

Instabilities of Multiorbital Electron Systems

Von der Fakultät für Mathematik, Informatik und
Naturwissenschaften der RWTH Aachen University zur
Erlangung des akademischen Grades eines Doktors der
Naturwissenschaften genehmigte Dissertation

vorgelegt von

Diplom-Physiker Stefan Andreas Uebelacker
aus Fulda

Berichter: Prof. Dr. Carsten Honerkamp
Prof. Dr. Werner Hanke

Tag der mündlichen Prüfung: 2. Dezember 2013

Diese Dissertation ist auf den Internetseiten der Hochschul-
bibliothek online verfügbar.

Summary

In the present thesis, we consider interaction induced instabilities in different electronic models consisting of multiple orbitals. We employ the functional renormalization group method, to tackle the many-particle problem. The main goal of this work is the identification of leading instabilities of different interacting electron systems and the relevant energy scales for the onset of correlations.

First, we recapitulate the functional renormalization group formalism and discuss details of its application. We proceed with the investigation of two models, a continuum model and a model on a checkerboard lattice, which exhibit a single quadratic band crossing point at the Fermi level. Here, we find that electron-electron interactions can lead to ordering with non-trivial topological properties, i.e. the existence of topologically protected edge states. We further discuss the emergence of superconductivity, when the band crossing point is shifted away from the Fermi surface.

Then, we turn to more realistic models featuring quadratic and cubic band crossing points, namely the honeycomb bi- and trilayer, which are used to describe the graphene layered systems. We obtain rich phase diagrams, with antiferromagnetic spin-density, two types of charge-density waves and a quantum spin Hall phase, which features in the case of the trilayer topologically protected edge states. With interaction parameters extracted from *ab initio* calculations, we observe a close competition between the antiferromagnetic and quantum spin Hall state. Here, the precise shape of the interaction decides which instability is the leading one. A comparison of the energy scales of the ordering phenomena in tri-, bi- and single layer reveals that when the interaction parameters from *ab initio* are appropriately rescaled, the functional renormalization group can qualitatively reproduce experimental gap sizes in the respective materials consistently.

Afterwards, we study a multiband model of the copper-based unconventional superconductors. This is motivated by a puzzling material trend in copper-based high- T_c superconductors, pointed out by Pavarini et al. [Pav01]: Compounds with larger next-nearest-neighbor hopping generally exhibit larger critical temperatures, which cannot be easily understood within spin-fluctuation theories of the one-band Hubbard model. Therefore, we consider the extension of the original model by including additional orbitals. We investigate a two-band model with an additional $4s$ orbital within a two-patch approximation and the N -patch-scheme. By this, a general understanding of the influence of the additional orbitals is established. Afterwards, we additionally include the

$3d_{z^2}$ orbital and show that the material trend, found in experiments, can, at least, qualitatively be reproduced.

Lastly, we go back to the single band Hubbard model and examine the consequences of the widely used approximation of neglecting the self-energy and the frequency dependence of the interaction vertex. We establish that the phase diagram obtained from the functional renormalization group is only quantitatively affected. From this study, we conclude that neglecting self-energy and frequency dependence, is a sensible approach, in order to obtain a reliable qualitative picture of the low energy behavior of a weakly or moderately coupled system at reasonable expense.

Zusammenfassung

In dieser Arbeit untersuchen wir wechselwirkungsinduzierte Instabilitäten verschiedener Modelle mit mehreren Orbitalen. Wir verwenden die funktionale Renormierungsgruppe um das Vielteilchenproblem zu behandeln. Das Hauptziel dieser Arbeit ist es, führende Instabilitäten verschiedener Systeme wechselwirkender Elektronen und die zugehörigen Energieskalen für das Einsetzen von Korrelationen zu identifizieren.

Zunächst wiederholen wir den Renormierungsgruppenformalismus und diskutieren Details seiner Anwendung. Wir fahren fort mit der Untersuchung von zwei Modellen – einem Kontinuum-Modell und einem Modell auf dem Schachbrett-Gitter – die einen quadratischen Bandkreuzungspunkt am Fermi-Niveau besitzen. Hier finden wir, dass Elektron-Elektron-Wechselwirkung zu Ordnungsphänomenen mit nichttrivialen topologischen Eigenschaften führen kann, wie etwa die Existenz von topologisch geschützten Randzuständen. Außerdem diskutieren wir die Ausbildung supraleitender Phasen bei Verschiebung des Bandkreuzungspunkts weg vom Fermi-Niveau.

Anschließend wenden wir uns realistischeren Modellen zu, die quadratische und kubische Bandkreuzungspunkte aufweisen, und zwar das zwei- und dreilagige Honigwabengitter, das als Modell für Graphensysteme benutzt wird. Wir erhalten reichhaltige Phasendiagramme, die eine antiferromagnetische Spindichte- und zwei Arten von Ladungsdichtewellen sowie eine Quanten-Spin-Hall-Phase beinhaltet, die im Falle des Gitters in drei Schichten topologisch geschützte Randzustände aufweist. Mit Wechselwirkungsparametern aus Ab-Initio-Rechnungen ergibt sich eine starke Rivalität zwischen der antiferromagnetischen und der Quanten-Spin-Hall-Phase. Hier entscheidet die genaue Form der Wechselwirkung, welche Instabilität die führende ist. Ein Vergleich der Energieskalen der Ordnungsphänomene in drei-, zwei-, und monolagigen Schichten zeigt, dass die funktionale Renormierungsgruppe in der Lage ist experimentelle Gap-Größen in den jeweiligen Materialien qualitativ konsistent zu reproduzieren, wenn die Ab-Initio-Wechselwirkungsparameter geeignet reskaliert werden.

Danach betrachten wir ein Multiband-Modell der kupferbasierten unkonventionellen Supraleiter. Die Motivation hierfür ist ein ungeklärter Materialtrend in kupferbasierten Hoch-Temperatur-Supraleitern, der von Pavarini et al. aufgezeigt wurde [Pav01]: Verbindungen mit größerem Nächst-Nachbar-Hüpfen weisen allgemein höhere kritische Temperaturen auf, was innerhalb von Spinfluktuationstheorien im Einband-Modell nicht zu erklären ist. Daher betrachten wir die Erweiterung des ursprünglichen Modells um zusätzliche Orbitale.

Wir untersuchen ein Zweiband-Modell mit zusätzlichem $4s$ -Orbital innerhalb der Zwei-Patch-Näherung und des N -Patch-Schemas. Dabei gewinnen wir ein generelles Verständnis des Einflusses zusätzlicher Orbitale. Danach fügen wir außerdem das $3d_{z^2}$ -Orbital hinzu und zeigen, dass der experimentelle Materialtrend zumindest qualitativ reproduziert werden kann.

Zuletzt gehen wir zurück zum Einband-Hubbard-Modell und untersuchen die Auswirkungen der oft verwendeten Näherungen, die Selbstenergie und die Frequenzabhängigkeit des Wechselwirkungsverstärkers zu vernachlässigen. Wir stellen fest, dass sich das aus der funktionalen Renormierungsgruppe erhaltene Phasendiagramm nur quantitativ ändert. Anhand unserer Untersuchung schließen wir, dass die Vernachlässigung der Selbstenergie und der Frequenzabhängigkeit eine sinnvolle Herangehensweise ist, um ein qualitatives Bild des niederenergetischen Verhaltens eines schwach bis mäßig gekoppelten Systems mit angemessenem Aufwand zu erhalten.

Contents

1	Introduction	9
1.1	Context	9
1.2	Outline of the Thesis	10
2	The Functional Renormalization Group Scheme	13
2.1	Introduction	13
2.2	Generating Functionals	15
2.3	The Flow Equation of the Effective Action	16
2.4	Flow Equations of the 1PI Vertex Functions	17
2.5	Cutoff-Function and Initial Condition	21
2.6	Application of the Scheme	22
2.7	Orbital Mixing	23
3	Instabilities of Quadratic Band Crossing Points	27
3.1	Introduction	27
3.2	Continuum Fermion Model	29
3.3	Functional Renormalization Group Treatment	31
3.4	Phase Diagram of the Continuum Model	33
3.5	Model on a Checkerboard Lattice	39
3.6	Flows at Non-Vanishing Chemical Potential	42
3.7	Conclusion	43
4	Instabilities of Interacting Electrons on the Honeycomb Bilayer	45
4.1	Introduction	45
4.2	Model	47
4.3	Functional Renormalization Group Treatment	51
4.4	Phase Diagram of the Honeycomb Bilayer	53
4.5	Critical Scale of the Instabilities	59
4.6	Inclusion of Long-Ranged Interaction	61
4.7	Conclusion	63
5	Interacting Electrons on Trilayer Honeycomb Lattices	65
5.1	Introduction	65
5.2	Models	66
5.3	ABA and ABC Trilayer Hubbard Model	71
5.4	ABC trilayer: Instabilities and Phase Diagram with Non-Local Interactions	75

5.5	Energy Scales of the Ordering Phenomena	79
5.6	Conclusion	82
6	Multiband Effects on Superconducting Instabilities Driven by Electron-Electron Interactions	85
6.1	Introduction	85
6.2	Models	88
6.3	Functional Renormalization Group Treatment	91
6.4	Results for the Two-Band Model	93
6.5	Simplified Picture: Two-Patch Model	95
6.6	Results for the Three-Band Model	98
6.7	Conclusion	104
7	Self-Energy Feedback and Frequency-Dependent Interactions	107
7.1	Introduction	107
7.2	Model and Method	109
7.3	Case without Instability	111
7.4	Critical Scales and Leading Instabilities	112
7.5	Flow of the Self-Energy	117
7.6	Discussion	122
8	Conclusion and Outlook	125
A	Improved Patching for the Checkerboard Lattice Model	129
B	Critical Scale from RPA	131
	Bibliography	133
	Publications	151
	Acknowledgements	153
	Curriculum Vitae	155

Chapter 1

Introduction

1.1 Context

Nature presents a variety of materials, in which electron-electron interactions play a crucial role for the observed properties. Prominent examples are the layered iron-pnictide and copper-oxide materials, which exhibit the astonishing feature of high T_c -superconductivity [PG10; SB07]. Here, interactions lead to an instability of the system towards a ground state, in which global gauge invariance is spontaneously broken. This mechanism of interaction-induced spontaneous symmetry breaking is responsible for many fascinating properties of interacting electron systems.

The inclusion of interactions is, however, a challenging task and subject of present research in the study of correlated materials. Some of the most interesting correlation effects have been found in systems, which can, in good approximation, be described by a two-dimensional model of interacting electrons on a lattice, which is formed by static ions. A prominent example is the infamous Hubbard model [Hub63] on a square lattice, which is expected to contain the crucial ingredients to describe high T_c -superconductivity in the copper-oxide compounds. Even after decades of intensive research, it is still far from understood (see e.g. [SB07]). The original Hubbard model has natural extensions to different lattice structures, multiple orbitals, non-local interactions and more remote hoppings.

Recently, there has been increasing interest in the study of models with multiple orbitals. In 2008 high- T_c superconductivity was discovered in layered iron-pnictides [Kam08]. In these materials, the Fermi surface is not restricted to a single band as in the cuprates. The orbital mixing, i.e., the fact, that the bands at the Fermi level are composed of multiple orbitals, leads to a pronounced momentum dependence of the interaction, which implies for instance that certain scattering amplitudes are already attractive at the bare level. That is, aside from the Fermi surface shape, one has to account for this additional feature of the band-structure that is crucial for a realistic picture of the low-energy physics, e.g., the symmetry of the pairing gap [Hon10].

Another example for an interesting system with multiple orbitals, is given by the honeycomb lattice with one or more coupled layers. Such a lattice is realized in graphene, which has been fabricated in thin sheets, consisting of very

few or even a single atomic layer [Nov04]. In graphene, multiple bands touch the Fermi surface. In models restricted to the largest hopping terms, this leads to band-structures featuring band crossing at isolated points at the Fermi level, e.g., a Dirac cone in the case of the single layer. Again, the orbital composition of the bands, which leads to a winding of the Bloch eigenvectors around the band crossing points, is crucial for interesting properties [Cas09]. For instance an interaction driven ground state with topologically non-trivial order might be realizable in these materials [Rag08].

This work connects to these recent developments and investigates different electron models consisting of multiple bands. Often, multiorbital systems are discussed in the context of strongly correlated transition metal oxides, where usually electrons are treated as rather localized objects [Hot06]. Therefore, we briefly note that in this thesis we deal with multiorbital systems from the view of Fermi surface instabilities of itinerant electron systems. In most cases, considering more than one band is the natural and self-evident approach, like in honeycomb bi- and trilayer, where more than one band touches the Fermi surface. However, we will also deal with a description of the copper-oxides, that is more refined, than the one-band Hubbard model, by taking into account bands at higher energy, which do not touch the Fermi surface, in order to understand experimentally observed material trends.

We will employ the functional renormalization group (fRG) method, to tackle the many-particle problem. The formalism is based on an exact flow equation for the generating functional of the one-particle irreducible (1PI) vertex function. This approach provides a systematic and quite generally applicable procedure for the identification of the leading instability of a given interacting electron system.

The main goal of this work is the estimation of tentative phase diagrams for several multiorbital systems. Additionally, we will be interested in the relevant energy scales of the ordering phenomena obtained from the fRG, as these can be used as an order of magnitude estimate for experimentally found ordering temperatures and gap sizes.

1.2 Outline of the Thesis

This thesis is organized as follows. In chapter 2 we explain the fRG method, as it has been used in this work. After a short introduction, we present the flow equations for the one-particle irreducible (1PI) vertex functions in the presence of charge-, and spin-conservation for interacting electrons on a lattice. Afterwards, we elaborate on details of the application, such as the chosen cutoff and employed approximations. Finally, the orbital mixing, which is specific to multiorbital models, and its implications for the application of the fRG method are discussed.

Chapter 3 describes the investigation of two models, a continuum model

and a model on a checkerboard lattice, which exhibit a single quadratic band crossing point (QBCP) at the Fermi level. Here, we find that electron-electron interaction can induce ordered states with non-trivial topological properties, i.e. these states feature the existence of edge state, which are protected by topology. We discuss the emergence of superconductivity for finite chemical potentials.

In Chapter 4, we discuss instabilities of interacting electrons on the honeycomb bilayer at and near half-filling. We obtain a rich phase diagram, with an antiferromagnetic (AFM) spin-density wave (SDW), two types of charge-density wave (CDW) and a quantum spin Hall (QSH) phase, depending on interaction parameters. We compare the critical scale, found within the fRG method, with quantum Monte Carlo (QMC) data and discuss the relation to experimental findings in bilayer graphene.

We extend this study to the honeycomb trilayer in chapter 5. Here, we compare two different stacking orders, which can be realized in trilayer graphene and obtain a similar phase diagram as in the bilayer case. A comparison of the energy scales of the ordering phenomena for the tri-, bi- and single layer reveals, that with appropriately chosen initial interaction strength, one can reproduce experimental results on the respective materials qualitatively.

Chapter 6 is motivated by a puzzling material trend in copper-based high- T_c superconductors. Compounds with larger next-nearest-neighbor hopping generally exhibit larger T_c [Pav01], which cannot be easily understood within spin-fluctuation theories of the one-band Hubbard model. Therefore, we consider the extension of the original model, by including additional orbitals. We investigate a two-band model with included $4s$ orbital within a two-patch approximation and the N -patch fRG scheme. By this, a general understanding of the influence of the additional orbitals is established. Afterwards, we additionally include the $3d_{z^2}$ orbital and show that the material trend, found in experiments, can be qualitatively reproduced.

Finally, chapter 7 is mostly devoted to technical improvements of the fRG. Here, we go back to the single band Hubbard model and examine consequences of the widely used approximation of neglecting the self-energy and the frequency dependence of the interaction vertex. We establish, that the overall phase diagram is only quantitatively altered. Moreover, we detect precursors of the breakdown of the Fermi-liquid behavior in the flow of the self-energy for diverging flows near the critical scale.

In the conclusion in chapter 8, we summarize the results and give a short outlook on possible routes of future research.

Parts of this thesis have been previously published in the articles listed on page 151.

Chapter 2

The Functional Renormalization Group Scheme

In this chapter, we introduce the fRG scheme. First, we give a short overview on the renormalization group mainly considering the application to two-dimensional fermionic systems. Afterwards, we present the fRG formalism and the flow equations for the 1PI vertex functions, which are used in this work. We discuss details on the application of these equations to actual systems and illustrate how the multiband character of the systems is treated.

Contents

2.1	Introduction	13
2.2	Generating Functionals	15
2.3	The Flow Equation of the Effective Action	16
2.4	Flow Equations of the 1PI Vertex Functions	17
2.5	Cutoff-Function and Initial Condition	21
2.6	Application of the Scheme	22
2.7	Orbital Mixing	23

2.1 Introduction

Initially, the idea of renormalization achieved remarkable success in quantum electrodynamics. Here, it provided a mechanism to eliminate divergences, which arise in perturbation theory due to unbounded contributions in the high energy sector (see e.g. [Zee10] for a pedagogical introduction). Wilson promoted renormalization group techniques to the application to statistical physics [Wil71]. He was able to calculate critical exponents for a continuous spin Hamiltonian by successively integrating out degrees of freedom in a certain momentum shell. The beautiful concepts of the renormalization group like scale dependent Hamiltonians, the analysis of the flow to fixed-points, and the identification of relevant and irrelevant terms in a given Hamiltonian, proved to be very useful for the analysis of critical behavior (see, e.g., the reviews of Fisher [Fis74] and Shankar [Sha94]).

The term functional renormalization group (fRG) is a label for approaches, which are based on exact flow equation for generating functionals of vertex functions, as derived, for instance, in [Pol84; Wet93; SH01]. An instructive comparison of the flow equations of different generating functionals, such as the 1PI, the Wick-ordered and the Polchinski scheme is given in [Ens05].

Nowadays, the application of the fRG method covers a wide range of physical systems. We name the study of ultra cold atoms, e.g. [DW06; DW07; Flo08; BDS11], and high energy physics, e.g. [BTW02; Gie06; Paw07]. In condensed matter physics, the application ranges from the study of spin Hamiltonians, e.g. [RTT11; Got12], non-equilibrium physics, e.g. [Sch09; PSS10], to interacting fermions on a lattice. The latter is discussed in more detail in the following. For a comprehensive review on this see [Met12].

In the first applications of the fRG to the two-dimensional Hubbard model, the exact flow equations have been approximated by the neglect of the three-particle vertex, self-energy corrections and frequency dependence of the interaction vertex, and the restriction of the flow to the symmetric phase. Also the momentum dependence of the vertex has been simplified, including in the simplest version only the two saddle points in the Brillouin zone [Sch87; FRS98]. Later the more refined N -patch scheme has been introduced [ZS00; HM00; Hon01]. Here, the vertex is calculated at a larger set of momenta on the Fermi surface, typically consisting of a number of 32 points. Aside from the momentum shell cutoff, different regularization schemes have been employed, e.g. the temperature flow [HS01], the interaction flow [Hon04] and more recently the Ω cutoff with a frequency dependent regulator [HS09]. These schemes have the advantage, that they avoid the artificial suppression of the ferromagnetic instability of the momentum shell cutoff, as explained in [HS01; Met12]. Despite the simplifications, the N -patch scheme already provides a reasonable qualitative phase diagram for the two-dimensional Hubbard model at weak coupling, including an antiferromagnetic, d-wave pairing and ferromagnetic regime (e.g. [HS01; Met12]).

The improvement over these approximations is still ongoing research. A lot of effort is put into the access of the symmetry broken phase [Ger05; GHM08; SGM08], which is crucial to obtain more quantitative results, like e.g. gap sizes. Here however, one has to sacrifice the flexibility of the N -patch approach, as the treatment of competing instabilities becomes much more complicated. Also, the flow of the self-energy [HS03; KK04; RM05; Kat09; Ueb09] as well as the frequency dependence of the interaction vertex [KT06; FHL06; HFL07] has been treated to some extent. These two subjects are discussed in more detail in section 7.1. A promising path for improvement of the fRG scheme is a more efficient parametrization of the vertex function [HS09], which minimizes numerical cost, and is helpful in the inclusion of frequency dependence [HGS12], self-energy corrections [GS12], as well as in the access of the symmetry-broken phase [EM10].

Lastly, we mention the extension of the fRG method to multiband systems. This has been used to study the emergence of superconductivity in the various iron pnictide materials [Wan09; PHH09; WZL09; WZL10; Hon10; Tho11b; Tho11a]. Also, in close relation to the work exposed in chapters 4 and 5, possible instabilities of single layer graphene have been explored [Rag08; Hon08].

Instructive overviews are given by the review article by Metzner et al. [Met12] and the book written by Kopietz, Bartosch and Schütz [KBS10]. A mathematically more rigorous introduction to the fRG can be found in [Sal99].

2.2 Generating Functionals

The fRG scheme is already well documented in literature [Sal99; SH01; Ens05; And06; Hus09; KBS10; Met12]. Therefore, we only shortly recapitulate the flow equations of the 1PI vertex functions. In this section, we recall some standard definitions and relations of generating functionals, where we employ mostly the notation of the review article by Metzner et al. [Met12].

We consider the action

$$\mathcal{S}[\psi, \bar{\psi}] = - \sum_{x, x'} \bar{\psi}(x') G_0^{-1}(x', x) \psi(x) + V_0[\psi, \bar{\psi}]. \quad (2.1)$$

$\psi(x)$ and $\bar{\psi}(x)$ are Grassmann numbers and represent the eigenvalues of the corresponding fermionic coherent states, which are assigned by the general quantum number x and $G_0(x, x')$ is the free Green's function. Below, we will sometimes suppress the explicit notation of the quantum numbers. We will focus on electronic systems, which can be described by momentum, Matsubara frequency, band index and spin projection: $x = \{k, \omega, b, \sigma\}$. The interaction part is assumed to be quartic in the fields

$$V_0[\psi, \bar{\psi}] = \sum_{\substack{x_1, x_2, \\ x'_1, x'_2}} V_0(x'_1, x'_2, x_1, x_2) \bar{\psi}(x'_1) \bar{\psi}(x'_2) \psi(x_2) \psi(x_1), \quad (2.2)$$

with the bare interaction vertex $V_0(x'_1, x'_2, x_1, x_2)$, which will be specified for the individual models below.

The generating functional of the connected Green's function is given by [NO98; Met12]

$$\mathcal{G}[\eta, \bar{\eta}] = - \ln \int [D\psi \bar{\psi}] \exp(-\mathcal{S}[\psi, \bar{\psi}] + (\bar{\eta}, \psi) + (\bar{\psi}, \eta)), \quad (2.3)$$

where we introduced the shorthand notations $\int [D\psi \bar{\psi}] = \int \prod_x d\psi(x) d\bar{\psi}(x)$ and $(A, B) = \sum_x A(x)B(x)$ as in [Met12]. All connected Green's functions can be derived from this functional by computing the derivative with respect to the

corresponding source fields η and $\bar{\eta}$ [NO98; Met12]

$$\begin{aligned} G^{(2m)}(x'_1, \dots, x'_m, x_1, \dots, x_m) &= -\langle \psi(x'_1) \cdots \psi(x'_m) \bar{\psi}(x_m) \cdots \bar{\psi}(x_1) \rangle_c \\ &= (-1)^m \frac{\partial^{2m} \mathcal{G}[\eta, \bar{\eta}]}{\partial \bar{\eta}(x'_1) \cdots \partial \bar{\eta}(x'_m) \partial \eta(x_m) \cdots \partial \eta(x_1)} \Big|_{\eta=\bar{\eta}=0}. \end{aligned} \quad (2.4)$$

$\langle \cdots \rangle_c$ denotes the connected expectation value, i.e. the sum of all connected diagrams contributing to the thermal average. The partition function is obtained from the generating functional as $Z = \exp(-\mathcal{G}[0, 0])$ [Met12].

We will however prefer to consider the Legendre transform of the functional $\mathcal{G}(\eta, \bar{\eta})$ [Met12]

$$\Gamma[\psi, \bar{\psi}] = \mathcal{G}[\eta, \bar{\eta}] + (\bar{\eta}, \psi) + (\bar{\psi}, \eta). \quad (2.5)$$

This functional is often called the effective action and is the generating functional of the 1PI vertex functions [NO98; Met12]

$$\Gamma^{(2m)}(x'_1, \dots, x'_m, x_1, \dots, x_m) = \frac{\partial^{2m} \Gamma[\psi, \bar{\psi}]}{\partial \bar{\psi}(x'_1) \cdots \partial \bar{\psi}(x'_m) \partial \psi(x_m) \cdots \partial \psi(x_1)} \Big|_{\psi=\bar{\psi}=0}. \quad (2.6)$$

The old and new fields are related via [Met12]

$$\frac{\partial \Gamma[\psi, \bar{\psi}]}{\partial \psi(x)} = -\bar{\eta}(x), \quad \frac{\partial \Gamma[\psi, \bar{\psi}]}{\partial \bar{\psi}(x)} = \eta(x). \quad (2.7)$$

The second derivatives of the generating functionals are the inverse of one another [NO98; Met12]

$$\begin{aligned} \sum_{x_2} \begin{pmatrix} \frac{-\partial^2 \mathcal{G}[\eta, \bar{\eta}]}{\partial \bar{\eta}(x_3) \partial \eta(x_2)} & \frac{\partial^2 \mathcal{G}[\eta, \bar{\eta}]}{\partial \bar{\eta}(x_3) \partial \bar{\eta}(x_2)} \\ \frac{\partial^2 \mathcal{G}[\eta, \bar{\eta}]}{\partial \eta(x_3) \partial \eta(x_2)} & \frac{-\partial^2 \mathcal{G}[\eta, \bar{\eta}]}{\partial \eta(x_3) \partial \bar{\eta}(x_2)} \end{pmatrix} \begin{pmatrix} \frac{\partial^2 \Gamma[\psi, \bar{\psi}]}{\partial \bar{\psi}(x_2) \partial \psi(x_1)} & \frac{\partial^2 \Gamma[\psi, \bar{\psi}]}{\partial \bar{\psi}(x_2) \partial \bar{\psi}(x_1)} \\ \frac{\partial^2 \Gamma[\psi, \bar{\psi}]}{\partial \psi(x_2) \partial \psi(x_1)} & \frac{\partial^2 \Gamma[\psi, \bar{\psi}]}{\partial \psi(x_2) \partial \bar{\psi}(x_1)} \end{pmatrix} &= \delta_{x_1, x_3} \begin{pmatrix} 1 & 0 \\ 0 & 1 \end{pmatrix} \\ = \mathbf{G}^{(2)}[\eta, \bar{\eta}] & \mathbf{\Gamma}^{(2)}[\psi, \bar{\psi}] = \mathbb{1}. \end{aligned} \quad (2.8)$$

For vanishing source fields and in presence of charge symmetry, we obtain the Dyson equation [Met12]

$$\Gamma^{(2)} = G^{-1} = G_0^{-1} - \Sigma. \quad (2.9)$$

Here, Σ is the self-energy and $G^{-1} = (G^{(2)})^{-1}$ is the full Green's function.

2.3 The Flow Equation of the Effective Action

The fRG approach is based on the idea to introduce a regularization parameter Λ in the free Green's function. A common way to do this, which we will employ here, is to multiply a regularization or cutoff function to the free Green's

function as

$$G_0^\Lambda = \theta(\Lambda)G_0. \quad (2.10)$$

Typically, at the beginning of the flow, the cutoff function is identical to zero, so that all vertex corrections vanish. During the fRG flow, more and more contributions of the vertex correction are successively included, until, at least in principle, we recover the complete action. In practice, truncations are employed, as the complete integration of the flow equation is not feasible, as we discuss below.

With the introduction of the cutoff function, $\Gamma[\psi, \bar{\psi}] \rightarrow \Gamma^\Lambda[\psi, \bar{\psi}]$ now depends on the parameter Λ and we can derive a differential equation, to compute the effective action in dependence of Λ from the initial value at $\Lambda = \Lambda_0$. This can be most easily done by calculating the corresponding differential equation for the generating functional of the connected Green's function $\mathcal{G}^\Lambda[\eta, \bar{\eta}]$ first, as for instance shown in [Ens05]. With this and the relation (2.8), one can derive the well-known flow equation of the effective action [Met12]

$$\frac{d}{d\Lambda}\Gamma[\psi, \bar{\psi}] = -\frac{1}{2}(\bar{\Psi}, \dot{\mathbf{Q}}_0^\Lambda \Psi) - \frac{1}{2}\text{Tr}\left(\dot{\mathbf{Q}}_0^\Lambda (\mathbf{\Gamma}^{(2)\Lambda}[\psi, \bar{\psi}])^{-1}\right). \quad (2.11)$$

Here, the dot denotes the derivative with respect to Λ and we combined the fields in a Nambu notation as $\bar{\Psi} = (\bar{\psi}, \psi)$ and $\Psi = (\psi, \bar{\psi})^T$. Moreover, $\text{Tr}(AB) = \sum_{x,c,x',c'} A(x, c; x', c')B(x', c'; x, c)$, where the additional charge index c is represented in the matrix structure in equations (2.8, 2.12). For a U(1)-charge symmetric action of the form of equation (2.1, 2.2),

$$\mathbf{Q}_0^\Lambda = \begin{pmatrix} Q_0^\Lambda & 0 \\ 0 & -(Q_0^\Lambda)^T \end{pmatrix} \quad (2.12)$$

is diagonal, where $Q_0^\Lambda = (G_0^\Lambda)^{-1}$ and $(Q_0^\Lambda(x', x))^T = Q_0^\Lambda(x, x')$, see [Met12].

Up to now, we have not made use of any approximation and the flow equation (2.11) is thus an exact identity. It contains all contributions to the effective action with arbitrary power in the fields.

2.4 Flow Equations of the 1PI Vertex Functions

For the actual application to specific systems, the exact flow equation (2.11) has to be expanded in powers of the Grassmann fields. This leads to an infinite hierarchy of flow equations, where the flow equation of each vertex contains contributions of the vertex of the next higher order. The general flow equations for the lowest vertex functions are for instance derived in [SH01; Met12].

Here, we first want to restrict the free action to a more specialized form, which respects SU(2)-spin-rotational-symmetry and momentum conservation.

The free propagator is then given by

$$G_0(x', x) = G_0(p) \delta_{kk'} \delta_{\omega\omega'} \delta_{bb'} \delta_{\sigma\sigma'} , \quad (2.13)$$

where $p = \{k, \omega, b\}$ combines momentum, frequency and band index, and

$$G_0(p) = \frac{1}{i\omega - \xi_b(k)} \quad (2.14)$$

with $\xi_b(k) = \epsilon_b(k) - \mu$. Here, $\epsilon_b(k)$ is the dispersion relation and μ the chemical potential. The fermionic Matsubara frequencies are given by $\omega = (2n + 1)\pi T$ with $n \in \mathbb{Z}$. Similarly, we write for the inverse Green's function $Q_0^\Lambda(p) = (G_0^\Lambda(p))^{-1}$ with $G_0^\Lambda(p) = \theta(\Lambda)G_0(p)$.

The coefficient of the quartic part of the action in equation (2.2) reads

$$V_0(x_3, x_4, x_1, x_2) = V_0(p_1, p_2, p_3, b_4) \frac{T}{2\mathcal{N}} \delta_{k_1+k_2, k_3+k_4} \delta_{\omega_1+\omega_2, \omega_3+\omega_4} \delta_{\sigma_1\sigma_3} \delta_{\sigma_2\sigma_4} . \quad (2.15)$$

Here, T is the temperature and \mathcal{N} is the number of unit cells. In the reduced interaction $V_0(p_1, p_2, p_3, b_4)$ we introduced another convention with respect to the order of the indices for a better conformance with the literature. Below, we will usually state the considered Hamiltonians in the language of second quantization. For the connection between the two formalisms, we refer to familiar textbooks [AS06; NO98].

A system with an action restricted to the form defined by equations (2.13 – 2.15) respects U(1)-charge and SU(2)-spin-rotational symmetry as well as momentum conservation. Usually, we will ask questions like, what is the leading instability of a system or at which scale do correlation effects become strong? For this matter, the fRG equations can be simplified by explicitly incorporating spin-rotational invariance and momentum conservation in the vertex functions, so that a reduced set of couplings suffices to describe the effective action at a given scale. Therefore, we write, in analogy with equations (2.13, 2.15)

$$\Sigma^\Lambda(x', x) = \Sigma^\Lambda(p) \delta_{kk'} \delta_{\omega\omega'} \delta_{bb'} \delta_{\sigma\sigma'} , \quad (2.16)$$

$$G^\Lambda(x', x) = G^\Lambda(p) \delta_{kk'} \delta_{\omega\omega'} \delta_{bb'} \delta_{\sigma\sigma'} , \quad (2.17)$$

$$\begin{aligned} \Gamma^{(4)\Lambda}(x_3, x_4, x_1, x_2) &= \frac{T}{\mathcal{N}} \delta_{k_1+k_2, k_3+k_4} \delta_{\omega_1+\omega_2, \omega_3+\omega_4} \\ &\times (V^\Lambda(p_1, p_2, p_3, b_4) \delta_{\sigma_1\sigma_3} \delta_{\sigma_2\sigma_4} - V^\Lambda(p_2, p_1, p_3, b_4) \delta_{\sigma_1\sigma_4} \delta_{\sigma_2\sigma_3}) . \end{aligned} \quad (2.18)$$

$V^\Lambda(p_1, p_2, p_3, b_4)$ is the coupling function of the two-particle 1PI vertex, with the first two indices denoting ingoing and the third and fourth index denoting outgoing particles. The spin convention is such that the spin of the first and the third leg is the same, see also figure 2.1. The fourth momentum and frequency in the interaction vertex is fixed by conservation, so that here only the band index is written.

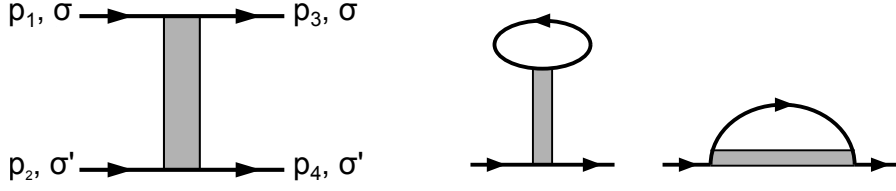


Figure 2.1: Left: Diagrammatic representation of the two-particle 1PI vertex. The spin is conserved along the short edges of the interaction vertex. Middle and right: Diagrammatic representation of the terms in the flow equations for the self-energy. Figure modified from [SH01].

With this, the flow equations for the self-energy and the two-particle 1PI vertex can be written as (see [SH01; PHH09; Met12])

$$\frac{d}{d\Lambda} \Sigma^\Lambda(p) = \int dp' S^\Lambda(p') [V^\Lambda(p, p', p', b) - 2V^\Lambda(p, p', p, b')] , \quad (2.19)$$

$$\begin{aligned} \frac{d}{d\Lambda} V^\Lambda(p_1, p_2, p_3, b_4) \\ = \tau_{\text{PP}}^\Lambda(p_1, p_2, p_3, b_4) + \tau_{\text{PH,d}}^\Lambda(p_1, p_2, p_3, b_4) + \tau_{\text{PH,cr}}^\Lambda(p_1, p_2, p_3, b_4) , \end{aligned} \quad (2.20)$$

with the particle-particle channel

$$\tau_{\text{PP}}^\Lambda(p_1, p_2, p_3, b_4) = - \int dp \sum_{b'} L^\Lambda(p, q_{\text{PP}}) V^\Lambda(p_1, p_2, p, b') V^\Lambda(p, q_{\text{PP}}, p_3, b_4) , \quad (2.21)$$

the direct particle-hole channel

$$\begin{aligned} \tau_{\text{PH,d}}^\Lambda(p_1, p_2, p_3, b_4) = - \int dp \sum_{b'} L^\Lambda(p, q_{\text{PH,d}}) \\ \times \left[-2V^\Lambda(p_1, p, p_3, b') V^\Lambda(q_{\text{PH,d}}, p_2, p, b_4) + V^\Lambda(p, p_1, p_3, b') V^\Lambda(q_{\text{PH,d}}, p_2, p, b_4) \right. \\ \left. + V^\Lambda(p_1, p, p_3, b') V^\Lambda(p_2, q_{\text{PH,d}}, p, b_4) \right] , \end{aligned} \quad (2.22)$$

and the crossed particle-hole channel

$$\begin{aligned} \tau_{\text{PH,cr}}^\Lambda(p_1, p_2, p_3, b_4) = - \int dp \sum_{b'} L^\Lambda(p, q_{\text{PH,cr}}) \\ \times V^\Lambda(p, p_2, p_3, b') V^\Lambda(p_1, q_{\text{PH,cr}}, p, b_4) , \end{aligned} \quad (2.23)$$

where again $p = (k, w, b)$, and $q_{\text{PP}} = (-k + k_1 + k_2, -w + w_1 + w_2, b')$, $q_{\text{PH,d}} = (k + k_1 - k_3, w + w_1 - w_3, b')$, $q_{\text{PH,cr}} = (k + k_2 - k_3, w + w_2 - w_3, b')$ are the quantum numbers of the second line in the diagrams for the two-particle 1PI vertex. We changed to an integral representation of the summation in momentum space and introduced the shorthand notation $\int dp = T \sum_{\omega, b} \int \frac{dk}{V_{\text{BZ}}}$, where the integral

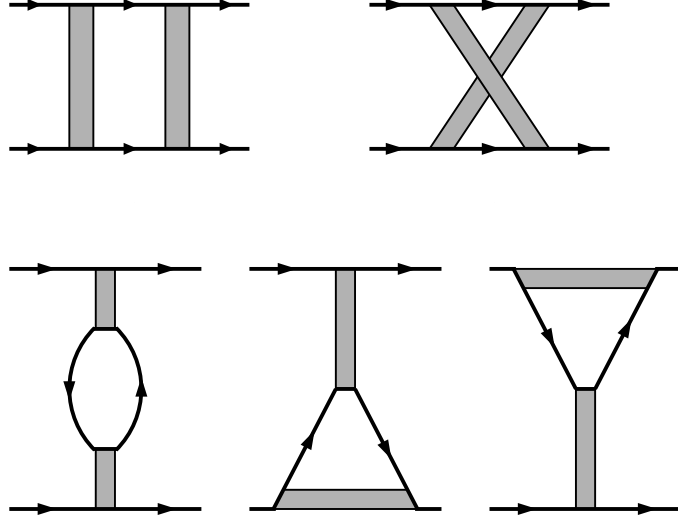


Figure 2.2: Diagrammatic representation of the terms in the flow equations for the two-particle 1PI vertex, with the particle-particle diagram τ_{PP}^Λ (top left), the crossed particle-hole diagram $\tau_{\text{PH,cr}}$ (top right), and the direct particle-hole diagrams $\tau_{\text{PH,d}}$ (bottom). The spin is conserved along the short edges of the interaction vertex. Figure taken from [SH01].

goes over the first Brillouin zone, which has the volume V_{BZ} . The internal loop is given by

$$L^\Lambda(p, p') = S^\Lambda(p)G^\Lambda(p') + G^\Lambda(p)S^\Lambda(p'), \quad (2.24)$$

with the single scale propagator

$$\begin{aligned} S^\Lambda(p) &= -G^\Lambda(p)\dot{Q}_0^\Lambda(p)G^\Lambda(p) \\ &= \frac{[i\omega - \xi_b(k)]\partial_\Lambda\theta(\Lambda)}{[i\omega - \xi_b(k) - \theta(\Lambda)\Sigma^\Lambda(p)]^2}. \end{aligned} \quad (2.25)$$

The flow equations (2.19 – 2.25) are for instance given in [SH01; PHH09; Met12] in different notations. An explicit derivation of the flow equations with incorporated symmetries can be found in [SH01]. Figures 2.1 and 2.2 show a diagrammatic representation of the flow equations.

We have closed the infinite hierarchy of flow equations, by setting the three-particle vertex to zero as is common practice. The three-particle vertex vanishes at $\Lambda = \Lambda_0$, but is generated during the flow. The approximation of neglecting this term restricts the validity of the approach to weak or moderate coupling strength. For small values of the interaction vertex, we expect reliable results as the contribution to the flow of the effective interaction is only third order in the interaction vertex [Met12]. However, when integrating out lower and lower scales, the couplings typically diverge. In this case, we stop the fRG flow, as

the contributions from the three-particle vertex are not negligible anymore.

Katanin showed that the replacement of the single scale propagator (2.25) in equations (2.21 – 2.23) by the expression $\frac{d}{d\Lambda}G^\Lambda(p)$ leads to a more accurate fulfillment of ward identities during the fRG flow [Kat04]. For flows into the symmetry broken regime, the replacement is indeed beneficial [Sal04]. In this work, we will mostly neglect self energy, in which case both expressions are identical. In chapter 7 we include self-energy feedback, however, we will not employ the Katanin modification to reduce the numerical effort, as we do not expect important effects for our flows in the symmetric phase.

2.5 Cutoff-Function and Initial Condition

The validity of the flow equations (2.19 – 2.25) is not restricted to a certain choice of the regularization function in (2.10). In fact, the renormalization group can be understood as a quite general semigroup law and is thus merely a rewriting of the original action [SH01].

For the application, we will choose the momentum shell cutoff, which can be written as

$$\theta(\Lambda) = \Theta(|\xi_b(k)| - \Lambda) . \quad (2.26)$$

Here, Θ denotes the step function, and thus all modes below Λ are cut off. At the initial value $\Lambda_0 = \max_{k,b}(|\xi_b(k)|)$, all vertex corrections vanish and the vertices at the beginning of the flow are simply given by the bare ones

$$\Sigma^{\Lambda_0}(p) = 0 , \quad (2.27)$$

$$V^{\Lambda_0}(p_1, p_2, p_3, b_4) = V_0(p_1, p_2, p_3, b_4) . \quad (2.28)$$

Clearly, with the action having only quadratic and quartic contributions, all higher vertices are zero at the initial scale. During the flow, the cutoff scale Λ is successively lowered and more and more corrections to the bare action are included. We briefly note, that the cutoff function is slightly softened in the numerical implementation for better feasibility.

Prominent alternatives to the momentum shell or energy cutoff are given by the temperature [HS01] and interaction flow scheme [Hon04]. More recently, the so called Ω -cutoff scheme, has been introduced by Husemann et al. [HS09; HGS12; GS12], where the bare propagator is multiplied with a frequency-dependent, rather than a momentum-dependent term.

It is well known that in the momentum shell cutoff instabilities in the particle-hole channel, with zero momentum transfer within the same band, are artificially suppressed. For instance, the ferromagnetic instability in the one-band Hubbard model cannot be detected with the momentum shell cutoff [HS01; Hus09; Met12]. We will stick to the energy cutoff scheme in our study of multi-band models, as we will not deal with instabilities, which are harmed by this artificial suppression and the energy cutoff is a natural and straightforward

choice.

2.6 Application of the Scheme

In section 2.4 we discussed the approximation of neglecting the three-particle vertex in the hierarchy of the fRG flow equations. For numerical feasibility we employ some further approximations, which have widely and successfully been used in literature ([Met12] and many works cited therein).

First, we neglect the flow of the self-energy by setting the right-hand side of equation (2.19) to zero. As the feedback of the self-energy in the flow of effective interaction is only third order in the interaction [Met12], we expect the self-energy to only become important when the effective interaction becomes large, and we stop the flow when this occurs.

Moreover, we neglect the frequency dependence of the vertex. That is, we only compute the zero frequency part of the interaction vertex and in the calculation of the one-loop diagrams the vertices are fixed to their scale-dependent values at zero frequency. With this, the frequency summation in the flow equations can be easily calculated analytically. The reasoning behind this approximation is, that the most relevant contributions to the flow to strong coupling comes from zero Matsubara frequency [Met12] and we are mainly interested in low-frequency vertices that are relevant for static ordering.

In chapter 7, we will go a step further by including the imaginary part of the self-energy and frequency dependence at least to a certain degree, while restricting to the Hubbard model in one band. We will see that, although some properties of the fRG flow are altered, e.g. the critical scale, at which the couplings diverge, becomes smaller, the overall shape of the phase diagram remains roughly the same. This is in accordance with results from several previous studies [Zan01; HS03; KT06; HFL07; Kat09].

The integration over momentum space is done numerically. For this, we divide the Brillouin zone into N patches and compute the vertex only on a finite set of representative momenta. Thereby, the interaction vertex is assumed to be constant within each patch and is determined by the value at the respective representative momentum. This procedure is in complete analogy with previous N -patch fRG studies (e.g. [Hon01; HS01; Hon08]). Usually we choose the set of representative momenta, which we will, hereafter, also refer to as patching points, to be located at the Fermi level, as the couplings at the Fermi level are expected to give the leading contribution to the flow [Hon01]. In chapter 3, 4 and 5, the Fermi level is given by a single point in momentum space, so that here we set the patching points on a ring around the Fermi point, to account for the angular dependence of the interaction vertex. This is detailed in section 3.3.

To reduce the numerical effort further, one can exploit additional symmetries of the system at hand. Typically the systems exhibit some rotational symmetry,

so that the coupling function only needs to be calculated for the patches in a part of the Brillouin zone. The remaining vertices can then be inferred from symmetry.

Usually, the interaction vertex undergoes a flow to strong coupling, i.e. a set of coupling constants diverge at a non-zero critical scale Λ_c . We will then stop the flow, as the truncation is no longer justified. The divergence is strictly speaking a (physically meaningful) artefact caused by the neglect of the self-energy in the flow. With self-energy correction, a gap would open up or some other modification of the low-energy spectrum would take place, and the flow would be regularized (see e.g. [Sal04]). Our analysis here tells us in which channel ordering occurs most prominently. The pronounced momentum structure of the vertex near the critical scale can be used to extract an effective Hamiltonian for the low-energy degrees of freedom. This is used to determine the leading order parameter of a given instability. The scale Λ_c can be interpreted as an (upper) estimate for ordering temperatures, if ordering is allowed by the Mermin-Wagner theorem [MW66], or at least as the temperature below which the dominant correlations should be clearly observable. Furthermore, one can understand Λ_c as energy scale for the modification of the spectrum, typically by a gap (see also [Hon01; PHH09]).

Below, we will apply the fRG approach with the discussed approximations to several models, to gain insight in the low energy behavior of the respective physical systems. Here, two advantages of the fRG method come into play. First, it can straightforwardly be applied to various different systems, i.e. it has no principal restriction to particular band-structures or interaction terms. Second, one does not need to specify the type of order, which one wants to investigate, rather the leading tendency emerges naturally from the flow.

2.7 Orbital Mixing

In all cases considered in this work, the bare action can be written in the form of equations (2.1, 2.2, 2.13 – 2.15). However, the single particle states are usually given in terms of an orbital basis (e.g. Wannier states), in which the interaction is either a pure on-site repulsion, or has some simple variation in momentum space, arising due to short-range interactions. For the implementation of the fRG equations, we will change to a band basis, in which the free Green's function is diagonal as in equation (2.13) via

$$\begin{aligned} \psi_{\omega,b,\sigma}(k) &= \sum_o u_{b,o}^*(k) \chi_{\omega,o,\sigma}(k) , & \bar{\psi}_{\omega,b,\sigma}(k) &= \sum_o u_{b,o}(k) \bar{\chi}_{\omega,o,\sigma}(k) , \\ \chi_{\omega,o,\sigma}(k) &= \sum_b u_{b,o}(k) \psi_{\omega,b,\sigma}(k) , & \bar{\chi}_{\omega,o,\sigma}(k) &= \sum_o u_{b,o}^*(k) \bar{\psi}_{\omega,b,\sigma}(k) , \end{aligned} \quad (2.29)$$

with a proper unitary transformation $u_{b,o}$. Here $\chi_{\omega,o,\sigma}(k)$ is the Grassmann field in the orbital basis, indicated by the index o and $\psi_{\omega,b,\sigma}(k)$ the field in

band basis, indicated by the index b . $u_{b,o}$ is also referred to as orbital content, weight or admixture. In fact, this basis has been used in equation (2.13) to arrive at the flow equations (2.19 – 2.23). For a calculation in this basis, we have to transform the interacting part of the action accordingly

$$\begin{aligned}
 & V_0[\psi, \bar{\psi}] \\
 &= \frac{T}{2\mathcal{N}} \sum_{\substack{\tilde{p}_1, \tilde{p}_2, \tilde{p}_3, \\ o_4, \sigma, \sigma'}} \tilde{V}_0(\tilde{p}_1, \tilde{p}_2, \tilde{p}_3, o_4) \bar{\chi}_{\omega_3, o_3, \sigma}(k_3) \bar{\chi}_{\omega_4, o_4, \sigma'}(k_4) \chi_{\omega_2, o_2, \sigma'}(k_2) \chi_{\omega_1, o_1, \sigma}(k_1) \\
 &= \frac{T}{2\mathcal{N}} \sum_{\substack{\tilde{p}_1, \tilde{p}_2, \tilde{p}_3, \\ o_4, \sigma, \sigma'}} \tilde{V}_0(\tilde{p}_1, \tilde{p}_2, \tilde{p}_3, o_4) \sum_{\substack{b_1, b_2, \\ b_3, b_4}} u_{b_1, o_1}(k_1) u_{b_2, o_2}(k_2) u_{b_3, o_3}^*(k_3) u_{b_4, o_4}^*(k_4) \\
 &\quad \times \bar{\psi}_{\omega_3, b_3, \sigma}(k_3) \bar{\psi}_{\omega_4, b_4, \sigma'}(k_4) \psi_{\omega_2, b_2, \sigma'}(k_2) \psi_{\omega_1, b_1, \sigma}(k_1) \\
 &= \frac{T}{2\mathcal{N}} \sum_{\substack{p_1, p_2, p_3, \\ b_4, \sigma, \sigma'}} V_0(p_1, p_2, p_3, b_4) \bar{\psi}_{\omega_3, b_3, \sigma}(k_3) \bar{\psi}_{\omega_4, b_4, \sigma'}(k_4) \psi_{\omega_2, b_2, \sigma'}(k_2) \psi_{\omega_1, b_1, \sigma}(k_1) .
 \end{aligned} \tag{2.30}$$

Here, we again used the multi-indices $p = \{k, \omega, b\}$ and $\tilde{p} = \{k, \omega, o\}$ including the band and orbital index respectively.

The factor $u_{b_1, o_1}(k_1) u_{b_2, o_2}(k_2) u_{b_3, o_3}^*(k_3) u_{b_4, o_4}^*(k_4)$ is often referred to as orbital mixing or ‘orbital makeup’ [Hon10]. In the last equation, we combined the orbital mixing and the interaction in orbital basis to the new interaction in band basis

$$V_0(p_1, p_2, p_3, b_4) = \sum_{\substack{o_1, o_2, \\ o_3, o_4}} \tilde{V}_0(\tilde{p}_1, \tilde{p}_2, \tilde{p}_3, o_4) u_{b_1, o_1}(k_1) u_{b_2, o_2}(k_2) u_{b_3, o_3}^*(k_3) u_{b_4, o_4}^*(k_4) . \tag{2.31}$$

Due to the extra factor, even the bare interaction can already exhibit a complicated structure in momentum space, which can decisively alter the outcome of the fRG flow (see Ref. [Hon10], which contains a discussion of the effect of this prefactor with respect to the iron-pnictides). For example, the orbital mixing can cause an instability in a system with a QBCP towards topologically non-trivial phases, which is not observed without this extra structure, as we will see below. We will study the influence of this feature on the pairing instability in a Hubbard-type model on a square lattice in chapter 6.

It is important to note that the transformation from orbital to band is not unique, i.e. the eigenvectors which diagonalize the quadratic part of the action are only fixed up to a complex momentum-dependent prefactor. This means that depending on the choice of this prefactor at any given point in momentum space, one can end up with different sign structure of the interaction vertex. However, the physics does, of course, not depend on this choice. If one would run the fRG flow exactly and then transform back to the orbital basis, the result would be independent of the choice we made for the transformation. However,

in practice two separate difficulties arise:

1. We carry out the summation over momentum numerically. This approach gives meaningful results as long as the momentum dependence is sufficiently smooth. On the other hand, the orbital mixing can lead to a pronounced momentum dependence already at the bare level as mentioned above. Thus, the approximation of the patching scheme is less accurate for choices of the orbital-to-band transformation, which exhibits discontinuities in the momentum dependence. We will, therefore, choose the transformation such that discontinuities in the interaction vertex are avoided, wherever possible. We will come back to this issue, when we discuss the choice of the transformation for the specific models.
2. In some cases in order to limit the numerical requirements it is necessary to restrict the fRG flow to a selected fraction of the degrees of freedom, i.e. only the conduction band. This will be the case in chapter 6. The flow of all other couplings is not computed. Thus, the complete information needed for the transformation in orbital basis at the end of the flow is not available, which poses problems in the interpretation of the numerical results.

In studies of the iron pnictides, the fRG method has been used, to tackle the question, which superconducting symmetry channel is dominant in the respective materials, i.e. whether the superconducting gaps exhibit nodes or not (e.g. [PHH09; Tho11a]). Here, the transformation back to the orbital basis after the flow is not straightforward due to the reasons outlined above. A practicable approach is to employ an ad hoc assumption for the couplings, which are not taken into account, e.g., to assume that these couplings have not changed during the flow [Lic12].

To avoid or at least reduce this issue here, we will exploit the freedom in the transformation, to minimize sign changes in the retained part of interaction processes, which is considered in the fRG flow. In this sense, the transformation is chosen to be minimal for the retained single particle states. In the models considered in chapter 6, we will only consider the conduction band in the fRG flow. Here, it is possible to identify a particularly suited choice of the transformation, which avoids sign changes of the transformation in momentum space from the orbital, which primarily contributes to the conduction band. With this choice, the multiband model transitions smoothly to the usual one-band model when the orbital mixing is reduced to zero.

Chapter 3

Instabilities of Quadratic Band Crossing Points

In this chapter, we study interaction-driven instabilities in QBCP two-orbital models in two dimensions, extending a previous study of Sun et al. [Sun09]. We explore the possibilities for interaction-driven topological states. In fact, the wavevector dependence of the Bloch eigenvectors of the free Hamiltonian causes interesting instabilities toward spin nematic (SN), quantum anomalous Hall (QAH) and QSH states. Topological non-trivial states occur at arbitrarily small interaction strength and for rather simple intraorbital and interorbital repulsions. We also discuss the emergence of superconductivity for finite chemical potentials.

Large parts of this chapter have previously been published in [UH11].

Contents

3.1	Introduction	27
3.2	Continuum Fermion Model	29
3.3	Functional Renormalization Group Treatment	31
3.4	Phase Diagram of the Continuum Model	33
3.5	Model on a Checkerboard Lattice	39
3.6	Flows at Non-Vanishing Chemical Potential	42
3.7	Conclusion	43

3.1 Introduction

Topological insulators are a new state of electron matter that have attracted enormous interest recently. For a detailed discussion, we refer to the reviews [HK10; QZ11]. These states can be distinguished from conventional insulators by topological invariants and robust subgap surface states. In the case of the integer quantum Hall effect [KDP80], the topological non-trivial state with a precisely quantized Hall conductivity is established in the presence of a strong magnetic field.

Later, Haldane realized, that a topological non-trivial state can also be constructed without external magnetic field [Hal88]. He introduced an imaginary

next-nearest-neighbor hopping term on a honeycomb lattice model, which, similar to a magnetic field, breaks time reversal symmetry. The total magnetic flux however is zero, as different contributions in the unit cell cancel each other. The topological non-trivial state he found is called QAH, where 'A' for anomalous refers to the property that no external magnetic field is needed [QZ11].

In two dimensions and in presence of time reversal invariance, a \mathbb{Z}_2 topological invariant can be associated with topological order [KM05b]. In this case, the topological non-trivial state is called QSH state. If the component of the electron spin along a certain quantization axis is conserved, the QSH state can be simply viewed as two copies of the QAH state associated with the two spin projections. Each copy contributes to the quantized Hall conductance with opposite sign, resulting in a net spin Hall conductance (see [KM05b; HK10; QZ11]).

In both QSH and QAH, the occurrence of protected edge states comes as a direct consequence of the topologically non-trivial nature of the bulk electronic band-structure, which is known as the bulk-boundary correspondence [HK10]. A very instructive way to visualize the topologically protected edge modes is, to define a model in single particle picture with non-vanishing topological quantum number on a strip geometry with periodic boundary conditions in one direction, as it is done e.g. in [QWZ06]. The energy spectrum can then be plotted in dependence of the wavevector along the strip. For the simplest case of the QAH state of spinless fermions, one obtains that within the energy gap of the bulk, two edge modes emerge, which are located at the opposite edges and cross the Fermi level with opposite Fermi velocity [QWZ06].

Usually, a topological non-trivial band-structure state is caused by the presence of spin orbit coupling. Initially, Kane and Mele proposed a spin-orbit term on the graphene lattice [KM05a], i.e. an imaginary next-nearest-neighbor hopping, that establishes the QSH state. However, it turned out that for graphene, the effect is too weak [Yao07; Gmi09]. Based on an insightful theoretical proposal [BHZ06], the QSH state could instead be realized in HgTe/CdTe quantum wells, where hallmarks of the QSH effect could be experimentally observed the first time [Kon07].

All this beautiful physics can be understood in the single particle picture. One could ask, however, if similar topologically non-trivial states can arise from interactions, through a phase transition at some critical temperature. Following this idea, different simple models were analyzed. Raghu et al. [Rag08] considered the honeycomb lattice with strong next-nearest-neighbor repulsion using mean-field and fRG techniques. Above a non-zero critical interaction strength [Rag08], the QSH state was found as the ground state of the system. This instability implies a spontaneous breaking of the spin rotational invariance. While this study serves as a proof of principle, it is by no means clear how one can realize the rather peculiar interaction with strong second-nearest-neighbor repulsion. Another study was performed by Zhang et al. [ZRV09]

for a three-dimensional lattice model where third-nearest neighbor interactions were essential to stabilize the QSH state.

A promising proposal came from Sun et al. [Sun09] who argued, based on mean-field calculations, that QBCP models should host QSH states already at arbitrarily weak interactions. The difference to the honeycomb lattice with its Dirac points is that, for a QBCP, the density of states is non-zero at the crossing point, and, hence, already a small interaction suffices to drive an instability. This picture is also supported by a mean-field study of Wen et al. [Wen10] who found topologically non-trivial phases already for small interactions in Kagome and decorated honeycomb lattice models with QBCPs.

Below, we consider two QBCP models [Sun09] in two dimensions. This allows us to explore the possibilities for interaction-driven topological states beyond mean-field theory. We furthermore investigate if there can be superconducting states emerging from topologically non-trivial insulators.

We briefly note that these interaction-driven topological insulators are also referred to as topological Mott insulators. The same term is sometimes used in the study of a slightly different question, which is the interplay between a Kane-Mele spin-orbit term leading to a topological band insulator, and the Hubbard on-site interaction leading to a Mott insulator, if sufficiently strong [RLH10; HLA11]. The present work addresses the interaction-induced generation of a Kane-Mele-type term in absence of significant spin-orbit coupling in the bare Hamiltonian, by interactions that are weaker than those required to drive the system Mott-insulating. The work [Var11] addresses the transition between topologically non-trivial and trivial states when non-zero interaction parameters are changed in finite-size systems. Interestingly, the single particle gap can remain robust across the topological transition, and both sides of the transition are insulators.

3.2 Continuum Fermion Model

We first consider a spin-1/2 model in the continuum in two dimensions, which describes the neighborhood of a QBCP. Following [Sun09], let the Hamiltonian be given by

$$H = H_{\text{free}} + H_{\text{int}} , \quad (3.1)$$

where the free part reads as

$$\begin{aligned} H_{\text{free}} &= \sum_{o,\sigma} \int dk \psi_{o,\sigma}^\dagger(k) H_{oo',\sigma}^0(k) \psi_{o',\sigma}(k) \\ &= \int dk \Psi^\dagger(k) \mathbf{H}^0(k) \Psi(k) . \end{aligned} \quad (3.2)$$

Here, the index σ denotes spin and $o = 1, 2$ denotes two different Fermi fields, which should be identified with the orbital degree of freedom and k is the

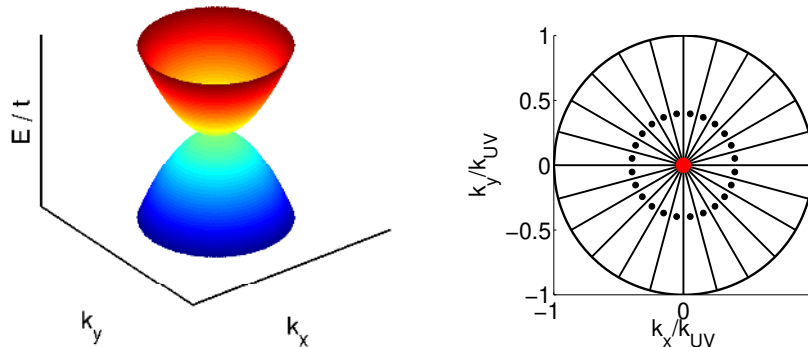


Figure 3.1: Left: Dispersion relation of the continuum model with the QBCP. Right: Sketch of the patching-scheme: the central red dot is the QBCP, and the black dots denote the momentum vectors k associated with respective patch, for which, the coupling function is computed.

momentum quantum number. In the second line, we have written the Hamiltonian in matrix notation, so that $\Psi = (\psi_{A,\uparrow}, \psi_{B,\uparrow}, \psi_{A,\downarrow}, \psi_{B,\downarrow})^T$ and $\Psi^\dagger = (\psi_{A,\uparrow}^\dagger, \psi_{B,\uparrow}^\dagger, \psi_{A,\downarrow}^\dagger, \psi_{B,\downarrow}^\dagger)$ combine spin and orbital degrees of freedom. We choose the free part to be of the form

$$\mathbf{H}^0(k) = I_S \otimes [d_I(k)I + d_x(k)\sigma_x + d_z(k)\sigma_z] , \quad (3.3)$$

where I_S is the unity matrix in spin space, I the unity matrix, and σ_x and σ_z the Pauli-matrices in orbital space. The integral is over a disk in two-dimensional momentum space. The disk radius, i.e. the ultraviolet (UV) cutoff, just determines the energy window focused on and will not be of any qualitative importance. The coefficients are $d_I(k) = t_I(k_x^2 + k_y^2) - \mu$, $d_x(k) = 2t_x k_x k_y$ and $d_z(k) = t_z(k_x^2 - k_y^2)$ as in [Sun09]. We will set t_I to zero and $t_x = t_z = t$ for simplicity. There is no t_y as this would break time-reversal symmetry or already create a QSH state at the bare level. Except for section 3.6, the chemical potential is set to zero so that the QBCP lies at the Fermi level. Note, that we exclude the possibility of spin orbit coupling by restricting the Hamiltonian to unity in spin space.

The free part can be easily written in a diagonal basis. With a proper transformation of the Fermi fields as in equation (2.29), the free Hamiltonian becomes

$$\mathbf{H}^0(k) = I_S \otimes [d_I(k)I + d'_z(k)\sigma_z] , \quad (3.4)$$

with $d'_z = \sqrt{d_x^2 + d_z^2}$. The band-structure of the model consists of two parabolas, which have a QBCP at the origin (see figure 3.1). In our choice $t_x = t_z = t$, the dispersion is rotationally invariant in the plane.

The interacting part of the Hamiltonian contains local intra- and interorbital repulsions,

$$\begin{aligned}
 H_{\text{int}} = & \frac{U}{2} \sum_{o,\sigma \neq \sigma'} \int dk dk' dq \psi_{o,\sigma}^\dagger(k+q) \psi_{o,\sigma'}^\dagger(k'-q) \psi_{o,\sigma'}(k') \psi_{o,\sigma}(k) \\
 & + \frac{U'}{2} \sum_{o \neq o', \sigma, \sigma'} \int dk dk' dq \psi_{o,\sigma}^\dagger(k+q) \psi_{o',\sigma'}^\dagger(k'-q) \psi_{o',\sigma'}(k') \psi_{o,\sigma}(k). \quad (3.5)
 \end{aligned}$$

As pointed out in Ref. [Sun09], the QBCP carries a vortex-like winding of the Bloch eigenvectors (with two components for the amplitudes in the two orbitals) that cannot be made undone continuously. The core of the vortex needs to be a degeneracy point, and, hence, the QBCP cannot be removed easily. When we think about the stability of the QBCP with respect to interactions, there are essentially two ways to remove the QBCP [Sun09] which we will find to be realized depending on the interaction parameters. The free Hamiltonian has rotational invariance in the k_x, k_y -plane. One way is now to break this rotational symmetry by splitting the QBCP into two Dirac points [Sun09]. In terms of the eigenvectors this stretches out the winding along a branch cut connecting the two Dirac points with an inversion of the direction of the Bloch eigenvectors. The other way is to open a gap by breaking either time reversal symmetry in a given spin sector [Sun09]. This corresponds to a non-zero d_y -term. Only when the d_y s in spin-up and spin-down sectors are opposite in sign but of the same magnitude, time-reversal symmetry is still present. This state is then a QSH state. Otherwise, time-reversal symmetry is broken. If d_y is spin-independent, we have a QAH state.

In the following, we study the instabilities of the continuum QBCP model detailed above and of a related lattice variant (see section 3.5) in the spin-1/2 case by a fRG approach. This extends the mean-field study of Sun et al. [Sun09] of a spinless model. We find that a single QBCP might be the most favorable situation to realize spontaneous QSH instabilities. Compared to previous studies, for instance in the honeycomb single layer [Rag08], neither particular longer ranged interactions are needed, and no threshold value for the interaction strength needs to be exceeded.

3.3 Functional Renormalization Group Treatment

We apply the fRG method detailed in chapter 2. For easier numerical feasibility, we will neglect the flow of the three-particle vertex and the self-energy and discard the frequency dependence of the interaction vertex, by setting all external frequencies to zero, as discussed in sections 2.4 and 2.6.

The summation over the Brillouin zone is computed numerically within the N -patch scheme, in which the coupling function is computed on a finite set of wavevectors in the Brillouin zone [ZS00; Hon01]. Usually these wavevectors

are chosen to be located at the Fermi surface, neglecting the variation of the vertex perpendicular to the Fermi surface. Here, however, at half-filling, the Fermi surface consists of only one point namely the QBCP. For our calculation in band basis, we have to employ equation (2.30), to calculate the interaction vertex at the initial scale. However, as mentioned above, the QBCP exhibits a vortex-like winding of the Bloch eigenvectors, and, thus, the transformation at the QBCP is ill-defined, i.e. it depends on the direction from which one approaches the QBCP. To account for the winding of the Bloch eigenvectors, we choose the set of momenta, at which the coupling function is computed, to be on a ring around the QBCP. A similar approach has been taken in the study of single layer graphene. Here, the band-structure exhibits two linear band crossing points and the fRG treatment, with representative momenta of the patches set on a ring around the Fermi point gives reasonable results [Rag08; Hon08].

We have checked that additional radial patches, as well as changing the radius of the ring, at which the coupling function is calculated, do not change the qualitative results for the continuum model at half-filling. In the study of the lattice model in section 3.5 we introduce additional radial patches (i.e. a second ring). This is done for a better resolution of the non-local order parameter (see appendix A). In section 3.6, we will consider the system away from half-filling. Here, we set the representative momenta of the patches at the Fermi level, as in previous studies on models with an extended Fermi surface (e.g. [Hon01]). In order to determine the symmetry channel of the leading superconducting instability, we again employ a patching scheme with additional radial patches.

The fRG calculation is performed in the band basis, in which the free part of the Hamiltonian is diagonal, as written in equation (3.4). Therefore, we transform the interacting part accordingly, as detailed in section 2.7. We pointed out, that the transformation from orbital to band basis is not unique, as the eigenvector of the quadratic part of the Hamiltonian at a given point in momentum space, is only defined up to a prefactor. In section 2.7, we discussed that for an exact calculation the result does not depend on this choice. However, due to the patching scheme, which we employ here, the accuracy of the method is reduced, if the interaction vertex exhibits discontinuities in the momentum dependence. We, therefore, make use of this freedom of choice, to reduce this error. In the continuum model any discontinuities can be avoided by the choice

$$u_{1,A}(k) = \frac{k_x}{|k|}, \quad u_{1,B}(k) = \frac{k_y}{|k|} \quad (3.6)$$

$$u_{2,A}(k) = \frac{k_y}{|k|}, \quad u_{2,B}(k) = \frac{-k_x}{|k|}, \quad (3.7)$$

with $|k| = \sqrt{k_x^2 + k_y^2}$ and $b = 1(2)$ denoting the upper (lower) band. The eigenvectors are independent from the distance to the QBCP and wind about 360° , when one goes once around the QBCP. An analogous choice is employed

in the lattice model of section 3.5, to avoid discontinuities in the winding around the QBCP.

It is natural to transform the interaction vertex back into the original basis, after the fRG flow has been calculated. This allows for a straightforward interpretation of the orbital dependence of the effective interaction and the corresponding order parameter.

The fRG flows are calculated at $T = 0$, so that we typically encounter diverging interactions at some critical scale Λ_c . If the flow of the fermionic self-energy was included, a gap would open at the instability scale. This would regularize the divergence at non-zero scale. Unfortunately, such flows into the symmetry-broken or massive sector are by far more complicated, when the competition of various instabilities or fermionic gaps is kept, which is our goal here. It gets more feasible when only one type of fermion gap is considered [Sal04]. A work by Sinner and Ziegler [SZ10] shows how the fRG in partially bosonized form (this formalism is e.g. reviewed in [Met12]) can be used to determine the final interacting gaps in single and bilayer graphene with Coulomb interactions, when all modes are integrated out.

Lastly, we remark that in the continuum model detailed in the preceding section 3.2 the UV cutoff, i.e., the starting scale Λ_0 , is somewhat arbitrary, as the model is understood as an effective low energy model of a lattice system. Therefore, we choose some fixed UV cutoff. The explicit calculations confirm the expectation that this choice only affects the absolute value of the critical scale, but not the type of instability. The prefactor $1/V_{BZ}$ in the flow equations (2.19 – 2.23) is replaced by the corresponding $1/\Omega$, with Ω being the surface area of the considered disk in momentum space.

3.4 Phase Diagram of the Continuum Model

We investigate the diverging tendencies of the fRG flow of the effective interaction for different ratios of U and U' for the QBCP at the Fermi level. The main growth is in particle-hole channels with zero momentum transfer, leading to very sharp structures in the effective interactions (see figures 3.2, 3.3, 3.4). If we focus on this dominant zero-momentum transfer component and drop the remaining interaction terms, the effective interaction becomes infinitely long-ranged in real space and decomposes into a product of two fermion bilinears, each with one creation and one annihilation operator at the same wavevector. This interaction can then be solved in mean-field theory. Then, the bilinears correspond to order parameters of the strongly coupled phase, the emergence at low scales of which is indicated by the flow to strong coupling.

In the following, we want to elucidate this procedure in more detail, by first considering specifically the SN phase, which is dominant for $U' \lesssim U/2$ as we will see below. If we run the fRG flow in this regime and stop at Λ_c , when the couplings exceed a value of three times the bandwidth, we discover that the

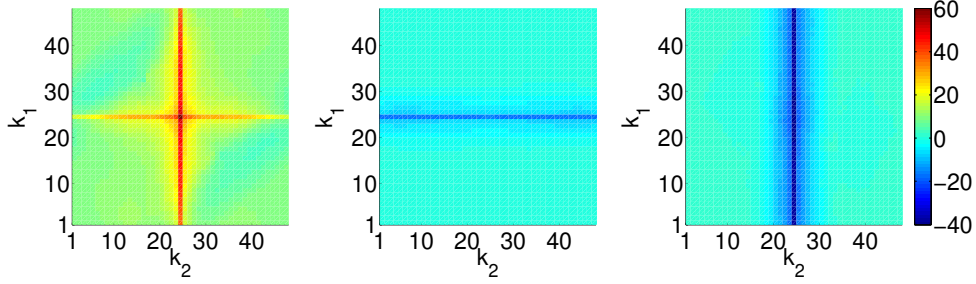


Figure 3.2: Effective interaction near the critical scale in the SN phase in units of t . The patch k_1 (k_2) of the first (second) ingoing leg is plotted on the y (x) axis, with the discretization shown in figure 3.1. $k_3 = 24$ is kept fixed. In our convention, the first and the third leg have the same spin. The first plot shows the vertices with the orbitals $o_1 = o_2 = o_3 = o_4$, the second plot shows the combination $o_1 = o_3 \neq o_2 = o_4$ and the third plot shows $o_1 = o_4 \neq o_2 = o_3$.

momentum dependence of the interaction vertex exhibits very sharp features. The precise value of this termination parameter does not matter with regard to the qualitative features of the interaction vertex, as long as it is larger than the bandwidth. In figure 3.2, we show a typical plot of the effective interaction at the critical scale in the SN phase. One nicely observes the sharp momentum dependence of the vertices. A certain set of coupling constants diverge, whereas, most of the couplings remain small. If we only keep the diverging tendencies, the interaction vertex, which depends on three momenta k_1, k_2, k_3 and 4 orbital indices o_1, \dots, o_4 , can in the case of the SN instability be written as

$$V_{\text{SN}}(k_1, o_1, k_2, o_2, k_3, o_3, o_4) = C \varepsilon_{o_1} \varepsilon_{o_2} (\delta_{o_1, o_3} \delta_{o_2, o_4} \delta_{k_1, k_3} + 2 \delta_{o_1, o_4} \delta_{o_2, o_3} \delta_{k_2, k_3}), \quad (3.8)$$

where C is a positive constant, which depends on the scale, at which the flow is stopped and is not of further interest and $\varepsilon_A = 1$, $\varepsilon_B = -1$ is an orbital-dependent sign factor.

The first (second) term corresponds to the horizontal (vertical) features in figure 3.2. If we assume that the features of the interaction vertex are peaked at exactly zero momentum transfer, we can rewrite the effective Hamiltonian at Λ_c as a spin-spin interaction in continuous momentum space

$$H_{\text{SN}} = - \sum_{o, o'} J_{\text{SN}} \varepsilon_o \varepsilon_{o'} \vec{S}_o \vec{S}_{o'}, \quad (3.9)$$

with

$$\vec{S}_o = \frac{1}{2} \sum_{\sigma, \sigma'} \int dk \vec{\tau}_{\sigma\sigma'} \psi_{o, \sigma}^\dagger(k) \psi_{o, \sigma'}(k). \quad (3.10)$$

Here $J_{\text{SN}} > 0$ and $\vec{\tau}$ are the Pauli matrices representing the spin degree of free-

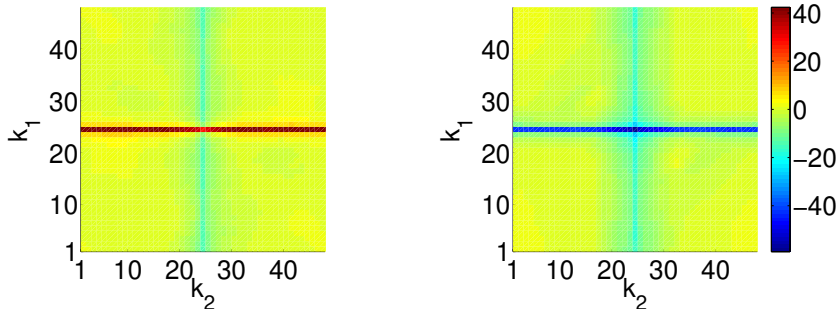


Figure 3.3: Effective interaction near the critical scale in the QAH phase in units of t . The patch k_1 (k_2) of the first (second) ingoing leg is plotted on the y (x) axis, with the discretization shown in figure 3.1. $k_3 = 24$ is kept fixed. In our convention, the first and the third leg have the same spin. The first plot shows the vertices with the orbitals $o_1 = o_2 \neq o_3 = o_4$, the second plot shows the combination $o_1 = o_4 \neq o_2 = o_3$. The weaker vertical features at $k_2 = k_3$ belong to remnants of the QSH instability (first plot) and SN instability (second plot), respectively.

dom and we used the identity [SH01] $\vec{\tau}_{\sigma_1\sigma_3}\vec{\tau}_{\sigma_2\sigma_4} = -\delta_{\sigma_1,\sigma_3}\delta_{\sigma_2,\sigma_4} + 2\delta_{\sigma_1,\sigma_4}\delta_{\sigma_2,\sigma_3}$.

This is an infinitely long-ranged spin-spin interaction, which is, due to the sign factors $\varepsilon_o, \varepsilon_{o'}$ of ferromagnetic type within the same orbital, and of anti-ferromagnetic type between the orbitals. This effective interaction favors the emergence of the order parameter

$$\begin{aligned} \vec{Q}_{\text{SN}} &= \int dk \sum_{\sigma,\sigma'} \langle \vec{\tau}_{\sigma\sigma'} [\psi_{A,\sigma}^\dagger(k)\psi_{A,\sigma'}(k) - \psi_{B,\sigma}^\dagger(k)\psi_{B,\sigma'}(k)] \rangle \\ &= \int dk \langle \Psi(k) (\vec{\tau} \otimes \sigma_z) \Psi(k) \rangle, \end{aligned} \quad (3.11)$$

where the brackets $\langle \dots \rangle$ denote thermal averages. The state with non-vanishing \vec{Q}_{SN} is characterized by a mean-field that is odd in both, the two orbitals and in the spin projection along, e.g., the z axis. For a given spin component, the QBCP splits into two Dirac points, either along the k_x axis or along the k_y axis. For the opposite spin projection, the dispersion is rotated by 90° . The translational symmetry however remains conserved. Therefore, this state exhibits SN order (see [Sun09]).

We also found an instability towards the emergence of a QAH order parameter. Here, the effective interaction can be written in analogy with equation (3.8) as

$$V_{\text{QAH}}(k_1, o_1, k_2, o_2, k_3, o_3, o_4) = C \delta_{k_1, k_3} \left(\delta_{o_1, o_2} \delta_{o_3, o_4} - \delta_{o_1, o_4} \delta_{o_2, o_3} \right), \quad (3.12)$$

where C is again a positive constant not of further interest (see figure 3.3).

The less pronounced vertical features in figure 3.3 correspond to a tendency toward the emergence of the QSH phase in the left and the SN phase in the right plot, which are still present but weaker than the leading QAH instability. The corresponding two-particle vertex is deduced similar to the nematic phase to be

$$H_{\text{QAH}} = \sum_{o_1, o_2, o_3, o_4} \tilde{V}_{\text{QAH}} \zeta_{o_1, o_3} \zeta_{o_2, o_4} n_{o_1, o_3} n_{o_2, o_4}, \quad (3.13)$$

with $\tilde{V}_{\text{QAH}} > 0$, $\zeta_{A,B} = 1$, $\zeta_{B,A} = -1$, $\zeta_{A,A} = \zeta_{B,B} = 0$ and

$$n_{o, o'} = \sum_{\sigma} \int dk \psi_{o', \sigma}^{\dagger}(k) \psi_{o, \sigma}(k). \quad (3.14)$$

A lowering of the free energy in the presence of this type of interaction is accomplished by a non-zero expectation value of the QAH order parameter

$$\begin{aligned} \Phi_{\text{QAH}} &= \int dk \sum_{\sigma} \langle i [\psi_{B, \sigma}^{\dagger}(k) \psi_{A, \sigma}(k) - \psi_{A, \sigma}^{\dagger}(k) \psi_{B, \sigma}(k)] \rangle \\ &= \int dk \langle \Psi^{\dagger}(k) (I \otimes \sigma_y) \Psi(k) \rangle. \end{aligned} \quad (3.15)$$

Note how the different sign of the couplings with $o_1 = o_2$ and $o_1 \neq o_2$ directly leads to the fact, that the expectation value of $\psi_{A, \sigma}^{\dagger}(k) \psi_{B, \sigma}(k)$ is imaginary. The product of the two bilinears yields a positive contribution, if $o_1 = o_2 \neq o_3 = o_4$ and a negative contribution if $o_1 = o_4 \neq o_2 = o_3$, which is only possible, if $\langle \psi_{A, \sigma}^{\dagger}(k) \psi_{B, \sigma}(k) \rangle$ and $\langle \psi_{B, \sigma}^{\dagger}(k) \psi_{A, \sigma}(k) \rangle$ have opposite signs and thus must be imaginary, as the terms are the complex conjugates of one another.

The QAH order parameter Φ_{QAH} represents an imaginary hopping amplitude between the two types of fermions, i.e. orbitals. Due to this imaginary hopping, time reversal symmetry is broken. This state has a gapped bulk spectrum, as can be found out from adding the mean-field to the free Hamiltonian. Also, it has a quantized Hall conductivity and topologically protected edge states, as can be understood, e.g. by computing the Hall conductivity from the skyrmion-number formula and by looking at finite systems in real space [QWZ06], as detailed in section 3.1.

Lastly, we found the QSH instability corresponding to the momentum and orbital dependence of the interaction vertex plotted in figure 3.4. Similar to the SN and QAH instability we can state the form of the interaction vertex, taking only the leading instabilities into account

$$\begin{aligned} V_{\text{QSH}}(k_1, o_1, k_2, o_2, k_3, o_3, o_4) &= C \left(-\delta_{o_1, o_2} \delta_{o_3, o_4} (\delta_{k_1, k_3} + 2\delta_{k_2, k_3}) \right. \\ &\quad \left. + \delta_{o_1, o_4} \delta_{o_2, o_3} \delta_{k_1, k_3} + 2\delta_{o_1, o_3} \delta_{o_2, o_4} \delta_{k_2, k_3} \right), \end{aligned} \quad (3.16)$$

with $C > 0$, which leads to the effective Hamiltonian

$$H_{\text{QSH}} = \sum_{o_1, o_2, o_3, o_4} \tilde{V}_{\text{QSH}} \zeta_{o_1, o_3} \zeta_{o_2, o_4} \vec{S}_{o_1, o_3} \vec{S}_{o_2, o_4}, \quad (3.17)$$

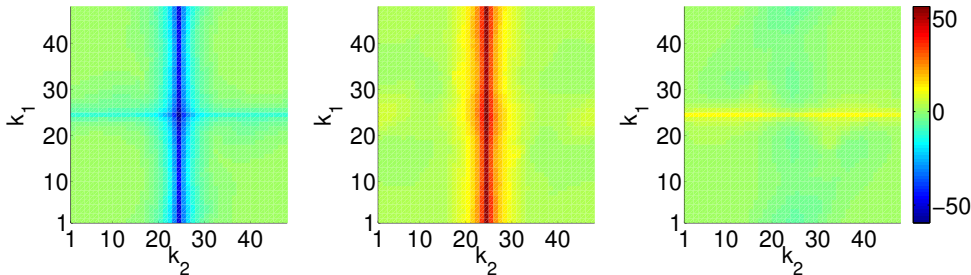


Figure 3.4: Effective interaction near the critical scale in the QSH phase in units of t . The patch k_1 (k_2) of the first (second) ingoing leg is plotted on the y (x) axis, with the discretization shown in figure 3.1. $k_3 = 24$ is kept fixed. In our convention, the first and the third leg have the same spin. The first plot shows the vertices with the orbitals $o_1 = o_2 \neq o_3 = o_4$, the second plot shows the combination $o_1 = o_3 \neq o_2 = o_4$ and the third plot shows $o_1 = o_4 \neq o_2 = o_3$. The horizontal features are somewhat weakened compared to the expected values of about half the amplitude of the vertical features, due to the competing QAH tendency, which has a feature with opposite sign at $k_1 = k_3$.

with $\tilde{V}_{\text{QSH}} > 0$, ζ_{o_1, o_2} as above and

$$\vec{S}_{o, \sigma'} = \sum_{\sigma, \sigma'} \int dk \vec{\tau}_{\sigma \sigma'} \psi_{\sigma', \sigma}^\dagger(k) \psi_{o, \sigma'}(k). \quad (3.18)$$

The corresponding mean field order parameter reads

$$\begin{aligned} \vec{\Phi}_{\text{QSH}} &= \int dk \sum_{\sigma, \sigma'} \langle \vec{\tau}_{\sigma \sigma'} i [\psi_{B, \sigma}^\dagger(k) \psi_{A, \sigma'}(k) - \psi_{A, \sigma}^\dagger(k) \psi_{B, \sigma'}(k)] \rangle \\ &= \int dk \langle \Psi^\dagger(k) (\vec{\tau} \otimes \sigma_y) \Psi(k) \rangle. \end{aligned} \quad (3.19)$$

Like in the QAH case an imaginary order parameter emerges, which is, however, now spin-dependent. Here, spin projection along, e.g., the z-axis is conserved, so that the QSH state can be understood as a QAH state, but, with opposite signs for each spin projection. The two copies are time reversal partners, so that the whole system is time reversal invariant but breaks spin rotational symmetry. It has a gapped bulk spectrum and helical edge states, which result in quantized spin Hall conductivity (see [Sun09; HK10]).

Now, let us discuss the parameter regions where these orders emerge in the continuum model in more detail. When we run the fRG with the local interaction parametrized by U and U' as initial conditions, we find different effective interactions dominated by the three types of ordering listed above in equations (3.11, 3.15, 3.19) as a function of U'/U . From analyzing which component of

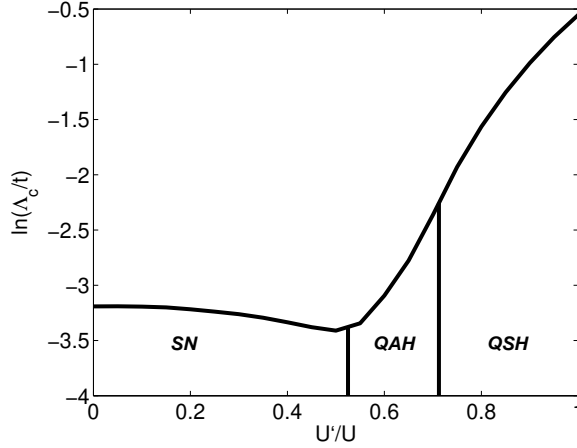


Figure 3.5: Tentative fRG phase diagram of the continuum model as a function of the interorbital interaction parameter U' in units of the intraorbital repulsion. Λ_c denotes the critical scale, defined as the scale, at which the couplings exceed three times the bandwidth, obtained with a fRG calculation using $N = 48$ patches per band, upper cutoff $\Lambda_{UV} = 10t$ and $U = 8t$.

these three grows most strongly, we can deduce a tentative phase diagram describing the leading ordering tendencies. Here, the critical scale Λ_c serves as an (upper) estimate for possible ordering temperatures, or at least for the onset of strong correlations of the type indicated. Note that the question as to whether these orderings actually occur in true long-range form or are prohibited by, e.g., collective fluctuations is not answered in this fRG scheme. Nevertheless, the analysis is expected to give a realistic account of the dominant non-local correlations. Another interesting possibility would be that the single particle Hamiltonian already contains small terms corresponding to the addressed mean fields, e.g., due to spin-orbit coupling, and that these terms then get strongly enhanced at low temperatures due to the interaction effects monitored by the fRG.

The phase diagram obtained for the QBCP model is shown in figure 3.5. For small values of the interorbital repulsion U' we encounter the SN phase with suggested order parameter (3.11). For $U' \gtrsim U/2$ the QAH-order parameter (3.15) is leading and above $U' \gtrsim 0.7U$ the system is unstable toward the QSH-order (3.19).

Upon changing U'/U , Λ_c does not decrease significantly between different phases. This suggests that there is no direct competition between the different tendencies, and the phase transitions are first order.

In order to answer the question as to whether there is a critical interaction strength needed for the emergence of long-range order, we also investigated the critical scale in dependence of the bare coupling strength for fixed U'/U in all

three regimes. We observed that the couplings do, indeed, diverge down to an interaction strength of less than $U = 2t$ for a bandwidth of $20t$. Although an arbitrary small interaction strength is not numerically accessible, we expect the instability to persist to infinitesimally small interaction due to the finite density of states, see also appendix B.

The conclusion we can draw from this study is that this QBCP model is a favorable situation for the occurrence of spontaneous spin Hall instabilities. No particularly strong or exotic interaction is needed, and the ratio $U'/U \leq 1$ between interorbital and intraorbital interactions should not be too unrealistic.

Note that the d -wave-like wavevector dependence of the components of the free Hamiltonian and its off-diagonal content that lead to a wavevector-variation of the Bloch eigenvectors, are essential for obtaining these interesting instabilities. If one just takes a Hamilton matrix $\mathbf{H}^0(k) \propto k^2 \sigma_z$, that leads to the same dispersion but constant Bloch eigenvectors, the initial condition for the fRG flow is changed and we do not encounter the nematic or the topologically non-trivial phases presented here.

3.5 Model on a Checkerboard Lattice

For possible realizations of the unconventional particle-hole instabilities found in the preceding section, it would further be advantageous to have a lattice model that shows similar physics. In this section, we want to analyze a QBCP on a checkerboard lattice, which has two sublattices A and B playing the role of the orbital degree of freedom in the last section. This model was already studied by Sun et al. in mean-field theory for spinless fermions [Sun09]. Here, we treat the spinfull case with the fRG. The free Hamiltonian is still of the form of equations (3.2, 3.3), but with the new hopping terms

$$\begin{aligned} d_I &= 2t_I(\cos k_x + \cos k_y) - \mu, \\ d_x &= 8t_x \cos \frac{k_x}{2} \cos \frac{k_y}{2}, \\ d_z &= 2t_z(\cos k_x - \cos k_y). \end{aligned} \tag{3.20}$$

Here, the lattice constant has been set to unity. t_x corresponds to hopping between nearest neighbors and t_I and t_z correspond to hopping between next-nearest neighbors, that is nearest neighbors on the same sublattice. If we again set $t_I = 0$, then the hoppings between next-nearest neighbors connected by a line in figure 3.6 and not connected by a line have opposite sign. We also set $t_x = t_z = t$ and $\mu = 0$ as before. This lattice model has a QBCP in the corner of the Brillouin zone (π, π) and, in its vicinity, the lattice model assumes the form of the continuum model in section 3.2 (see [Sun09]). The dispersion is shown in the right panel of figure 3.6. Further away from the band crossing, the dispersion breaks rotational symmetry around (π, π) .

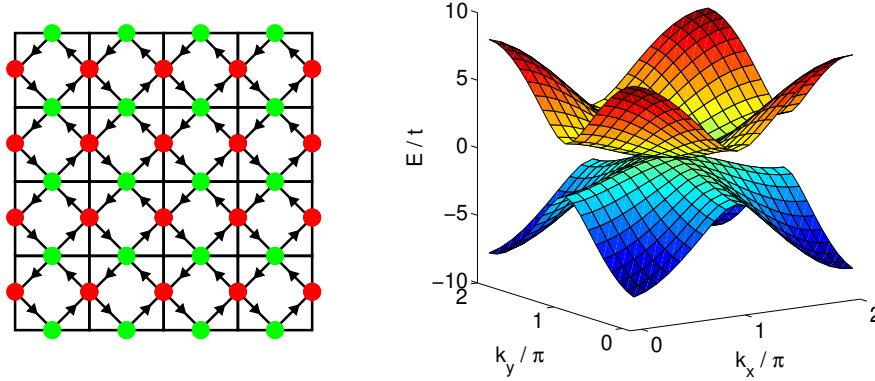


Figure 3.6: Left: Sketch of the Checkerboard lattice with two sublattices A and B indicated by the two different colors. The arrows indicate the current pattern in the QAH and QSH phase. In the QSH phase the current for opposite spins is reversed (modified according to [Sun09]). Right: Dispersion of the lattice Hamiltonian specified in equation (3.20).

We consider an on-site repulsion U and a spin-independent nearest-neighbor repulsion, thus, the interaction part of the Hamiltonian reads as

$$\begin{aligned}
 H_{\text{int}} = & \frac{U}{2\mathcal{N}} \sum_{\substack{k,k',q \\ o,\sigma \neq \sigma'}} \psi_{o,\sigma}^\dagger(k+q) \psi_{o,\sigma'}^\dagger(k'-q) \psi_{o,\sigma'}(k') \psi_{o,\sigma}(k) \\
 & + \frac{U'}{4\mathcal{N}} \sum_{\substack{k,k',q \\ o \neq o',\sigma,\sigma'}} \left(\cos \frac{q_x + q_y}{2} + \cos \frac{q_x - q_y}{2} \right) \\
 & \times \psi_{o,\sigma}^\dagger(k+q) \psi_{o',\sigma'}^\dagger(k'-q) \psi_{o',\sigma'}(k') \psi_{o,\sigma}(k), \quad (3.21)
 \end{aligned}$$

where \mathcal{N} is the number unit cells and we included an additional factor $1/4$ in the second term to compensate that each lattice site has 4 neighboring sites, so that the results are directly comparable to the continuum model.

We carry out the fRG analysis described in section 3.3. Again, for small U'/U we encounter a SN phase which has the same order parameter as in the continuum model given by equation (3.11). The mean fields of the QAH and QSH phases suggested by the fRG, however, have an additional prefactor due to the local separation of the orbitals. Similar as in [Sun09] they can be written as

$$\begin{aligned}
 \Phi_{\text{QAH}} = & \sum_k \left\langle \Psi^\dagger(k) (I \otimes \sigma_y) \Psi(k) \left(-2 \sin \frac{k_x}{2} \sin \frac{k_y}{2} \right) \right\rangle \\
 = & \frac{1}{2} \sum_{j,\delta,\sigma} \langle i D_\delta [\psi_{B,\sigma}^\dagger(j+\delta) \psi_{A,\sigma}(j) - \psi_{A,\sigma}^\dagger(j) \psi_{B,\sigma}(j+\delta)] \rangle, \quad (3.22)
 \end{aligned}$$

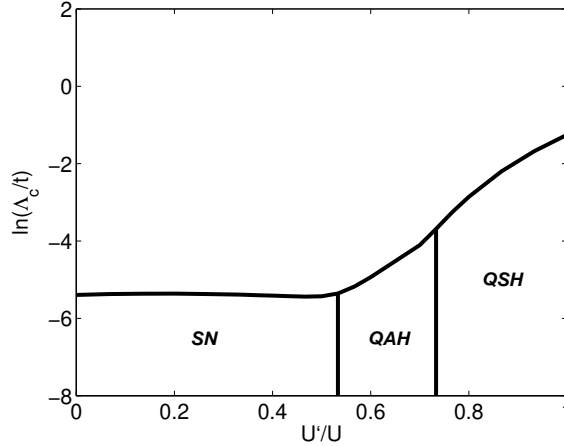


Figure 3.7: Phase diagram of the lattice model as a function of the interorbital interaction parameter U' , in units of the intraorbital repulsion $U = 6t$. Λ_c denotes the critical scale, defined as the scale, at which the couplings exceed four times the bandwidth, obtained with a fRG calculation using $N = 48$ patches per band.

$$\begin{aligned} \vec{\Phi}_{\text{QSH}} &= \sum_k \left\langle \Psi^\dagger(k) (\vec{\tau} \otimes \sigma_y) \Psi(k) \left(-2 \sin \frac{k_x}{2} \sin \frac{k_y}{2} \right) \right\rangle \\ &= \frac{1}{2} \sum_{j, \delta, \sigma, \sigma'} \langle \vec{\tau}_{\sigma\sigma'} i D_\delta [\psi_{B,\sigma}^\dagger(j+\delta) \psi_{A,\sigma'}(j) - \psi_{A,\sigma}^\dagger(j) \psi_{B,\sigma'}(j+\delta)] \rangle, \end{aligned} \quad (3.23)$$

with j denoting the lattice sites of sublattice A , $\delta = \pm \frac{x}{2} \pm \frac{y}{2}$, $D_{\pm(\frac{x}{2} + \frac{y}{2})} = 1$ and $D_{\pm(\frac{x}{2} - \frac{y}{2})} = -1$. Here, we introduced additional radial patches for a better resolution of the momentum-dependent variation in equations (3.22, 3.23). In close vicinity to the QBCP, the prefactor is nearly constant and thus cannot be observed, if only one ring of patching points close to the QBCP is used, however, by introducing a second ring of patching points, with greater distance to the QBCP the momentum dependence is detected. Details are given in appendix A.

Note that the topological non-trivial phases do not violate local charge conservation despite their unusual appearance. It can be shown that the expectation value of the fermion number operator at a given coordinate remains constant. The current pattern in the QAH state is indicated by the arrows shown in figure 3.6. In the QSH state, we get the same pattern for one spin component, but, here, the current for the other spin component is reversed.

The phase diagram of the lattice model is shown in figure 3.7. It is similar to the one of the continuum model, both phase transitions occur at similar U'/U -ratio. As expected, the difference between the two models, which lies only in the high energy modes, does not play an essential role for the determination of the leading instability.

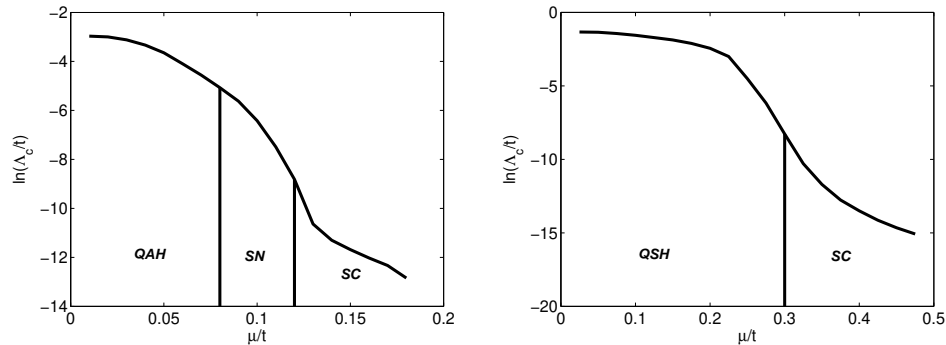


Figure 3.8: Phase diagram of the continuum model as a function of the chemical potential μ at $U'/U = 0.55$ (left) and $U'/U = 0.75$ (right). Λ_c denotes the critical scale, defined as the scale, at which the couplings exceed three times the bandwidth, obtained with a fRG calculation using $N = 48$ patches per band, upper cutoff $\Lambda_{UV} = 10t$ and $U = 8t$.

3.6 Flows at Non-Vanishing Chemical Potential

We now want to investigate the instabilities of the QBCP at a finite value of the chemical potential, so that the QBCP is shifted away from the Fermi surface. We mainly consider the continuum model of section 3.2. However, we checked that the results remain qualitatively similar in the checkerboard lattice of the preceding section.

The natural choice for the patching points of the discretization scheme is to set them on the circular Fermi surface that opens upon changing the chemical potential away from zero, as we are interested in the effective model at low energy. We choose the patching points of the other band without Fermi surface to be at the same positions in momentum space. Again, we also used a momentum discretization with additional radial patches.

In all three regimes, we find a critical chemical potential μ_{crit} , above which, the leading instability is superconducting. This means that the leading divergence is now for momentum combinations that have total incoming momentum, $k_1 + k_2 = 0$ (assuming that the QBCP is at the origin in momentum space). Typical phase diagrams are shown in figure 3.8. We see that the critical scale drops for larger μ .

A further interesting result is, that in the regime, where we get the QAH for $\mu = 0$, there is always an intermediate phase, either SN or QSH type, before the superconducting channel becomes strongest. The leading instability of the intermediate phase is determined by the ratio of U' and U : above $U'/U = 0.6$, it is QSH and below it is SN.

We also addressed the question as to which type of pairing symmetry can be associated to the superconducting instability. It turns out that this question can not be conclusively answered within our approach. Depending on numerical

details, in particular, the discretization scheme (i.e., use of one or more radial patches), we obtain two different results, which are most plausible according to our data and which both have an orbital dependence of the order parameter. In the first case, the pairing has an interorbital s -wave-like component and a d -wave-like intraorbital component. The second, nearly degenerate, possibility is an odd-parity, i.e., triplet pairing, symmetry that is p -wave-like in all orbital combinations, which has relative phase shifts between the orbital components. From our data, it seems that different superconducting channels are competing, so that numerical details decide which one is leading. As the model studied here has so far not been realized experimentally, we refrain from a classification of the pairings in this two-orbital situation and from elaborating this situation with refined numerics further. However, a general conclusion from this study is that, upon doping, the interaction-driven instabilities in such QBCP systems generically give way to unconventional superconducting phases.

3.7 Conclusion

In summary, we have investigated the weak coupling instabilities of the QBCP in a two-dimensional fermionic spin-1/2 system with an angle-resolved fRG calculation. Comparing the leading instability for different ratios of intraorbital and interorbital interactions, we obtained similar results for the continuum model and the model on a checkerboard lattice. For weak interorbital interaction, the system is unstable toward a SN phase. For intermediate U' , we encounter the time-reversal-symmetry breaking QAH phase, and for a strong interorbital repulsion, the leading tendency is toward the topological non-trivial QSH phase. Upon moving the chemical potential away from the band crossing point, the exotic instabilities are replaced by unconventional pairing instabilities at lower critical scale.

Our results with the QBCP at the chemical potential confirm the conclusion from the mean-field analysis by Sun et al. [Sun09], mainly obtained for the spinless case. They show that the dominant weak-coupling instabilities of a many-fermion system are not only determined by the shape of the dispersion, but that also the wavevector-dependent orbital composition of the bands has a decisive impact on the preferred ordering tendency. This holds as well for linear band crossing points, i.e. Dirac points. Here, however, the density of states vanishes at the Fermi level, and non-zero, possibly too large interactions strengths are required to find instabilities.

Further research should address where quadratic and other band crossing points can be found in realistic band-structures near the Fermi level, in order to investigate their potential instabilities. In the next part of this work, we will report on a fRG analysis on bilayer graphene, that is known to provide two QBCPs at the K and K' points of the Brillouin zone [Cas09], at least if trigonal warping is ignored. Naively, one might suspect that the bilayer case

of two QBCPs with short-range interactions will be dominated by instabilities with the wavevector connecting the degeneracy points, leading to density wave states, as found in a related approach by Vafeek [Vaf10]. We will see in the next chapter, that we find indeed a CDW instability, with momentum transfer connecting the two QBCPs. However, in the parameter range suggested by ab initio calculations [Weh11], instabilities with zero momentum transfer, such as AFM-SDW and QSH instability are leading. The study with a single band crossing connects well to these findings and confirms that if the two crossing point regions are not at all connected by scattering, QSH instabilities are possible for realistic interaction parameters.

Chapter 4

Instabilities of Interacting Electrons on the Honeycomb Bilayer

We investigate the instabilities of interacting electrons on the honeycomb bilayer for different interaction parameters. Besides a novel instability toward a CDW we find that using interaction parameters as determined by ab initio calculations for graphene and graphite puts the system close to the boundary between AFM and QSH instabilities. We compare the energy scales of the instabilities to QMC data. As the scales are large compared to experimentally found gaps, we analyze how reducing the critical scale and small doping of the layers affect the instabilities.

Large parts of this chapter have previously been published in [SUH12; Lan12].

Contents

4.1	Introduction	45
4.2	Model	47
4.3	Functional Renormalization Group Treatment	51
4.4	Phase Diagram of the Honeycomb Bilayer	53
4.5	Critical Scale of the Instabilities	59
4.6	Inclusion of Long-Ranged Interaction	61
4.7	Conclusion	63

4.1 Introduction

With the preparation of graphene in few or even a single atomic layer [Nov04], a new field in experimental and theoretical research has evolved. Graphene in few layers exhibits quite unusual band-structures, featuring a Fermi surface, which consists approximately of isolated band crossing points. For instance in the case of single layer graphene, the dispersion relation has two linear band crossing points, i.e., Dirac points. For a detailed discussion, we refer to the reviews by Castro Neto et al. [Cas09] and by McCann et al. [MK12] on bilayer graphene. Geim et al. [GN07] focus on the experimental characteristics and [Kot12] deals with correlation effects on single and bilayer graphene.

Theoretical works addressed the question, whether single layer graphene exhibits a correlated ground state, by studying models on a two-dimensional honeycomb lattice. The emergence of CDW and SDW type instabilities and exotic superconducting phases has been considered in [UCN07; Hon08; Kie12; Wan12]. An interesting possibility is also the emergence of a spin liquid state, which is found in QMC calculations at half-filling [Men10; HLA11]. In the work of Raghu et al. [Rag08], a phase diagram of interacting electrons on the honeycomb lattice at charge neutrality has been obtained via mean-field and fRG calculation, which is similar to the method employed in the present work. Besides instabilities towards SDW AFM and CDW order, a QSH state has been found to be leading for large next-nearest-neighbor interaction strength. Due to the linear dispersion a finite interaction strength is needed to induce a correlated ground state. So far, experiments were not able to detect signatures of a correlated ground state in single layer graphene, indicating, that the interactions strength in the actual system is too weak.

In this chapter, we focus on bilayer graphene at the charge neutrality point. As opposed to the single layer, the band crossing points of bilayer graphene are quadratic, if only nearest-neighbor hopping is included (see also [Cas09; MK12]). They exhibit a winding of the Bloch eigenvectors similar to the models of the preceding chapter. As opposed to the single layer, the density of states at the Fermi level is finite, so that one can expect from mean field or random phase approximation (RPA) that instabilities occur already at small interaction strength (see appendix B).

Several experiments have found signatures of a symmetry broken ground state [FMY09; Mar10; Wei10; May11; Vel12a; Fre12; Bao12; Vel12b]. Many of these experiments identified a finite excitation gap of the order of a few meV emerging at low temperatures in ultra-clean samples [Vel12a; Fre12; Bao12; Vel12b]. The authors of [Vel12a] state that their results are not compatible with QAH or QSH phase, as there are no signs of edge states. More plausible according to these findings seems to be the AFM state, which is consistent with the conclusion drawn in [Vel12b]. Moreover, the dependence on the magnetic field found in [Vel12a] has been reproduced by Kharitonov, within a mean-field calculation of the AFM state [Kha12]. On the other hand, transport data in [May11] have been interpreted towards the formation of a gapless nematic state, which is in contradiction to most of the other works. In view of these experimental observations, the nature of the ground state still remains highly debated.

The question, which type of ordered ground state might be realized, has been addressed in numerous works. Among others, cited below, we mention here [Min08; NL10b; Zha10a; JZM11; Zha11a; ZMM12; MJZ12]. An external electric field perpendicular to the bilayer graphene sheet can induce an instability towards a state with charge polarized layers, which is discussed in, e.g., [MAF07; NL10a; Gor12; CTV12]. Here, however, we focus on the case with zero potential difference between the two layers and without strain.

Recent works by the group around Vafeek are dealing with the problem by a perturbative renormalization group approach within a continuum model for the vicinity of the band crossing points [Vaf10; VY10; TV11]. Here, the nematic state is favored for long-range Coulomb interaction and the AFM instability is leading for short-range interactions [TV11]. Similarly, Lemonik and coworkers found the nematic, AFM but also the QSH state to be realized in relevant regions of the parameter space [Lem10; LAF12]. These studies clearly indicate, that the precise shape of the interaction is crucial for the determination of the ground state. In this context, it is important to notice that the effective interaction parameters and their spatial dependence for the usual low-energy models of graphene and graphite have been calculated by ab initio techniques using constrained RPA (cRPA) that takes into account the screening due to bands further away from the Fermi level [Weh11].

In the present work, we use the fRG scheme detailed in chapter 2 for an unbiased investigation of the instabilities of the Bernal stacked bilayer honeycomb lattice. In contrast to previous renormalization group calculations [Vaf10; VY10; Lem10; TV11; CTV12; LAF12], we use density functional theory band-structure parameters, as well as cRPA interaction parameters, as inputs for our fRG treatment, and we integrate out the four p_z -derived bands fully from the band edges toward the Fermi energy. This way, we strongly reduce the variety of possibilities depending on the model parameters, and get closer to a realistic picture of bilayer graphene.

4.2 Model

We consider the model of interacting electrons on the honeycomb bilayer lattice. The model has previously been introduced in numerous works, e.g. [Cas09; MK12; Kot12].

The lattice of each layer consists of two sublattices, where each site of the sublattice A has three nearest neighbors in the sublattice B. In the physically more relevant configuration, the two layers are arranged in the A-B or so called Bernal stacking. This means that the sites of the two sublattices A_1 and A_2 are on top of each other, while B_2 (B_1) is in the center of the hexagon formed by the sites in the first (second) layer, according to figure 4.1. The layer distance is about 3.4 \AA [Cas09]. The three vectors pointing from each site of sublattice A_1 (B_2) to its nearest neighbors B_1 (A_2) are given by δ_i with $i \in \{1, 2, 3\}$

$$\delta_1 = \frac{\sqrt{3}a}{2}\vec{e}_x + \frac{a}{2}\vec{e}_y, \quad (4.1)$$

$$\delta_2 = -\frac{\sqrt{3}a}{2}\vec{e}_x + \frac{a}{2}\vec{e}_y, \quad (4.2)$$

$$\delta_3 = -a\vec{e}_y, \quad (4.3)$$

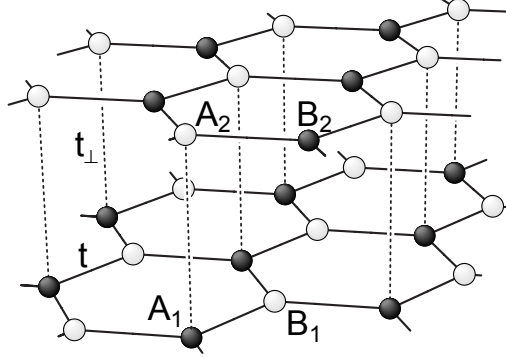


Figure 4.1: Sketch of the honeycomb bilayer in Bernal stacking with nearest neighbor intralayer hopping t between A and B sites of each layer and nearest neighbor interlayer hopping t_{\perp} between A_1 and A_2 sites. Cf., e.g., [Cas09; MK12].

where we adopted the convention of [Vaf10]. Here, $a = 1.4 \text{ \AA}$ [Cas09] is the distance between nearest neighbors in the same layer and $\vec{e}_{x/y}$ are unit vectors in x - and y -direction, respectively.

With this, we can write down the tight binding Hamiltonian, i.e. the non-interacting part, as

$$H^{\text{BL}} = H_0 + H_1 + H_3 + H_4 + H_5, \quad (4.4)$$

with

$$H_0 = -\gamma_0 \sum_{R, \delta_i, \sigma} \left(c_{B_1, \sigma}^{\dagger}(R + \delta_i) c_{A_1, \sigma}(R) + c_{B_2, \sigma}^{\dagger}(R - \delta_i) c_{A_2, \sigma}(R) + \text{h.c.} \right), \quad (4.5)$$

$$H_1 = \gamma_1 \sum_{R, \sigma} \left(c_{A_1, \sigma}^{\dagger}(R) c_{A_2, \sigma}(R) + \text{h.c.} \right), \quad (4.6)$$

$$H_3 = -\gamma_3 \sum_{R, \delta_i, \sigma} \left(c_{B_1, \sigma}^{\dagger}(R + \delta_1) c_{B_2, \sigma}(R + \delta_1 + \delta_i) + \text{h.c.} \right), \quad (4.7)$$

$$H_4 = \gamma_4 \sum_{R, \delta_i, \sigma} \left(c_{B_1, \sigma}^{\dagger}(R + \delta_i) c_{A_2, \sigma}(R) + c_{B_2, \sigma}^{\dagger}(R - \delta_i) c_{A_1, \sigma}(R) + \text{h.c.} \right), \quad (4.8)$$

$$H_5 = \Delta' \sum_{R, \sigma} \left(c_{A_1, \sigma}^{\dagger}(R) c_{A_1, \sigma}(R) + c_{A_2, \sigma}^{\dagger}(R) c_{A_2, \sigma}(R) \right). \quad (4.9)$$

Here, $c_{o, \sigma}^{\dagger}(r)$ and $c_{o, \sigma}(r)$ are creation and annihilation operator for an electron at site r with spin projection σ in orbital o . Here and in the rest of this chapter, R denotes the positions of the sites of the sublattice A_1 . γ_i are hopping parameters. Often, the first two hoppings are also denoted by $\gamma_0 = t$ and $\gamma_1 = t_{\perp}$. The first term, H_0 , describes the hopping between nearest neighbors. The second term, H_1 , describes vertical hopping between the A-sublattices. The third and fourth term, which are often referred to as trigonal warpings,

describe more remote hoppings between the layers, and the last term is a shift in chemical potential on the A sites. In the tight binding Hamiltonian (4.4 – 4.9) we included the most relevant terms according to Ref. [MK12], which contains an overview over different estimates for the hopping amplitudes.

We switch into momentum space by using the Fourier transform

$$\begin{aligned} c_{o,\sigma}(k) &= \frac{1}{\sqrt{\mathcal{N}}} \sum_r e^{ikr} c_{o,\sigma}(r) , \\ c_{o,\sigma}^\dagger(k) &= \frac{1}{\sqrt{\mathcal{N}}} \sum_r e^{-ikr} c_{o,\sigma}^\dagger(r) , \end{aligned} \quad (4.10)$$

where the sum over r includes all sites of the respective sublattice and \mathcal{N} is the number of unit cells. With this, we can write the tight-binding Hamiltonian (4.4) in momentum space as

$$H^{\text{BL}} = \sum_{k,\sigma} \Psi_\sigma^\dagger(k) \begin{pmatrix} \Delta' & \gamma_1 & \gamma_4 d_k & -\gamma_0 d_k^* \\ \gamma_1 & \Delta' & -\gamma_0 d_k & \gamma_4 d_k^* \\ \gamma_4 d_k^* & -\gamma_0 d_k^* & 0 & -\gamma_3 d_k \\ -\gamma_0 d_k & \gamma_4 d_k & -\gamma_3 d_k^* & 0 \end{pmatrix} \Psi_\sigma(k) , \quad (4.11)$$

with $\Psi_\sigma^\dagger(k) = (c_{A_1,\sigma}^\dagger(k), c_{A_2,\sigma}^\dagger(k), c_{B_2,\sigma}^\dagger(k), c_{B_1,\sigma}^\dagger(k))$ and $d_k = \sum_{\delta_i} e^{ik\delta_i}$.

When Δ' and the trigonal warping terms γ_3, γ_4 are set to zero, one can easily derive a simple expression for the eigenvalues of the Hamiltonian. In this case the four bands are given by

$$\epsilon_b(k) = \frac{1}{2} \left(\pm t_\perp \pm \sqrt{t_\perp^2 + 4t^2 |d_k|^2} \right) , \quad (4.12)$$

where we used the convention $\gamma_0 = t$ and $\gamma_1 = t_\perp$. Only the two bands, for which the two signs in equation (4.12) are opposite, touch the Fermi level. The band-structure exhibits two inequivalent QBCPs at the corners of the hexagonal Brillouin zone, which are denoted by K and K' . We recover the single layer case with two Dirac cones at K and K' , if t_\perp is set to zero.

The band-structure of the honeycomb bilayer is shown in figure 4.2. The right plot shows the vicinity of the K points in the presence of trigonal warping, chosen to the values $\gamma_0 = 3.16\text{eV}$, $\gamma_1 = 0.381\text{eV}$, $\gamma_3 = 0.38\text{eV}$, $\gamma_4 = 0.14\text{eV}$, $\Delta' = 0.022\text{eV}$, taken from [Kuz09]. Including γ_3 leads to a splitting of both QBCPs into 4 Dirac cones each, where the cones are still fixed to the Fermi level at half-filling. With the inclusion of γ_4 particle-hole symmetry is explicitly broken, and the three outer cones are shifted away from the Fermi level. The change in the topology of the dispersion relation due to trigonal warping terms sets in at an energy scale of the order of 1 meV [MK12]. A more detailed discussion of the model for bilayer graphene, its dispersion relation and the individual hopping terms can for instance be found in [MK12].

In the following, we set Δ' , γ_3 , and γ_4 to zero for simplicity. This is motivated

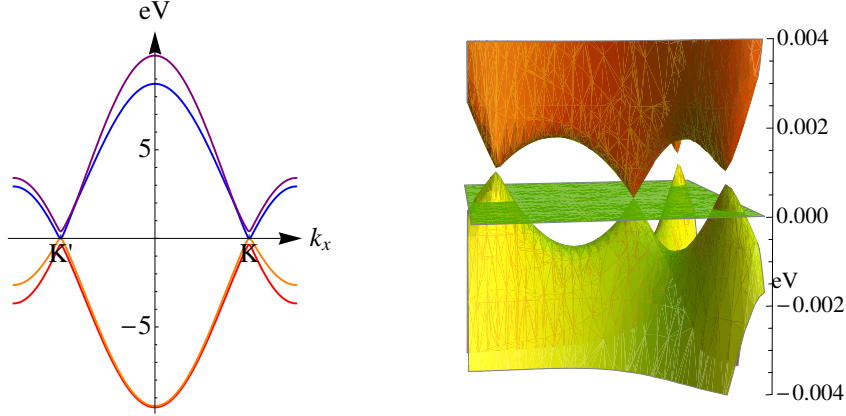


Figure 4.2: Left: Two-dimensional plot of the dispersion relation of the four bands in the honeycomb bilayer. The outer bands drawn in red and purple do not touch the Fermi level at finite t_{\perp} . Right: Dispersion relation of the honeycomb bilayer in the close vicinity to the K point with the terms γ_3 , γ_4 and Δ' included, according to [Kuz09]. The splitting of the QBCP cannot be seen in the left plot, as the corresponding energy scale is too small. Cf. figures 3, 4 in [MK12].

by the fact, that the critical scales, we find with the fRG approach, are larger than this scale. Moreover, gap sizes inferred from experiment are larger than 1 meV, albeit still of the same order of magnitude [Vel12a; Fre12; Bao12; Vel12b].

We will consider an on-site interaction U , a nearest-neighbor intralayer interaction V_1 and a next-nearest-neighbor intralayer interaction V_2 . The on-site repulsion is given by

$$H_U = U \sum_{R,o} n_{o,\uparrow}(R + \delta_{o,1}) n_{o,\downarrow}(R + \delta_{o,1}) , \quad (4.13)$$

with $n_{o,\sigma}(r) = c_{o,\sigma}^\dagger(r) c_{o,\sigma}(r)$. Here, we introduced

$$\delta_{o,i} = \begin{cases} 0, & \text{if } o \in \{A_1, A_2\} \\ (-1)^{j-1} \delta_i, & \text{if } o = B_j \end{cases} \quad (4.14)$$

for a more compact notation. The nearest-neighbor and next-nearest-neighbor interaction read

$$H_{V_1} = V_1 \sum_{\substack{R,i,j \in \{1,2\}, \\ \sigma, \sigma'}} n_{A_j, \sigma}(R) n_{B_j, \sigma'}(R + \delta_{B_j, i}) , \quad (4.15)$$

$$H_{V_2} = \frac{V_2}{2} \sum_{\substack{R, \sigma, \\ \Delta_i, \sigma, \sigma'}} n_{o, \sigma}(R + \delta_{o,1}) n_{o, \sigma'}(R + \delta_{o,1} + \Delta_i) , \quad (4.16)$$

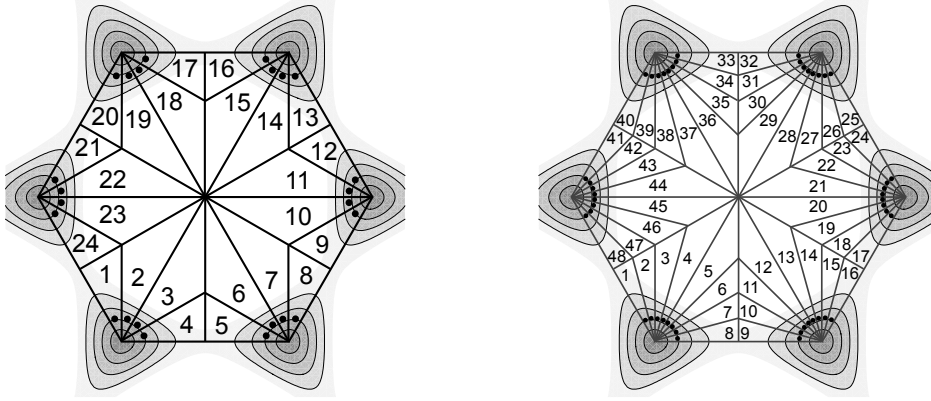


Figure 4.3: Patching scheme of the Brillouin zone in the fRG. The black dots denote the momentum vectors, at which the coupling function is evaluated. Shown are the two discretizations with $N = 24$ and $N = 48$ patches. Both resolutions yield qualitatively the same results.

where

$$\begin{aligned} \Delta_1 &= \delta_1 - \delta_2, & \Delta_2 &= \delta_3 - \delta_2, & \Delta_3 &= \delta_3 - \delta_1, \\ \Delta_4 &= \delta_2 - \delta_1, & \Delta_5 &= \delta_2 - \delta_3, & \Delta_6 &= \delta_1 - \delta_3 \end{aligned} \quad (4.17)$$

are the vectors connecting second nearest neighbors. Below, we will also study the stability of our results with respect to the inclusion of a third-nearest-neighbor intralayer interaction. In section 4.6, we will additionally include long-ranged interactions, i.e. a Coulomb tail, of the electron-electron interaction.

4.3 Functional Renormalization Group Treatment

For the fRG treatment, we use a similar approach as in the study of the system with a single QBCP in the preceding chapter (see section 3.3), to study the leading instabilities of interacting electrons on the honeycomb bilayer. Again, we neglect the three-particle vertex, self-energy contributions, and the frequency dependence of the vertex, by setting all external frequencies in the fRG equations to zero. As before, we use a patching scheme to make the numerical integration in momentum space feasible. The patches are chosen, as shown in figure 4.3. The vertices are computed at momenta set on two rings around the QBCPs at K and K' . As in chapter 3, we choose the patching points away from the QBCP to account for the winding of the Bloch functions. We also include the bands, which do not touch the Fermi surface in the fRG treatment. The patches are set on the same positions in all four bands. Again, we have checked that changing the radius of the ring, on which the patching points are located does not change the qualitative results. We mostly employ a patching

with $N = 24$ patches per band (left panel of figure 4.3). In some cases, we will increase the accuracy by doubling the number of patches (right panel of figure 4.3). However, we did not encounter any major differences in the results of the flows with different discretization.

As all bands are fully taken into account within our approach, we can simply transform back into the orbital basis, to obtain easily interpretable data. As opposed to the situation in chapter 3, here it is not clear, which choice for the eigenvectors in the orbital-to-band transformation is best suited. On the other hand, we tried different choices and checked that critical scales and the leading instabilities are independent of this.

We note, that it needs some severe improvements to the patching scheme, if one wants to take into account trigonal warpings. Here, the QBCP splits into 4 Dirac points (see section 4.2), and to take into account the winding around each Dirac cone, one has to introduce additional patches at momenta inside the splitting of the QBCP. This drastically increases the needed numerical effort. We, therefore, restrict the analysis to the simpler case with vanishing trigonal warping terms. We will see that our estimates of the critical scale are much larger, than the energy window, in which trigonal warpings change the topology of the dispersion. Therefore, the inclusion of these terms should not drastically change our results. However, the experimental estimates for gaps of symmetry broken phases are of the order of a few meV, which is comparable to the scale of the splitting of the QBCP, as discussed above. Thus, the inclusion of trigonal warping terms in future works might be worthwhile.

Typically the vertices will diverge at a critical scale, due to the neglect of self-energy, which would regularize the flow. We stop the fRG flow, when the vertices exceed a certain value larger than the bandwidth. We estimate Λ_c by an extrapolation of $1/V_{\max}$ over Λ , where V_{\max} is the maximum value of the coupling function. The scale, at which the extrapolated value of $1/V_{\max}$ becomes zero gives Λ_c . The analysis on which class of coupling constants diverge, enables us to obtain tentative ground state diagrams for bilayer graphene.

As opposed to other works using different renormalization group approaches to bilayer graphene [Vaf10; VY10; Lem10; TV11; CTV12; LAF12], we dispense with the restriction of the original model to the modes close to the QBCP. Our calculations can, thus, be directly based on ab initio parameters, which enables us to easily identify the experimentally relevant parameter region and to give predictions on the energy scales of the ordering phenomena. Moreover, the full information of all four bands is kept, which enables us, for instance, to detect the QSH state proposed by Varma et al. [ZAV12] as opposed to the 'usual' QSH state. These two states differ from each other, in the sign of the QSH order parameter in the two layers, i.e. in the direction of the net current. In our approach this manifests in different relative signs in the couplings with legs in different orbitals. This feature cannot be detected, if the available information is restricted to only two bands. We will discuss this issue below in section 4.4.

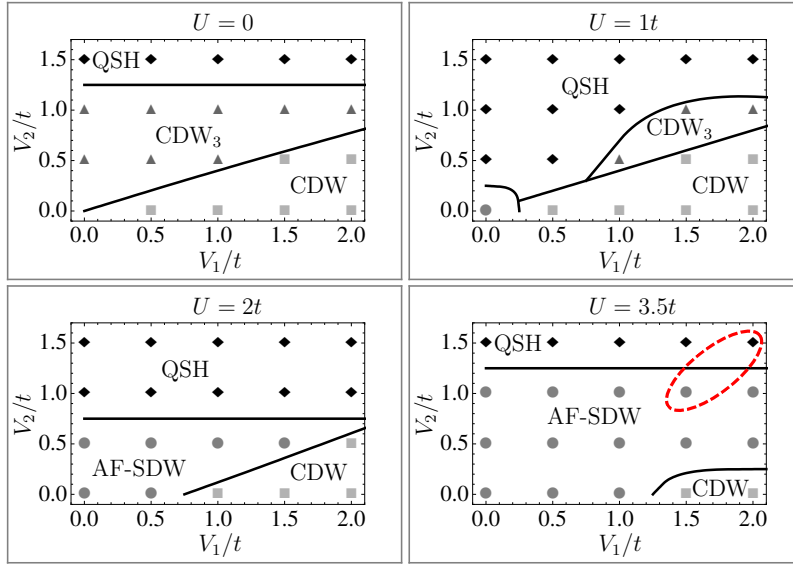


Figure 4.4: Tentative fRG phase diagrams for $U/t = 0, 1, 2, 3.5$ and $t_{\perp} = 0.1t$. The black lines are guides for the eye and separate the different regimes. The area encircled by the dashed line shows the region of the cRPA parameters of Ref. [Weh11].

4.4 Phase Diagram of the Honeycomb Bilayer

Here, we present the fRG results at zero temperature for interlayer hopping $t_{\perp} = 0.1t$ as estimate for values in literature, e.g. for graphite [Zha08; Kuz09] or for few-layer graphene [Oht07]. We also analyzed larger $t_{\perp} < t$, without major qualitative differences, except for the values of the critical scales. We consider the charge-neutrality point, if not stated otherwise.

The nearest-neighbor hopping $t \approx 3\text{eV}$ sets the energy unit. We then study the parameter space spanned by U, V_1 and V_2 up to the cRPA parameters found in Ref. [Weh11]. By identifying the leading tendencies, i.e. the strongest class of divergent couplings, we encounter rich tentative phase diagrams shown in figure 4.4. The drawn boundaries are guides for the eye. Typically, the flows change continuously from one regime to the other without drastic features in Λ_c . Hence, while without including self-energy effects a possible suppression of the critical scales due to quasi-particle degradation is not captured, we expect that these transitions are of first order. We now discuss the various ordering tendencies found for given parameters and how they are revealed in the fRG flow.

The procedure is analogous to the one described in detail in 3.4. The diverging couplings of the interaction vertex near Λ_c are extracted, to obtain an effective low-energy Hamiltonian. The corresponding order parameter can be inferred from a mean field decoupling.

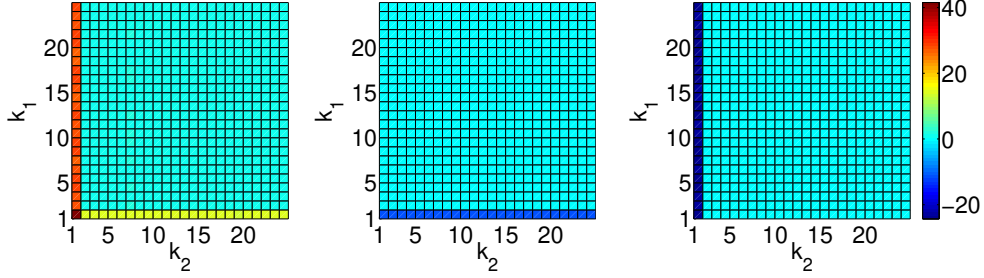


Figure 4.5: Effective interaction near the critical scale in the AFM SDW phase in units of t . The patch k_1 (k_2) of the first (second) ingoing leg is plotted on the y (x) axis, with the discretization shown in figure 4.3. $k_3 = 1$ is kept fixed. In our convention, the first and the third leg have the same spin. The first plot shows the vertices with the orbitals $o_1 = o_2 = o_3 = o_4 = B_2$, the second plot shows the combination $o_1 = o_3 = B_2$, $o_2 = o_4 = B_1$, and the third plot shows $o_1 = o_4 = B_2$, $o_2 = o_3 = B_1$.

In the fRG data, the flow towards the AFM SDW is seen as a leading divergence of interaction components with zero momentum transfer in the spin channel. It features an attractive sign for intra-sublattice scattering and a repulsive sign for inter-sublattice processes, in complete correspondence to the single layer [Hon08]. A snapshot of the interaction vertex is shown in figure 4.5. The interlayer sign structure can be read from the fRG data as well. In detail, the leading part of effective interaction in this case reads

$$H_{\text{AFM}} = -\frac{1}{\mathcal{N}} \sum_{o,o'} V_{oo'} \varepsilon_o \varepsilon_{o'} \vec{S}_o \vec{S}_{o'} , \quad (4.18)$$

with

$$\vec{S}_o = \frac{1}{2} \sum_{k,\sigma,\sigma'} \vec{\tau}_{\sigma\sigma'} c_{o,\sigma}^\dagger(k) c_{o,\sigma'}(k) , \quad (4.19)$$

and $V_{oo'} > 0$. The ε_o s depend on the orbital, as $\varepsilon_o = +1$ for $o \in \{A_1, B_2\}$ and $\varepsilon_o = -1$ for $o \in \{A_2, B_1\}$. The effective interaction has become infinitely-ranged due to the sharpness in momentum space. A mean-field decoupling of H_{AFM} results in an AFM spin alignment in each layer, where a net spin (e.g. 'up') moment is located on the A_1 - and B_2 -sublattices, and an opposite net spin ('down') moment on the B_1 - and A_2 -sublattices. In absence of spin-orbit interactions, the spin quantization axis is not fixed. A closer look at the fRG data shows that the intralayer components $V_{oo'}$ on the B sublattices grow faster toward the instability than the couplings on the A-sublattices, pointing to a larger spin moment on the B sublattice, in agreement with QMC simulations [Lan12] for the same system, with pure on-site interactions, see section 4.5.

For large nearest-neighbor interaction, we encounter diverging interactions in

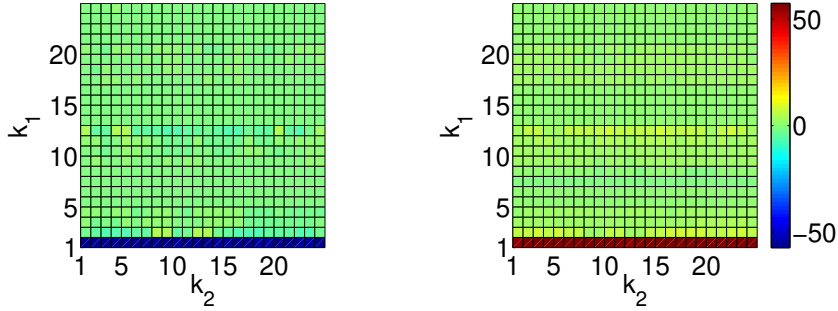


Figure 4.6: Effective interaction near the critical scale in the CDW phase in units of t . The patch k_1 (k_2) of the first (second) ingoing leg is plotted on the y (x) axis, with the discretization shown in figure 4.3. $k_3 = 1$ is kept fixed. In our convention, the first and the third leg have the same spin. The left plot shows the vertices with the orbitals $o_1 = o_2 = o_3 = o_4 = B_2$, the right plot shows the combination $o_1 = o_3 = B_2$, $o_2 = o_4 = A_2$.

the density channel, again with zero momentum transfer, with opposite signs for the intra- and interorbital interactions, see figure 4.6. In detail, we observe the effective interaction

$$H_{\text{CDW}} = -\frac{1}{\mathcal{N}} \sum_{o,o'} V_{oo'} \varepsilon_o \varepsilon_{o'} n_o n_{o'} , \quad (4.20)$$

with

$$n_o = \sum_{k,\sigma} c_{o,\sigma}^\dagger(k) c_{o,\sigma}(k) , \quad (4.21)$$

and $V_{oo'} > 0$. Within a layer, this results in an infinitely-ranged attraction for sites on the same sublattice and repulsion for sites on different sublattices. The sign-structure between the layers favors an enhanced occupancy of the A_1 and B_2 sublattices and a reduced occupancy on the B_1 and A_2 sublattices or vice versa. The electronic spectrum becomes gapped by this ordering.

The QSH phase breaks spin-rotational symmetry, whereas time reversal symmetry remains conserved [KM05a; QZ11]. In the fRG flow, spin interactions with zero wavevector transfer diverge, with an additional sign structure that alternates between K and K' points, and between the sublattices. A snapshot of the vertices near the divergence is shown in figure 4.7. The effective interaction reads

$$H_{\text{QSH}} = -\frac{1}{\mathcal{N}} \sum_{o,o'} V_{oo'} \varepsilon_o \varepsilon_{o'} \vec{S}_o^f \vec{S}_{o'}^f , \quad (4.22)$$

with

$$\vec{S}_o^f = \frac{1}{2} \sum_{k,\sigma,\sigma'} f_k \vec{\tau}_{\sigma\sigma'} c_{o,\sigma}^\dagger(k) c_{o,\sigma'}(k) , \quad (4.23)$$

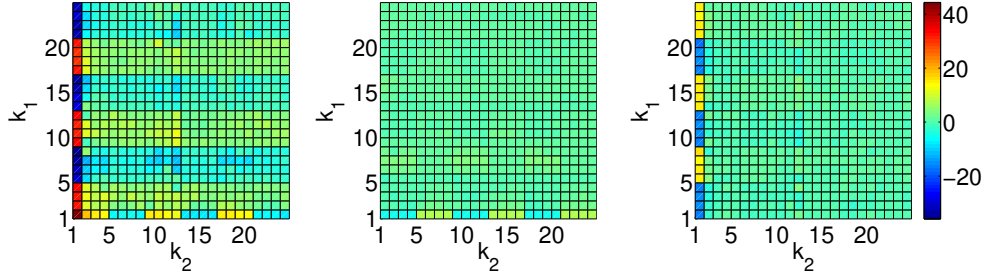


Figure 4.7: Effective interaction near the critical scale in the QSH phase in units of t . The patch k_1 (k_2) of the first (second) ingoing leg is plotted on the y (x) axis, with the discretization shown in figure 4.3. $k_3 = 1$ is kept fixed. In our convention, the first and the third leg have the same spin. The first plot shows the vertices with the orbitals $o_1 = o_2 = o_3 = o_4 = B_2$, the second plot shows the combination $o_1 = o_3 = B_2$, $o_2 = o_4 = A_2$, and the third plot shows $o_1 = o_4 = B_2$, $o_2 = o_3 = A_2$.

including a f -wave form factor $f_k = \sin(\sqrt{3}ak_x) - 2\sin(\frac{\sqrt{3}ak_x}{2})\cos(\frac{3ak_y}{2})$. Again $V_{oo'} > 0$ is positive for all indices. In a mean-field treatment of this effective interaction, a purely imaginary Kane-Mele [KM05a] order parameter in each layer is induced. The order parameter can be written as

$$\vec{\Phi}_{\text{KM}} = \sum_{\substack{\Delta_i, \sigma \\ \sigma, \sigma'}} \langle \varepsilon_o (-1)^i \vec{\tau}_{\sigma\sigma'} [c_{o,\sigma}^\dagger(R + \delta_{o,1}) c_{o,\sigma'}(R + \delta_{o,1} + \Delta_i)] \rangle, \quad (4.24)$$

with $\delta_{o,i} = 0$ for $o \in \{A_1, A_2\}$ and $\delta_{o,i} = (-1)^{j-1} \delta_i$ for $o = B_j$ as in section 4.2 and Δ_i , as defined in equation (4.17), connecting next-nearest neighbors. The sign differs for the A and B sublattice of each layer. That means that the flux in each sublattice has the same orientation for each spin projection. Moreover, the chirality of the state comes out the same in the two layers for the same spin. All flux currents are oriented, counterclockwise for one and clockwise for the other spin projection. Consequently, there are two edge modes with the same propagation direction per spin. Hence, the edge states are not topologically protected, as we have two copies of the Kane-Mele order parameter [QZ11]. We will nevertheless refer to this state as QSH state.

Interestingly, we found another instability for smaller U and $V_2/t \lesssim 1.0$. It is a three-sublattice CDW instability (CDW₃). Here a site-centered CDW tendency with a finite momentum transfer $Q = K - K' = K'$ grows during the fRG flow. The wavevector dependence of the interaction vertex near Λ_c for this CDW₃ instability is shown in figure 4.8. The sharp features belong to wavevector transfer $\pm Q$. Only processes with initial k_1 and k_2 near different band crossing points grow strongly, because only then the final states, after scattering by $\pm Q$, lie near the BCPs as well. This causes the interruption of

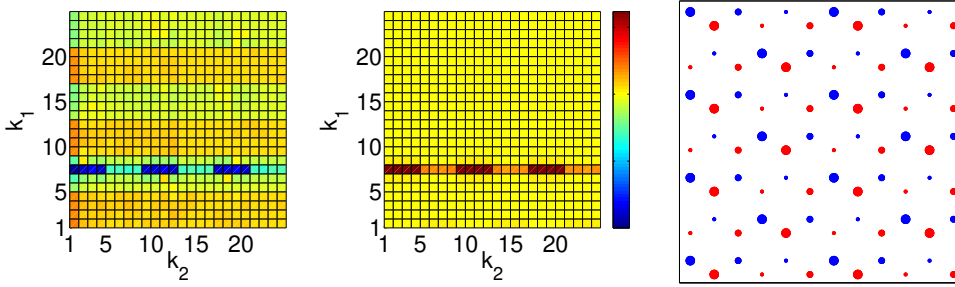


Figure 4.8: CDW₃ instability. Left and middle plot: Effective interaction near the critical scale in units of t for $U = 0, V_1 = 0.5t, V_2 = 0.5t$ and $t_\perp = 0.1t$. The patch k_1 (k_2) of the first (second) ingoing leg is plotted on the y (x) axis, with the discretization shown in figure 4.3. $k_3 = 1$ is kept fixed. In our convention, the first and the third leg have the same spin. The left plot shows the vertices with the orbitals $o_1 = o_2 = o_3 = o_4 = B_2$, the middle plot shows the combination $o_1 = o_3 = B_2, o_2 = o_4 = B_1$. Right: Qualitative charge distribution in the CDW₃ mean-field state for $\alpha = 1/6$ and equal $|\Delta_o^{\text{CDW}_3}|$ s in one layer. The size of the symbols indicates the charge density, the three sizes in one (original) sublattice average to 1.

the horizontal features in figure 4.8. The corresponding effective interaction given by these leading terms near the divergence becomes

$$H_{\text{CDW}_3} = -\frac{1}{\mathcal{N}} \sum_{o,o'} V_{oo'} \varepsilon_o \varepsilon_{o'} (n_o(Q) n_{o'}(-Q) + n_o(-Q) n_{o'}(Q)), \quad (4.25)$$

with

$$n_o(Q) = \sum_{k,\sigma} c_{o,\sigma}^\dagger(k+Q) c_{o,\sigma}(k), \quad (4.26)$$

and $V_{oo'} > 0$. In this equation it is understood that the wavevectors k range in the vicinity of the K and K' points, as only there the interactions grow large. In a variational treatment, (4.25) is minimized by complex expectation values

$$\langle n_o(Q) \rangle = \varepsilon_o |\Delta_o^{\text{CDW}_3}| e^{i\varphi}. \quad (4.27)$$

These break the translational symmetry by density modulations $\propto \cos(Qr + \varphi)$. Based on the fRG data for $V_{oo'}$, the $|\Delta_o^{\text{CDW}_3}|$ should be of comparable magnitude. Each original sublattice o is broken up into three sublattices (see right plot in figure 4.8). Changing φ reorganizes the charges within the three new sublattices while keeping the average constant. The discrete rotational symmetry is broken completely for general φ . Hence, this state should be observable directly in scanning tunneling experiments. Depending on the phase φ , the quadratic mean-field Hamiltonian for a single layer either exhibits a

gapless spectrum with Dirac points shifted away from the K , K' points or a fully gapped state. Which case represents the mean-field ground state as function of the interaction parameters has yet to be determined variationally.

Let us now discuss the relation of the fRG data on the honeycomb bilayer to bilayer graphene. In [Weh11] the interaction parameters for single layer graphene and graphite were estimated by ab initio methods. We expect bilayer graphene to interpolate between these cases. The area of these ab initio interaction parameters is shown as a dashed line in the bottom right plot in figure 4.4. In the fRG for this parameter range, SDW and QSH instabilities compete. Which one is leading depends, however, on the precise values of the interaction and also the hopping parameters, so that we refrain from giving a definite prediction. We have also checked that a third-nearest-neighbor repulsion $V_3 < t$ does not change the nature of the ground state for these parameters. As both states have a non-zero single particle gap, they are compatible with the experimental spectrum of [Vel12a]. A distinction might be made from testing for time-reversal symmetry breaking, which only occurs for the SDW state. As the QSH state corresponds to two copies of the Kane-Mele single layer state, gapless edge state transport might be spoiled by impurities as the edge states are not protected by topology [QZ11]. Further, for the f -wave order parameter of the QSH, impurities will be detrimental, and the experimental gap is only seen in ultraclean samples [Vel12a].

On the other hand, along with the experiments in [Vel12a] and [Bao12], our findings are not compatible with the experimental spectrum reconstruction in [May11] where a nematic phase is proposed as the ground state. In fact, the existence of a nematic state is not reflected in the parameter range that we covered in our analysis in contrast to other renormalization group works [Vaf10; Lem10; LAF12]. One difference is, that we implemented a lattice model for the complete bandwidth including four bands and not a low-energy continuum model. Furthermore, so far, we only considered short-ranged ab initio parameters, and did not include a long-ranged Coulomb interaction, which favors the emergence of nematic order, according to [Vaf10; VY10; TV11]. In order to check, whether the absence of the nematic instability in our approach is due to the restriction to short-range interactions, we consider longer ranged interactions in section 4.6.

We want to shortly discuss the proposal of Zhu, Vivek and Varma [ZAV12]. They propose a state, which we, hereafter, refer to as ZVV-state, where the flux orientation is opposite in both layers as opposed to the QSH state we found in our fRG analysis, where the flux has the same orientation in all four sublattices for a given spin projection. In more detail they performed a mean field analysis on the honeycomb bilayer with a second nearest neighbor interaction. Their calculation suggests, that there is a parameter window, in which the ZVV-state has a lower ground state energy than the QSH state. We carefully analyzed the fRG data and confirmed that the QSH instability is leading over the ZVV-state,

for any reasonable choice of interaction parameters.

4.5 Critical Scale of the Instabilities

In this section, we will compare the critical scales obtained from fRG calculations, with gap sizes from experiment and with QMC data obtained for the honeycomb bilayer with on-site interaction only.

The instability scales deduced for the parameters extracted from ab initio calculations [Weh11] are huge (up to $\approx t$), due to the perfect nesting between the two bands forming the QBCPs. We cannot guarantee that our method still works quantitatively in this regime. Most likely, the inclusion of self-energy corrections and frequency dependence of the interactions will reduce the fRG scales. However, it is clear that the experimental energy gaps $\approx 2 \text{ meV} \approx 10^{-3}t$ [Vel12a] are several orders of magnitude smaller than the gap scales one gets, theoretically, in this simple modeling, using a method that should be expected to be more realistic than mean-field theory or simpler perturbative arguments.

The single layer system for pure on-site interactions offers a possibility to compare the energy scales in the fRG with numerically exact QMC data. At $U_{c,\text{QMC}} \approx 4.3t$, where, according to QMC, the AFM order sets in above a narrow spin-liquid regime [Men10], the single particle gap is $\approx 0.15t$. The fRG approach gives $\Lambda_c = 0.85t$ at $U = 4.3t$. Hence, the overestimate near the opening of the gap at $U_{c,\text{QMC}}$ in QMC is about a factor $\approx 5 - 6$, which is reasonable for an order of magnitude estimation. However, the critical interaction strength found in the fRG approach is only $U_c \approx 2.8t$, which is considerably smaller than the value $U_{c,\text{QMC}} \approx 4.3t$ obtained from QMC.

To gain additional information about the reliability of the estimation of the critical scale in the bilayer case, we compare our critical scales to QMC and mean-field data, which are published in [Lan12]. Here, we restrict to an on-site interaction U , as additional interactions are hard to handle in the QMC approach, due to the sign problem. Also, we choose $t_{\perp} = t$, as the QMC and the mean field calculations are done on finite systems, and therefore a sufficiently large t_{\perp} is needed, in order to resolve the quadratic behavior of the dispersion relation in the vicinity of the band crossing points. All three approaches find accordingly the emergence of the spin order parameter, that is a finite expectation value of the operator given in equation (4.19), with the tendency of a smaller net magnetization on the A sublattice.

In figure 4.9, we compare the estimated gaps from QMC and mean-field calculations to the critical scale of the fRG method. The fRG data in 4.9 are obtained within the improved patching with $N = 48$ patches per band, as shown in the right panel of figure 4.3. Again, we observe that the fRG overestimates the critical energy scale to a factor smaller than 10. Note, however, that due to the restriction of the QMC method, we are not able to obtain a comparison at a smaller, more realistic value of t_{\perp} .

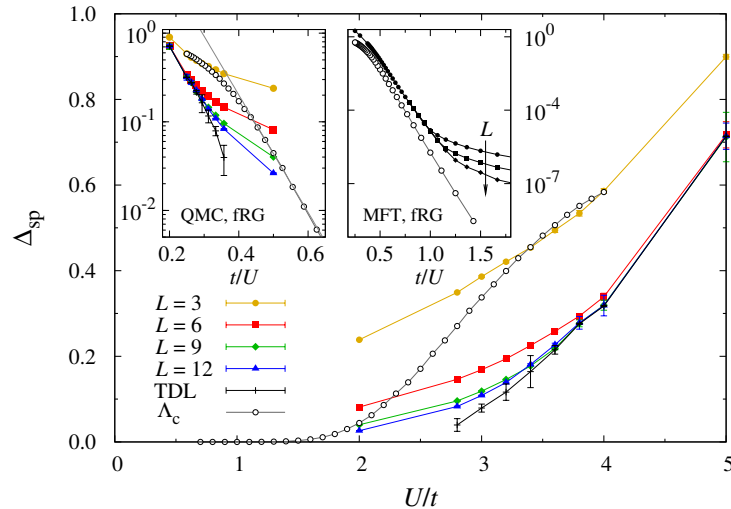


Figure 4.9: Single particle gap from QMC for different system sizes and the finite size extrapolation to the thermodynamic limit using a polynomial fit function, along with the fRG critical scale Λ_c , obtained with the improved patching with $N = 48$ patches per band, as a function of the local Coulomb repulsion U/t in the AFM regime. The inset on the left shows the same data vs. t/U in a semilog scale, exhibiting an exponential onset of the gap in the large t/U range. The inset on the right shows the fRG data along with mean field results for different system sizes.

The insets in figure 4.9 nicely show the exponential dependence of the critical scale and confirms that no critical interaction strength is needed to establish an instability. Owing to the finite density of states at the Fermi level, this is expected, e.g. from RPA. For details, see appendix B. The fRG nicely complements the data obtained with the QMC and mean-field approach, as these methods suffer from finite size effects and thus cannot reproduce this trend for small values of U .

We also investigated the impact of non-vanishing chemical potentials ($\mu \neq 0$) to mimic the effect of impurities or small dopings on the ground state, with focus on the cRPA interaction parameters and $t_{\perp} = 0.1t$. In the range between $\mu \in (0, 0.5t]$, the critical scale Λ_c only changes mildly and the ground state remains unchanged, as shown in the left panel figure 4.10.

Of course, in the experiment, unintentional doping and potential variations will lead to a reduction of the energy scales. But, as one can see from the doping dependence just described, even a combination of factors like doping, disorder, trigonal warping, additional reductions of the interaction parameters etc., does probably not suffice to reduce the scales down to values compatible with the experiment.

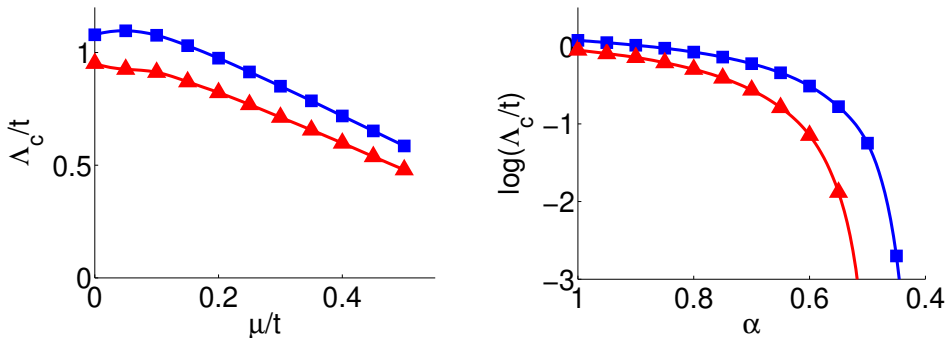


Figure 4.10: Left: FRG critical scale Λ_c vs. chemical potential μ for graphene (blue squares) and graphite (red triangles) cRPA interaction parameters [Weh11]. Right: Critical scale Λ_c as function of a rescaling parameter α for graphene (blue squares) and graphite (red triangles) cRPA interaction parameters.

We have seen that the fRG cannot reproduce the experimentally found energy scales with the interaction parameters extracted from DFT+cRPA, probably due to shortcomings of our approximations, e.g. neglect of self-energy effects. Thus, it is an interesting question to ask, whether the leading ordering tendencies found in the preceding section are dependent on the critical scale. Therefore, we introduce a global rescaling parameter α for the interaction terms, i.e. $U \rightarrow \alpha U$, $V_1 \rightarrow \alpha V_1$, $V_2 \rightarrow \alpha V_2$. We find that α does not change the nature of the ground state, i.e. for the graphene parameters we observed a QSH instability for all α and for the graphite parameters the SDW instability. Λ_c decreases by two orders of magnitude as $\alpha \lesssim 0.5$, as shown in the right plot of figure 4.10. That means, to recover the energy scales obtained by the experiments, the interaction has to be reduced to about half of its estimated value, if no other possible corrections, are taken into account. This finding can be related to the underestimation of the critical interaction strength in the single layer compared to QMC. We will discuss this issue again in section 5.5. Here, we will see that the overestimation of the critical scale, compared to the experiments is consistently reproduced in honeycomb models with different numbers of layers and stacking orders. If the interaction strength is chosen such that the single layer remains in the semi-metallic phase, as found in the experiments, we obtain critical scales, for honeycomb bi- and trilayer, which compare well with experimentally found gaps.

4.6 Inclusion of Long-Ranged Interaction

A crucial difference to other renormalization group calculations on bilayer graphene is the inclusion of Coulomb-interaction with a long-range tail. We want

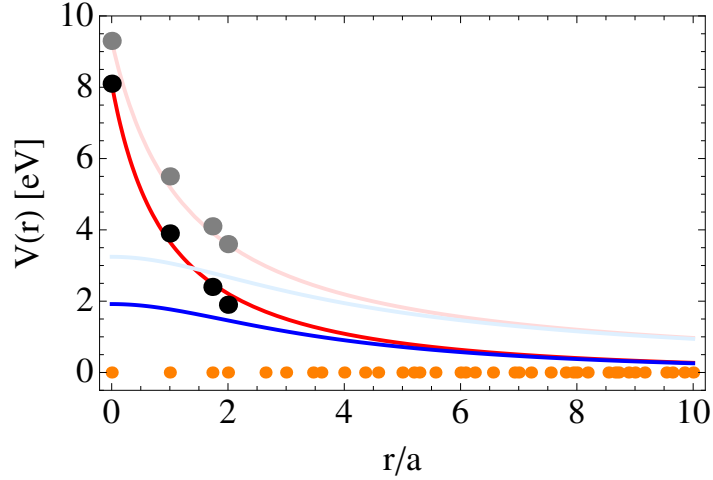


Figure 4.11: Fitting potential with the three parameters U, ϵ, ξ . The red (blue) lines describe the interaction strength for sites in the same (different) layer for graphene (light) and graphite (solid). The dots show the corresponding values for the interactions of the three nearest neighbors as found by Wehling for graphene (gray) and graphite (black). The orange dots indicate the positions of next neighbors. Parameters: $U = 9.3\text{eV}$, $\epsilon = 1.2$, $\xi = \infty$ (graphene); $U = 8.1\text{eV}$, $\epsilon = 1$, $\xi = 10$ (graphite).

to consider this in our analysis, to check whether this is the reason why we cannot detect a nematic instability in the analysis described in section 4.4.

We choose the following screened Coulomb potential for a parametrization of the long-range interaction, as an ad hoc ansatz

$$V(r) = \frac{\epsilon U}{\sqrt{l(a_{\perp}/a)^2 + (r/a)^2} + \epsilon} \exp\left(-\frac{\sqrt{l(a_{\perp}/a)^2 + (r/a)^2}}{\xi}\right), \quad (4.28)$$

where r is the two-dimensional distance of two sites, $a_{\perp} \approx 3.4 \text{ \AA}$ [Cas09] the distance between the layers, and $a \approx 1.4 \text{ \AA}$ [Cas09] is the distance between nearest neighbors. For $\xi \rightarrow \infty$ the potential is $\sim 1/r$. The index l indicates, whether the two interacting sites are located in the same ($l = 0$) or in a different layer ($l = 1$). At $r = 0$, we find the on-site value U , if the neighbors are located in the same layer. We use DFT data [Weh11] to fix the fitting parameters U , ϵ and ξ in equation (4.28). In figure 4.11, we show the fitting function, which reproduces the interaction parameters given in [Weh11]. We use this fitting function to extract interaction parameters for the more remote interactions. We include interactions between neighbors, with a distance up to 10 times the carbon bond-length. This approach includes only a finite number of remote interactions, and thus does not amount for an inclusion of the complete long-range tail. However, we do not expect that contributions to the interaction, from very remote neighbors, are physically relevant.

Within this setup, fRG flows were performed, with different values for the fitting parameters in equation (4.28). Only preliminary results were obtained before the completion of this thesis.

For shorter ranged interaction, we recover the AFM SDW state detailed in section 4.4 as expected. For a longer ranged Coulomb potential, the interaction vertex at the initial scale are already comparable in magnitude to the bandwidth, if the fitting procedure with the DFT data is employed (figure 4.11). Therefore, the approximations in the fRG method are no longer justified. If the fRG flow is performed with long-range Coulomb interaction, with smaller magnitude, than suggested by the fitting procedure, we either observe again the AFM SDW instability or no diverging interactions, i.e. the critical scale is below the value, which is numerically accessible. In particular, the nematic instability has not been detected within this fRG scheme, as opposed to related works [Vaf10; VY10; Lem10; TV11; LAF12]. Further research is needed, to investigate the parameter space of the Coulomb interaction more carefully and to determine the reason, why, within our approach, the nematic instability is not as prominent as one would expect from the results of perturbative renormalization group calculations in the low-energy continuum model [Vaf10; VY10; Lem10; TV11; LAF12].

4.7 Conclusion

We have presented a fRG study of interaction driven instabilities in the honeycomb bilayer model. Besides a novel CDW_3 state, we found that using ab initio estimates for the band-structure and non-local interaction parameters for bilayer graphene leads to a narrow competition of QSH and AFM SDW instabilities, making them the two main candidates for the experimental search. Details might decide what the actual ground state is.

We observed very high energy scales for the breakdown of the gapless state, when employing the interaction parameters extracted from cRPA. This discrepancy is presumably caused by the approximations of the fRG method, e.g. neglect of self-energy feedback. A rescaling of the interaction parameters to about half of their original values is needed to reproduce the experimentally found gap sizes. In section 5.5, we will see that with this rescaling procedure we are able to consistently reproduce the experimental trends in single, bi- and trilayer graphene.

The leading instability for the interaction parameters extracted from DFT is fairly unaffected by the absolute strength of the interaction and is mainly dependent on the ratio of the different interaction terms. So, we conclude that the prediction, that either AFM SDW or QSH state is favored in bilayer graphene, is still relevant for the experimental situation, despite of the discrepancy of the energy scale in theory and experiment.

Chapter 5

Interacting Electrons on Trilayer Honeycomb Lattices

Few-layer graphene systems come in various stacking orders. Considering tight-binding models for electrons on stacked honeycomb layers, this gives rise to a variety of low-energy band-structures near the charge neutrality point. Depending on the stacking order these band-structures enhance or reduce the role of electron-electron interactions. In this chapter, we investigate the instabilities of interacting electrons on honeycomb multilayers with a focus on trilayer with ABA and ABC stackings. We find different types of competing instabilities and identify the leading ordering tendencies in the different regions of the phase diagram, for a range of local and non-local short-ranged interactions. The dominant instabilities turn out to be toward an AFM SDW, a CDW and QSH order. Ab initio values for the interaction parameters put the systems at the border between SDW and QSH regimes. Furthermore, we discuss the energy scales for the interaction-induced gaps in this model study and put them into context with the scales for single layer and Bernal-stacked bilayer honeycomb lattices. This yields a comprehensive picture of the possible interaction-induced ground states of few-layer graphene.

This chapter has previously been published in [Sch12].

Contents

5.1	Introduction	65
5.2	Models	66
5.3	ABA and ABC Trilayer Hubbard Model	71
5.4	ABC trilayer: Instabilities and Phase Diagram with Non-Local Interactions	75
5.5	Energy Scales of the Ordering Phenomena	79
5.6	Conclusion	82

5.1 Introduction

After having considered the honeycomb bilayer in the preceding chapter, we mainly focus on trilayer in the following. Experiments on graphene systems

with three layers [Bao10; Tay11; Zha11b; Kum11; Jha11; Lui11; Kho12; HNE12] aimed to clarify the role of many-body interactions [NK10; Bao11]. For bilayer graphene, the experimental studies agree on the correlated nature of the ground state, but disagree on the symmetries of the underlying order, a topic that is a matter of current debate. At temperatures below 5K, transport experiments found gap openings of about 2-3 meV [Vel12a; Bao12; Vel12b], for further details, see also section 4.1. For trilayer graphene, the stacking order is crucial for the electronic properties [KM09; Zha10b; APP10; GLS11; YRK11; KM11; BCR12; ZTM12; JM12; Xu12]. In [Bao11], it was found that neutral trilayer graphene with ABC stacking shows many-body correlations with a pronounced gap of ≈ 6 meV, while graphene trilayers with ABA stacking do not show a gap. In view of this experimental situation, a better theoretical understanding of the many-body instabilities and the nature of the correlated phases that are candidates for possible trilayer graphene ground states, is required.

Here, we employ the fRG approach, detailed in chapter 2 to address the problem of competing instabilities on honeycomb trilayers in an unbiased way. We explore a region of the phase diagram with a range of interaction parameters with density-density repulsions up to the second nearest neighbor that are motivated by the ab initio values as proposed in [Weh11].

An instability toward an interaction-induced QSH state is of particular interest in connection with realizing topological insulators in graphene. As discussed before, it was argued in [Rag08] that second-nearest-neighbor repulsions can lead to an interaction-induced mean-field having the same effect as the Kane-Mele mass term [KM05a]. In the single graphene layer, a non-zero interaction strength is needed to open any kind of gap [Rag08]. So far, there is no experimental evidence for this. In the bilayer system analyzed in chapter 4, we found the same instability for arbitrarily small interactions of appropriate distance dependence, and basically get two copies of the Kane-Mele QSH state coupled by the interlayer terms. The sign of the order parameter gives rise to distinct choices with interestingly different properties [ZAV12]. While this is an interesting many-body state, the corresponding spin-polarized edge modes would not be topologically protected in a strict sense as the bilayer-doubling now permits time-reversal invariant single particle terms that would localize the edge states [QZ11]. However, if one finds the same state in the trilayer system, one would again have an odd number of Kramers pairs at the edges or edge states per spin, and the topological protection would keep at least one edge mode alive. In this chapter, we show that the fRG suggests that the trilayer QSH state is not unlikely for realistic parameters, and that it can even occur at sizable energy scales ≈ 10 meV.

5.2 Models

Here, we construct the non-interacting part of the tight-binding Hamiltonians for ABC and ABA stacked trilayer honeycomb lattices. The models for trilayer

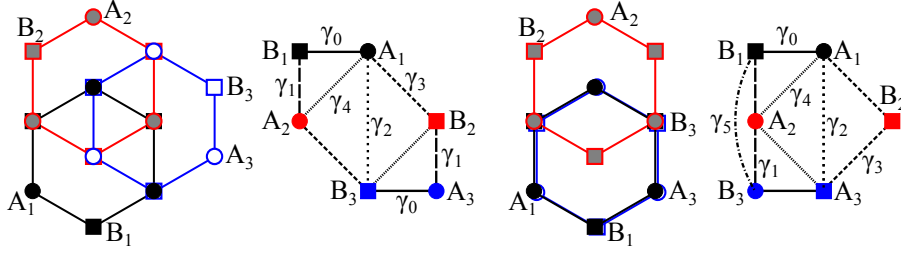


Figure 5.1: Sketch of ABC stacked trilayer graphene with trigonal warping terms (first and second plot). Sketch of ABA stacked trilayer graphene with trigonal warping terms (third and fourth plot). Hoppings are shown in side-view. Cf. [KM09; Zha10b].

honeycomb lattices are also introduced and discussed in, e.g., [KM09; Zha10b; YRK11; KM11]. The tight-binding Hamiltonian for ABC and ABA stacked trilayers is composed out of single layer Hamiltonians for the in-plane hoppings, perpendicular hoppings between different layers and remote hoppings between the layers, including a certain planar distance. We denote the different lattice sites A_1, B_1, A_2, B_2, A_3 and B_3 , where A and B specify the sublattice and the index numbers the layer as shown in figure 5.1.

The position vectors of the two-dimensional bipartite lattice structure are called R , with R being the positions of the sites of the A_2 sublattice. According to the preceding chapter, we denote the vectors, characterizing the three nearest neighbors in plane by δ_i given in equation (4.1 – 4.3). Here, the vectors point from the B-sublattice to the A-sublattice in each layer. Also, $c_{o,\sigma}(r)$ and $c_{o,\sigma}^\dagger(r)$ are annihilation and creation operators of an electron at position r and the layer and sublattice are encoded in the subscript $o \in \{A_1, B_1, A_2, B_2, A_3, B_3\}$. The index $\sigma = \uparrow, \downarrow$ specifies the electron spin as before.

With these preliminaries, we can write down the tight-binding Hamiltonian in the first two layers,

$$H_1^\parallel = -\gamma_0 \sum_{R, \delta_i, \sigma} \left(c_{B_1, \sigma}^\dagger(R) c_{A_1, \sigma}(R + \delta_i) + \text{h.c.} \right), \quad (5.1)$$

$$H_2^\parallel = -\gamma_0 \sum_{R, \delta_i, \sigma} \left(c_{B_2, \sigma}^\dagger(R - \delta_i) c_{A_2, \sigma}(R) + \text{h.c.} \right), \quad (5.2)$$

and a stacking-dependent Hamiltonian for the third layer,

$$H_{3,c}^\parallel = -\gamma_0 \sum_{R, \delta_i, \sigma} \left(c_{B_3, \sigma}^\dagger(R + c\delta_1) c_{A_3, \sigma}(R + c\delta_1 + \delta_i) + \text{h.c.} \right), \quad (5.3)$$

where we have attributed an additional index c to $H_{3,c}$, with $c = 0$ for the ABA stacking, and $c = 1$ for the ABC or chiral stacking. In graphene and few-layer graphene systems, the hopping $\gamma_0 = t \approx 3 \text{ eV}$ (see, e.g., [Zha08; Zha10b]). Next,

we introduce the interlayer hoppings, γ_1 , between sites that lie on top of each other and connect adjacent layers,

$$H_{12}^\perp = \gamma_1 \sum_{R,\sigma} \left(c_{B_1,\sigma}^\dagger(R) c_{A_2,\sigma}(R) + \text{h.c.} \right), \quad (5.4)$$

$$H_{23,0}^\perp = \gamma_1 \sum_{R,\sigma} \left(c_{B_3,\sigma}^\dagger(R) c_{A_2,\sigma}(R) + \text{h.c.} \right), \quad (5.5)$$

$$H_{23,1}^\perp = \gamma_1 \sum_{R,\sigma} \left(c_{B_2,\sigma}^\dagger(R - \delta_1) c_{A_3,\sigma}(R - \delta_1) + \text{h.c.} \right), \quad (5.6)$$

where, again, we accounted for the different stackings, by introducing $H_{23,c}^\perp$. Ab initio values for $\gamma_1 = t_\perp$ are available for graphite [DD02; KM11], $t_\perp \approx 0.4$ eV, and ABC trilayer graphene [Zha10b], $t_\perp \approx 0.5$ eV.

In figure 5.1, we also show the more remote hoppings $\gamma_2, \gamma_3, \gamma_4, \gamma_5$ whose effect is discussed below. In the present model study, we ignore these terms for most explicit calculations. For the discussion of the energy bands, we use the Fourier transform, given in equation (4.10) and write the tight-binding Hamiltonians in this approximation in Fourier space as

$$\begin{aligned} H_c^{\text{TL}} &= H_1^\parallel + H_2^\parallel + H_{3,c}^\parallel + H_{12}^\perp + H_{23,c}^\perp \\ &= \sum_{k,\sigma} \Psi_\sigma^\dagger(k) \hat{H}_c^{\text{TL}} \Psi_\sigma(k), \end{aligned} \quad (5.7)$$

with $\Psi_\sigma^\dagger(k) = (c_{A_1,\sigma}^\dagger(k), c_{B_1,\sigma}^\dagger(k), c_{A_2,\sigma}^\dagger(k), c_{B_2,\sigma}^\dagger(k), c_{A_3,\sigma}^\dagger(k), c_{B_3,\sigma}^\dagger(k))$ and

$$\hat{H}_c^{\text{TL}} = \gamma_0 \begin{pmatrix} 0 & -d_k & 0 & 0 & 0 & 0 \\ -d_k^* & 0 & \frac{\gamma_1}{\gamma_0} & 0 & 0 & 0 \\ 0 & \frac{\gamma_1}{\gamma_0} & 0 & -d_k & 0 & \frac{(1-c)\gamma_1}{\gamma_0} \\ 0 & 0 & -d_k^* & 0 & \frac{c\gamma_1}{\gamma_0} & 0 \\ 0 & 0 & 0 & \frac{c\gamma_1}{\gamma_0} & 0 & -d_k \\ 0 & 0 & \frac{(1-c)\gamma_1}{\gamma_0} & 0 & -d_k^* & 0 \end{pmatrix}, \quad (5.8)$$

where $d_k = \sum_{\delta_i} e^{ik\delta_i}$. The resulting energy bands are depicted in figure 5.2. The dispersion for ABC trilayers is very flat near the Fermi level, with cubic wavevector dependence close to the K and K' points. Hence, one should expect an enhanced role of interactions compared to ABA trilayers and AB bilayers where the wavevector dependence is quadratic (see also [Zha10b]).

Now, we discuss the effect of remote hopping terms on the band dispersion and possible implications for instabilities. For the ABC trilayer system, the density of states close to the Fermi energy has a van Hove singularity $\sim \epsilon^{-1/3}$ due to the cubic band crossing point, as pointed out before (e.g. [Xu12]). This enhances the role of interaction effects, leading to high critical scales for ordering tendencies. In our model study, we, therefore, choose to ignore remote

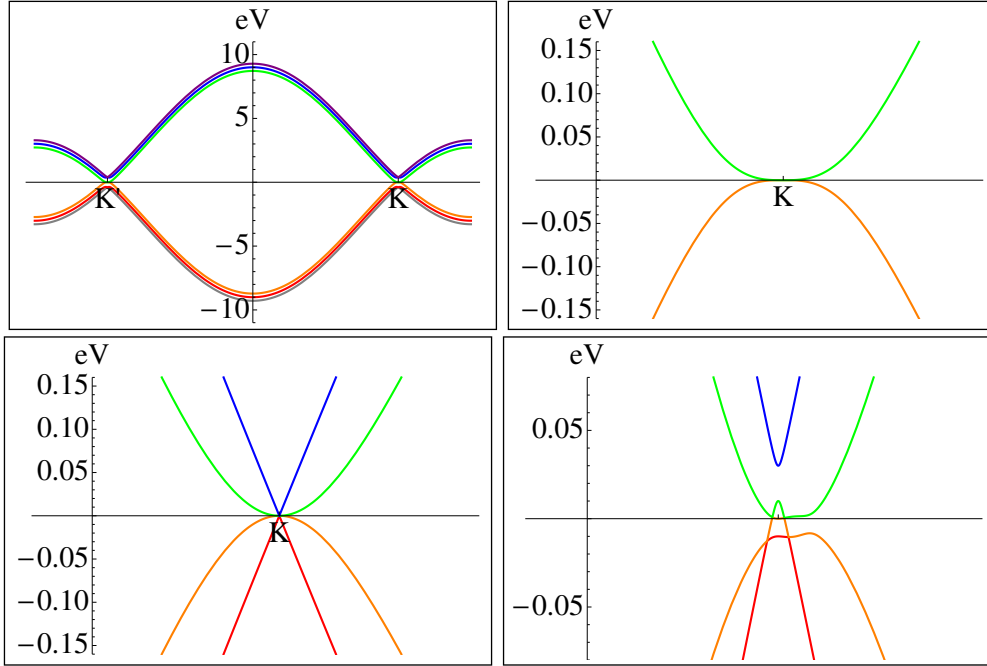


Figure 5.2: Sketch of ABC and ABA stacked trilayer graphene band-structure with $t = 3$ eV, $t_{\perp} = 0.4$ eV. Top left: ABC trilayer dispersion with $k_y = 0$. Top right: ABC trilayer dispersion close to K, K' with $k_y = 0$. Bottom left: ABA bands close to K, K' with $k_y = 0$. Bottom right: ABA bands close to K, K' with $k_y = 0$ with remote hoppings $\gamma_2, \gamma_3, \gamma_4, \gamma_5$ and on-site energy Δ' and the numerical values as given in the main text. Cf. [KM11; HNE12; Xu12].

hoppings that change the topology of the bands below an energy of order 10 meV [Zha10b], which is of the order of the measured gap in the experiment [Bao11]. Of course, it is an interesting question whether these terms affect the nature of the instability in trilayer graphene. However, we find in our computations that instabilities occur already on an energy scale that is higher than or at least comparable to $0.004t \approx 10$ meV. This serves as an a posteriori justification for dropping the remote hopping terms and proves the consistency of our approach.

In ABA trilayer, the situation is different. Here, the band-structure close to the K and K' points is separated into a linear and a quadratic subband. The remote hoppings induce separate gaps for these subbands, however, with an individual energy shift of the subbands (see also [KM11; YRK11] for a discussion of the ABA trilayer dispersion). This destroys the particle-hole nesting and the associated instabilities are suppressed (at least for small interaction terms). Explicitly, the tight-binding Hamiltonian in the presence of the important remote hoppings [DD02; KM11; ZTM12], $\gamma_2 = -0.02$ eV, $\gamma_3 = 0.3$ eV, $\gamma_4 =$

0.04 eV, $\gamma_5 = 0.04$ eV, $\Delta' = 0.05$ eV, can be written as

$$\hat{H}^* = \begin{pmatrix} 0 & -\gamma_0 d_k & \gamma_4 d_k & -\gamma_3 d_k^* & \frac{\gamma_2}{2} & 0 \\ -\gamma_0 d_k^* & \Delta' & \gamma_1 & \gamma_4 d_k & 0 & \frac{\gamma_5}{2} \\ \gamma_4 d_k^* & \gamma_1 & \Delta' & -\gamma_0 d_k & \gamma_4 d_k^* & \gamma_1 \\ -\gamma_3 d_k & \gamma_4 d_k^* & -\gamma_0 d_k^* & 0 & -\gamma_3 d_k & \gamma_4 d_k^* \\ \frac{\gamma_2}{2} & 0 & \gamma_4 d_k & -\gamma_3 d_k^* & 0 & -\gamma_0 d_k \\ 0 & \frac{\gamma_5}{2} & \gamma_1 & \gamma_4 d_k & -\gamma_0 d_k^* & \Delta' \end{pmatrix}. \quad (5.9)$$

Within the fRG approach, we show that, also for this system, flows toward many-body instabilities occur, however, only beyond a critical interaction strength, which, similarly to the single layer case, probably is larger than the interaction strength in the real material.

In order to investigate the instabilities that are possible on the trilayer honeycomb lattice for interacting electrons, we take into account a number of interaction terms, most importantly an on-site or Hubbard interaction U , a nearest-neighbor intralayer interaction V_1 and a next-nearest-neighbor intralayer interaction V_2 . For these interaction parameters ab initio parameters from cRPA computations are available [Weh11] and we take those values as a motivation for the investigated range in the phase diagram. The interaction Hamiltonian reads

$$H_I = U \sum_{r_i} n_{\uparrow}(r_i) n_{\downarrow}(r_i) + V_1 \sum_{\substack{\langle r_i, r_j \rangle, \\ \sigma, \sigma'}} n_{\sigma}(r_i) n_{\sigma'}(r_j) + V_2 \sum_{\langle\langle r_i, r_j \rangle\rangle, \sigma, \sigma'} n_{\sigma}(r_i) n_{\sigma'}(r_j), \quad (5.10)$$

where $n_{\sigma}(r_i) = c_{o,\sigma}^{\dagger}(r_i) c_{o,\sigma}(r_i)$ and r_i, r_j run over the lattice sites, but pairs are included only once. The unitary transformation from the orbital to the band degrees of freedom, diagonalizing H_0^{TL} or H_1^{TL} is performed numerically and has to be carried out on H_I as well, cf. section 2.7. This adds ‘orbital makeup’ to the interaction terms in band representation, leading to an additional angular dependence of the interactions near the K and K' points. We have already seen in chapter 3, that this has a crucial impact on the fRG flow by allowing for unconventional instabilities.

We study the fRG flow at temperature $T = 0$, employing the formalism detailed in chapter 2. We used the same approach as in the study of the bilayer system. For details of the application of this formalism, we, therefore, refer to section 4.3.

We use the scale, at which the interaction vertex exceeds a value of the order of 10 times the bandwidth, as an estimate for the critical scale. The precise choice of this value has only a minor effect on the extracted critical scale, as the couplings grow very rapidly in the vicinity of the divergence. We find flows to strong coupling with non-zero critical scales Λ_c for all choices of non-vanishing interaction terms provided there is a non-vanishing density of states at the Fermi level of the coupled layers.

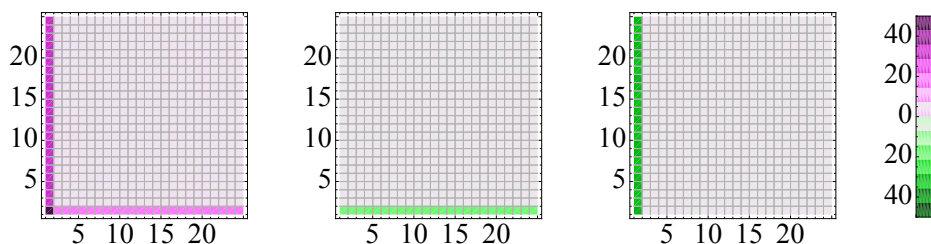


Figure 5.3: Effective interaction vertex near the critical scale in the AFM regime in units of t . Left: Orbital combinations with $o_1 = o_2 = o_3 = o_4$. The numbers on the axis specify the number of the patch as shown in figure 4.3. On the horizontal axis the wavevector k_1 can be read off, and on the vertical axis we enumerate k_2 . k_3 is fixed on the first patch, k_4 then follows from momentum conservation. Here, we see that the sharp vertical structure ($k_1 = k_3$) comes with the double magnitude as the horizontal structure ($k_2 = k_3$). Middle: Effective vertex function for the orbital combination, where $o_1 = o_3, o_2 = o_4 \neq o_1$ and if $o_1 \in \{A_1, A_2, A_3\}$, then $o_2 \in \{B_1, B_2, B_3\}$. Right: Effective vertex function for the orbital combination, where $o_1 = o_4, o_2 = o_3 \neq o_1$ and if $o_1 \in \{A_1, A_2, A_3\}$, then $o_2 \in \{B_1, B_2, B_3\}$. If in the second and third plots both $o_1, o_2 \in \{A_1, A_2, A_3\}$ or $\in \{B_1, B_2, B_3\}$, the sign of the vertices changes.

5.3 ABA and ABC Trilayer Hubbard Model

Let us start the description of the fRG results with the case of on-site interactions only, i.e. $U > 0, V_1 = V_2 = 0$. We limit the study to the charge neutrality point, i.e. with Fermi points at K and K' in the Brillouin zone.

First, we want to investigate the simpler band-structures when all remote hopping terms are neglected and only $t \neq 0$ and $t_\perp \neq 0$. Then, running the fRG flow with pure on-site interaction $U \neq 0$ in the ABC and ABA stacked trilayers, we observe an instability toward an AFM SDW with a typical signature of the interaction vertex near the instability as shown in figure 5.3. Similar to the phase, obtained in the honeycomb bilayer in chapter 4, the leading part of the effective interaction corresponding to the clearly discernible sharp structures in wavevector space reads in this case

$$H_{\text{AFM}} = -\frac{1}{\mathcal{N}} \sum_{o,o'} V_{oo'} \epsilon_o \epsilon_{o'} \vec{S}_o \vec{S}_{o'}, \quad (5.11)$$

with $V_{oo'} > 0$ and

$$\vec{S}_o = \frac{1}{2} \sum_{k,\sigma,\sigma'} \vec{\tau}_{\sigma\sigma'} c_{o,\sigma}^\dagger(k) c_{o,\sigma'}(k), \quad (5.12)$$

as in equation (4.19). The fact that the above Hamiltonian only contains the $q =$

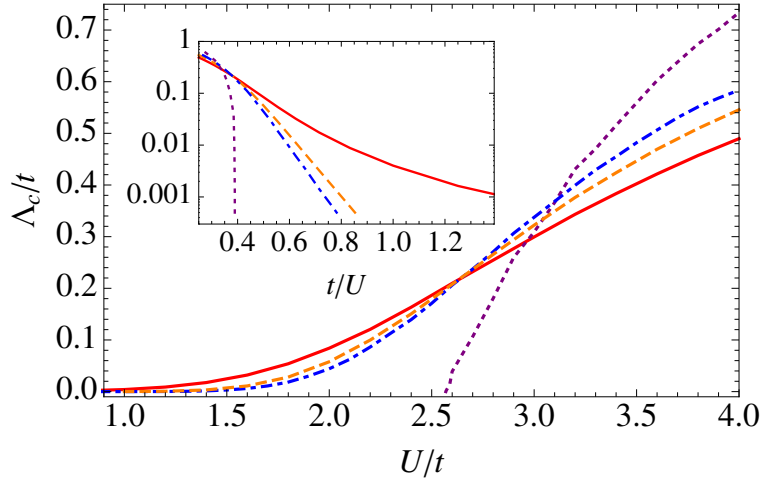


Figure 5.4: FRG critical scale for the single layer (dotted purple), the AB bilayer (dot dashed blue), the ABA trilayer (dashed orange) and the ABC trilayer (solid red). These results were obtained with $t_{\perp} = t$ and all higher hopping terms set to 0. The inset shows the same data in a semilog plot over t/U .

0 component means that the effective interaction has become infinitely-ranged [Hon08]. The factors ϵ_o depend on the orbital, $\epsilon_o = +1$ for $o \in \{A_1, A_2, A_3\}$ and $\epsilon_o = -1$ for $o \in \{B_1, B_2, B_3\}$. This sign structure implements the staggering of the interaction within the unit cell appropriate for AFM interactions. Note and that this parametrization holds in both cases, for the ABC as well as for the ABA stacking.

A mean-field decoupling of H_{AFM} results in an AFM spin alignment in each layer, where a net spin (e.g. ‘up’) moment is located on the A_1 -, A_2 -, and A_3 -sublattices, and an opposite net spin (‘down’) moment on the B_1 -, B_2 -, and B_3 -sublattices.

The critical scale Λ_c as a function of the on-site interaction U for ABC and ABA honeycomb trilayers with model hopping parameters $t = t_{\perp}$ is shown in figure 5.4, together with the critical scales of single and bilayer honeycomb lattices with the same hopping parameters. This choice of band parameters takes us beyond the regime of realistic parameters for trilayer graphene, but pronounces the characteristic features of the ABC and the ABA stacking close to the K and K' points and, therefore, allows us to study the differences of the various honeycomb stacks more explicitly. Furthermore, it allows us to make a comparison with the QMC results for the bilayer system, which we discussed in section 4.5. We add a systematic study of the dependence on t_{\perp} below. Most importantly, we observe that in the ABC trilayer, the critical scale decreases more slowly compared to AB bilayer, when the on-site interaction is decreased. While in the case of ABA trilayer and AB bilayer with QBCPs the functional dependence of $\Lambda_c(U)$ can be fitted by an exponential decay, $\sim \exp(-\alpha/U)$ (cf.

inset in figure 5.4), this does not hold for the ABC trilayer case. Instead, at small U , based on the density of states $\sim \epsilon^{-1/3}$, one would naively expect a behavior $\Lambda_c \sim U^3$. In Appendix B we derive this result within the RPA. The $\Lambda_c \sim U^3$ behavior, however, is not reproduced by our data, presumably due to the influence of the high energy sector, i.e. additional bands. We expect that the leading $\Lambda_c \sim U^3$ dependence might be recovered at smaller U and, thus, smaller Λ , which is numerically hard to access due to the rapidly decreasing critical scale.

From this analysis, we conclude that in ABC trilayers an interaction-induced gap, which we expect to be of the order of the critical scale Λ_c , may be considerably larger than in the other structures. This also implies a more stable correlated ground state. All this seems compatible with recent experiments [Bao11].

When the remote hoppings $\gamma_2, \gamma_3, \gamma_4, \gamma_5$ and the on-site energy Δ' in ABA trilayers are taken into account, the band dispersion is deformed considerably and the particle-hole nesting of the band-structure is destroyed [KM11; ZTM12], see figure 5.2. In this case, one should expect that in the weakly interacting limit the tendency toward instabilities will be strongly reduced. However, it is interesting to study what happens in the case of intermediate and larger on-site interactions.

An accurate treatment of the dispersion with remote hoppings at the lowest scales would require the implementation of a new patching scheme to resolve the vicinity of the K and K' points, i.e. the fact that the Fermi surface is now not restricted to a single point. This is beyond the scope of this work. Therefore, we now stop the flow at the energy scale Λ^* , at which the bands become non-monotonous. This procedure is routinely done in parquet- and g -ology studies of imperfectly nested bands [ZYD97; CEE08]. Of course it leaves the scales below Λ^* unintegrated, but as the dispersion at these lowest scales is not nested and partially gapped, we do not expect significant contributions of these modes to the flow. Hence, we expect that the so-obtained estimate for critical scales and U_c is already quite good. For the hopping parameters given in Refs. [KM11; ZTM12] the energy scale, at which the dispersion is not monotonous any more is given by $\Lambda^* \approx 10 \text{ meV} \approx 0.004t$.

However, it is important to note that the remote hoppings already change the dispersion far above the scale Λ^* . This explains why, for the ABA stacking (henceforth called ABA* stacking when the remote hopping are included), the effect of the remote hoppings is quite drastic. Studying, again, the case of on-site interactions U only, we observe clearly diverging susceptibilities only for on-site interactions $U \gtrsim 2.6t$ at critical scales well above $0.004t$. For smaller interactions, the couplings grow very slowly and no divergences at finite scales above Λ^* can be identified. In figure 5.5, we show the fRG results for the critical scales for the ABA* trilayer with remote hopping terms. For comparison, we also show the curves for the single and bilayer systems. As the similarity to

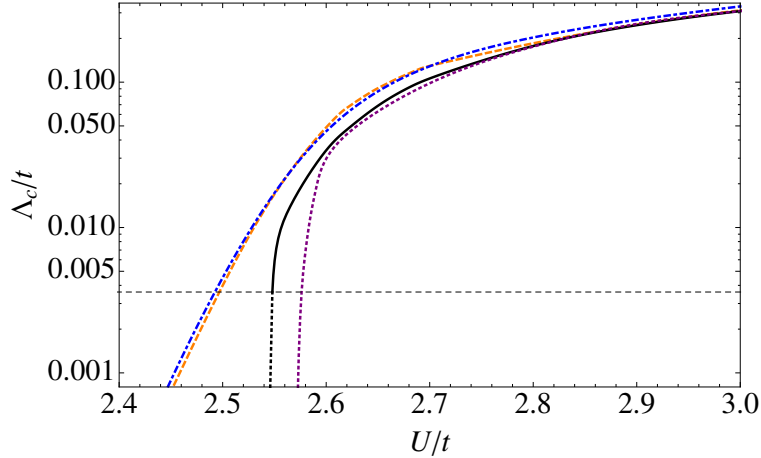


Figure 5.5: Critical scale of ABA-trilayer including remote hoppings (denoted ABA*, solid black), with the ratios of the hopping parameters corresponding to the realistic values [KM11; ZTM12], and with pure on-site repulsion U as interaction. For comparison, we also show the critical scales of ABA-trilayer without remote hoppings (dashed orange), AB bilayer (dotted dashed blue), both with the choice $t_{\perp} = 0.1t$, and the single layer system (dotted purple). The dashed horizontal line visualizes the energy scale Λ^* where the bands become non-monotonous, due to remote hoppings.

the single layer is strong, this analysis suggests a critical on-site interaction $U_c \approx 2.6t$, above which, a many-body instability can occur in the ABA* stacking with remote hopping included. We would like to add that the fRG in the present approximation has the tendency to overestimate critical scales. Therefore, we would expect the true U_c to be slightly larger. For instance, as discussed in section 4.5, in the single layer system for on-site interactions only, QMC gives $U_{c,\text{QMC}} \approx 4.3t$ for the opening of a single particle gap [Men10], while, in the fRG, we find $U_c \approx 2.6t$ as well (see figure 5.4).

The experimental study in [Bao11] does not find a gap for ABA* trilayer graphene. This is compatible with our findings, given that the interactions in real material are weaker than this critical value. This is to be expected for consistency, as the critical interaction strengths of the single layer and the ABA*-trilayer are roughly the same, and the single layer remains semimetallic, too. Even if they are slightly above the threshold, the expected transport gaps would be small and very hard to measure. Therefore, while a precise quantitative picture cannot be obtained with our approximate fRG method and here for on-site interactions only, on a qualitative level, we reach consistent conclusions. It would be interesting to resolve better the critical region close to $U_{c,\text{TL}}$ for the ABA* stacked trilayer with remote hoppings and analyze the onset of instabilities and their nature. However, this would require a different

implementation of our patching scheme, which we leave for future work. In the remainder of this chapter, we, therefore, concentrate on a more thorough study of the ABC trilayer model.

5.4 ABC trilayer: Instabilities and Phase Diagram with Non-Local Interactions

From the results for pure on-site interactions and also inspired by recent experiments, we conclude that while ABC trilayers strongly support the formation of many-body states, the ABA* trilayer, including remote hoppings, most probably does not. We take this as a motivation to study further the instabilities of ABC trilayers for a wider range of non-local interaction parameters, which brings us closer to the real materials. Ab initio values for the strength of the density-density interactions up to the third nearest neighbor were listed for single layer graphene and graphite in [Weh11]. Most likely, one can safely interpolate the parameters for the bi- and trilayer case from these data.

Running the fRG for extended interactions, we find a number of different phases similar to the ones, described in the preceding chapter 4 for the bilayer case, namely a CDW, a QSH and CDW with non-zero momentum transfer (CDW₃) alongside the AFM SDW. For the investigation of the phase diagram, we take into account non-local interaction contributions, namely the nearest-neighbor in-plane interaction V_1 and the second-nearest-neighbor in-plane interaction V_2 . More remote interaction contributions are neglected. In the bilayer case (chapter 4), we checked explicitly that a third-nearest-neighbor interaction, V_3 , does not change the picture. Also, we do not consider interlayer interactions. The ab initio calculations in [Weh11] showed that the nearest interlayer interactions in graphite (as well as in layered graphene) are of the order of the V_3 -term.¹

The two leading non-local interaction terms V_1 and V_2 trigger the appearance of qualitatively different instabilities. For a dominating V_1 , we find an instability toward a CDW with a momentum signature of the effective interaction as shown in figure 5.6. This momentum structure can be written down as an effective interaction Hamiltonian of the form,

$$H_{\text{CDW}} = -\frac{1}{\mathcal{N}} \sum_{o,o'} V_{oo'} \epsilon_o \epsilon_{o'} n_o n_{o'} , \quad (5.13)$$

with $V_{oo'} > 0$ and

$$n_o = \sum_{k,\sigma} c_{o,\sigma}^\dagger(k) c_{o,\sigma}(k) . \quad (5.14)$$

Also, $\epsilon_o = +1$ for $o \in \{A_1, A_2, A_3\}$ and $\epsilon_o = -1$ for $o \in \{B_1, B_2, B_3\}$ as in the preceding section. This sign structure supports an enhanced occupancy of

¹T. O. Wehling, private communication.

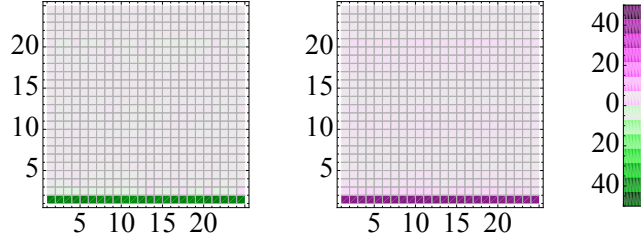


Figure 5.6: Effective interaction vertex near the critical scale in the CDW regime for $U = 0$, $V_1 = 0.5t$ and $V_2 = 0$ in units of t . Left: Orbital combinations with $o_1 = o_2 = o_3 = o_4$. The numbers on the axis specify the number of the patch as shown in figure 4.3. On the horizontal axis the wavevector k_1 can be read off and on the vertical axis we enumerate k_2 . k_3 is fixed on the first patch, k_4 then follows from momentum conservation. Right: Effective vertex function for the orbital combination, where $o_1 = o_3, o_2 = o_4 \neq o_1$ and if $o_1 \in \{A_1, A_2, A_3\}$, then $o_2 \in \{B_1, B_2, B_3\}$. If, in the right plot, both $o_1, o_2 \in \{A_1, A_2, A_3\}$ or $\in \{B_1, B_2, B_3\}$ the sign of the vertices changes.

the A_i sublattices compared to the B_i sublattices, or vice versa. Furthermore, a mean-field decoupling of this effective interaction gives a gap in the single particle spectrum.

A dominating V_2 yields an instability whose dominant interaction terms (see figure 5.7) can be cast into an effective Hamiltonian of the following type

$$H_{\text{QSH}} = -\frac{1}{\mathcal{N}} \sum_{o,o'} V_{oo'} \epsilon_o \epsilon_{o'} \vec{S}_o^f \vec{S}_{o'}^f, \quad (5.15)$$

with $V_{oo'} > 0$ and

$$\vec{S}_o^f = \frac{1}{2} \sum_{k,\sigma,\sigma'} f_k \vec{\tau}_{\sigma\sigma'} c_{o,\sigma}^\dagger(k) c_{o,\sigma'}(k), \quad (5.16)$$

including a f -wave form factor $f_k = \sin(\sqrt{3}ak_x) - 2 \sin(\frac{\sqrt{3}ak_x}{2}) \cos(\frac{3ak_y}{2})$. This effective Hamiltonian can be decoupled in a purely imaginary Kane-Mele order parameter, similar to equation (4.24). This type of instability represents a many-body path to the QSH state, where the mass term due to spin-orbit interaction in the original Kane-Mele proposal [KM05a] is now provided by an interaction-induced mean-field. In the single layer [Rag08] and bilayer honeycomb models, this instability was found in the same corner of interaction parameter space. For an odd number of layers, the mean-field Kane-Mele-ordered state will give rise to an odd number of helical edge modes, and, thus, represent a two-dimensional interaction-driven topological insulator with protected edge modes.

Finally, in the niche of the parameter space for smaller U , we also recover

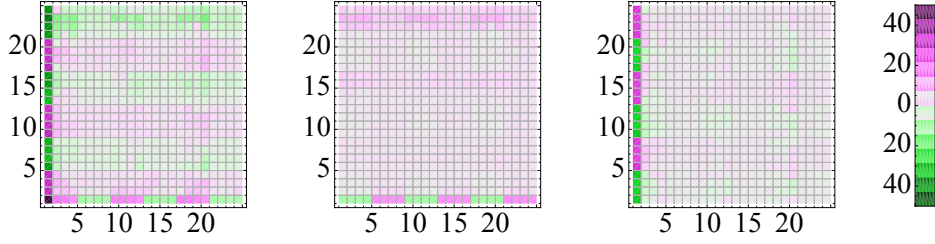


Figure 5.7: Effective interaction vertex near the critical scale in the QSH regime for $U = 0$, $V_1 = 0$ and $V_2 = 1.5t$ in units of t . Left: Orbital combinations with $o_1 = o_2 = o_3 = o_4$. The numbers on the axis specify the number of the patch as shown in figure 4.3. On the horizontal axis the wavevector k_1 can be read off and on the vertical axis we enumerate k_2 . k_3 is fixed on the first patch, k_4 then follows from momentum conservation. Here, we see that the sharp vertical structure ($k_1 = k_3$) comes with the double magnitude as the horizontal structure ($k_2 = k_3$). Middle: Effective vertex function for the orbital combination, where $o_1 = o_3, o_2 = o_4 \neq o_1$ and if $o_1 \in \{A_1, A_2, A_3\}$, then $o_2 \in \{B_1, B_2, B_3\}$. Right: Effective vertex function for the orbital combination, where $o_1 = o_4, o_2 = o_3 \neq o_1$ and if $o_1 \in \{A_1, A_2, A_3\}$, then $o_2 \in \{B_1, B_2, B_3\}$. If, in the second and third plots both $o_1, o_2 \in \{A_1, A_2, A_3\}$ or $\in \{B_1, B_2, B_3\}$ the sign of the vertices changes .

the CDW₃ phase, which we already found in the bilayer system,

$$H_{\text{CDW}_3} = -\frac{1}{\mathcal{N}} \sum_{o,o'} V_{oo'} \epsilon_o \epsilon_{o'} (n_o(Q) n_{o'}(-Q) + n_o(-Q) n_{o'}(Q)) , \quad (5.17)$$

with

$$n_o(Q) = \sum_{k,\sigma} c_{o,\sigma}^\dagger(k+Q) c_{o,\sigma}(k) . \quad (5.18)$$

The sum over k is restricted to the vicinity of the K and K' points, as only there the interactions grow large. See figure 5.8 for the characteristic momentum structure of the effective interaction. The order parameter due to the symmetry breaking $\langle n_o(Q) \rangle \neq 0$ is in complete analogy with the one in the honeycomb bilayer in chapter 4, except for the adapted definition of the ϵ_o . Within one layer, this order forms three inequivalent sites with different charge densities. The sign structure of the order parameter on different layers and sublattices is determined by the ϵ_o factors, so as to lower the energy contribution from (5.17). This leaves the total phase of the order parameter undetermined, cf. equation (4.27). Depending on this phase, the quadratic mean-field Hamiltonian for a single layer can exhibit a gapped or gapless spectrum.

For a systematic investigation of the ABC trilayer phase diagram, we scan

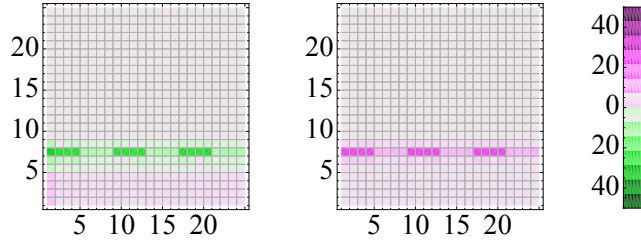


Figure 5.8: Effective interaction vertex near the critical scale in the CDW_3 regime for $U = 0$, $V_1 = 0$ and $V_2 = 0.5t$ in units of t . Left: Orbital combinations with $o_1 = o_2 = o_3 = o_4$. The numbers on the axis specify the number of the patch as shown in figure 4.3. On the horizontal axis the wavevector k_1 can be read off and on the vertical axis we enumerate k_2 . k_3 is fixed on the first patch, k_4 then follows from momentum conservation. Here, we see that the order parameter has non-vanishing momentum transfer as the sharp feature is not at $k_1 = k_3$. Right: Effective vertex function for the orbital combination, where $o_1 = o_3, o_2 = o_4 \neq o_1$ and if $o_1 \in \{A_1, A_2, A_3\}$, then $o_2 \in \{B_1, B_2, B_3\}$. If, in the right plot, both $o_1, o_2 \in \{A_1, A_2, A_3\}$ or $\in \{B_1, B_2, B_3\}$ the sign of the vertices changes.

a range of interaction parameters U , V_1 , and V_2 , whose ab initio values are listed in [Weh11]. As we expect the fRG to overestimate the critical scales, we take these ab initio parameters as upper bounds for the range of our phase diagrams. In figure 5.9, we show the fRG phase diagram obtained by identifying the leading tendencies in the effective interactions near the instability with an underlying contour plot of the critical scale Λ_c in units of t .

We also mark the ab initio values in the lower plots in figure 5.9, obtained by taking the values from [Weh11] and scaling $\{U, V_1, V_2\} \rightarrow \alpha\{U, V_1, V_2\}$, so as to hit the values $U = 2t$ and $U = 3t$. In both cases, these choices place the system near the phase boundary between QSH and AFM SDW instability. For the more long-ranged single layer graphene interactions, one finds a QSH state, while for the slightly shorter ranged graphite parameters, one gets an AFM SDW state. Hence, which order occurs, might be a delicate issue that is decided by details. In our approximation, the critical scales interpolate smoothly across the phase borders, indicating a weaker competition between the different tendencies.

Note, that due to this borderline situation, there is no true necessity for different layered graphene systems, e.g. with different environments, to exhibit the same ground state, and even the energy scales or gaps could come out similarly despite different states being selected. Hence, regarding the leading instability, the situation in the ABC trilayer is very similar to the one found in the Bernal-stacked bilayer system in chapter 4.

As mentioned before, we also find a rather exotic density-wave phase CDW_3 , with a tripling of the unit cell, within the layers. This state is subject to

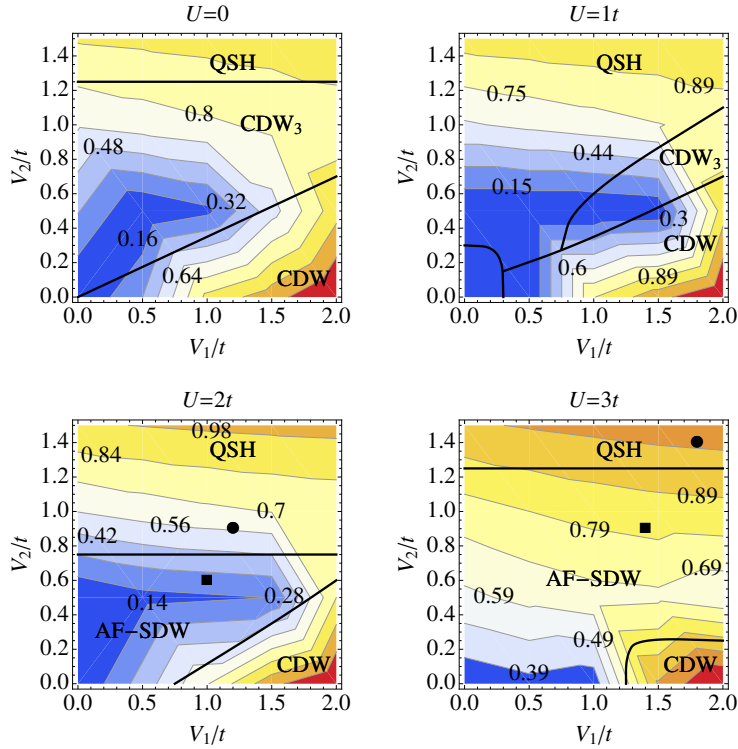


Figure 5.9: Tentative fRG phase diagram of the ABC trilayer with $t_{\perp} = 0.1t$. The black lines are guides to the eye and separate the different regimes. The contour plot encodes the critical scale, at which the vertices diverge. The rescaled ab initio interaction parameters for graphene (circles) and graphite (squares) in [Weh11] are shown in the lower plots.

further investigation. However, it occurs only at quite unrealistic corners of the parameter space with dominant non-local terms. Hence, we do not discuss it further here.

5.5 Energy Scales of the Ordering Phenomena

In section 4.5, in the study of the bilayer system, we encountered a problem with current model studies that in principle also affects the results in the trilayer case. Here, we discuss this issue again, and offer an explanation of what happens and how one should read the data, in order to get reasonable agreement with and a more quantitative picture of the experiments.

As shown in this and the preceding chapter, the simple models employed by virtually all many-body approaches to interaction effects in few-layer graphene can produce very large critical scales. This can be seen in figure 5.9, where we indicate the values of the critical scales in units of the hopping $t \approx 3 \text{ eV}$. These scales are huge for most choices of the interaction parameters. This

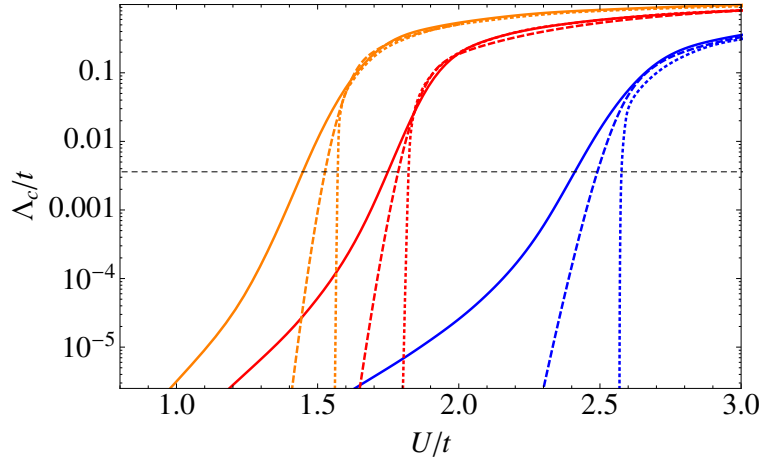


Figure 5.10: FRG critical scale for ABC trilayer for the pure Hubbard model (blue solid) and rescaled ab initio parameters for graphite (red solid) and single layer graphene (orange solid) as described in the text with $t_{\perp} = 0.1t$. For comparison, we also show the corresponding critical scale for the AB bilayer structure (dashed) and the single layer structure (dotted). For the Hubbard (blue curves) and the rescaled graphite parameters (red curves), we find the system to be in the AFM SDW phase, for the rescaled graphene parameters the system is in the QSH state (orange curves). The dashed horizontal line marks 10 meV, which is the order of magnitude, where the topology of the band structure in ABC trilayer graphene changes and remote hoppings become important.

is not surprising. In our and other theoretical approaches, the large scales are simply caused by the perfect particle-hole nesting of the band-structure. Furthermore, from the comparison with QMC calculations in the case of pure on-site interactions in section 4.5 we know that the overestimate of the fRG is certainly not severe and, expressed conservatively, is less than an order of magnitude in the regime where also the QMC finds robust ordering. As the critical scale is an estimate for the energy scale of the spectral restructuring or gap opening in the ordered phase, a high critical scale would correspond to large energy gaps. If we took the ab initio parameters of [Weh11] literally, the theoretical gap estimates would exceed the experimentally observed gap scales $\approx 1 - 10$ meV by orders of magnitude.

Let us now analyze the systematics of these critical scales, a bit more deeply. In figure 5.10, we show the critical scales obtained from fRG for single, bi- and trilayer graphene for three cases, namely for on-site interaction U only, and for non-local interactions with the cRPA parameters V_1 and V_2 for graphite and graphene with repulsions up to the second nearest neighbor, for realistic interlayer hopping $t_{\perp} = 0.1t$. The curves show the dependence on the overall

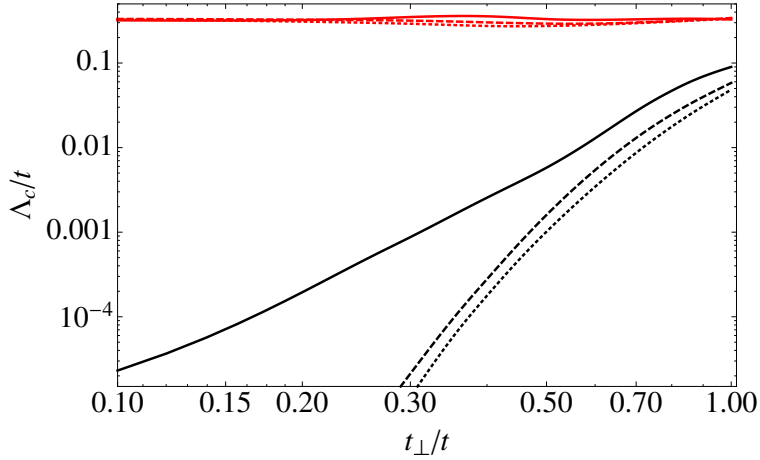


Figure 5.11: FRG critical scale for ABC trilayer (solid lines), ABA trilayer without remote hoppings (dashed lines), and AB bilayer (dotted lines) with fixed on-site interaction and variable t_{\perp} . The red lines show the results for $U = 3t > U_{c,SL}$ and no dependence of the critical scale on the interlayer hopping t_{\perp} . For the case $U = 2t < U_{c,SL}$ (black lines), we observe a strong dependence of the critical scale on t_{\perp} .

magnitude of the on-site interaction, where the ratio between the local U and the non-local interaction parameters is kept fixed. Obviously, there are two regimes: a high-scale regime with large critical scales that do not depend too strongly on the interaction strength, and a low-scale regime with a very strong dependence on the interaction. For the single layer, the second regime is very narrow and basically only contains the minimal critical interaction strength $U_c(V_1, V_2)$, below which, the semimetal is stable. Also, for bi- and trilayer, the high-scale regime starts above the single layer $U_c(V_1, V_2)$.

Next, let us consider the dependence of the critical scale Λ_c on the interlayer hopping t_{\perp} in the ABC trilayer. Whereas, the nature of the ground state qualitatively remains the same for all choices of $t_{\perp} \neq 0$ the absolute value of this parameter has an impact on the size of the critical scale and shows different behaviors on the two different sides of the critical on-site interaction of single layer graphene $U_{c,SL}$ (see figure 5.11) i.e., whether we are in the high-scale or in the low-scale regime. For large interactions, $U > U_{c,SL}$, the size of t_{\perp} is of no importance for the critical scale Λ_c . This changes for smaller U . Here, the smaller t_{\perp} is, the stronger is the Λ_c -variation with the interaction strength.

The comparison with QMC in section 4.5 was done at larger $t_{\perp} = t$ and $U \geq 2.8t$, where the scales do not vary that strongly. For band-structure parameters with $t_{\perp} \lesssim 0.1t$ and small interactions $U \lesssim U_{c,SL}$, we also observe flows to strong coupling for the ABC and the ABA trilayer systems. However, the critical

scales turn out to be very small, an effect that reflects the behavior of the single layer system, where no instabilities occur for $U < U_{c,SL}$. While this does not constitute a difficulty for the fRG method per se, it makes the numerical evaluation very tedious and renders comparison with QMC impossible.

We now argue that in order to account for the approximations made in the fRG scheme, mainly the neglect of self-energy corrections, and in order to obtain a realistic picture, we have to reduce the cRPA parameters with $U \approx 3t$ by hand. The reduction factor is chosen so as to obtain the experimentally verified semimetallic solution for the single layer case, i.e. roughly to $U \approx 1.5t$ (if we take the single layer cRPA values) with an analogous rescaling of the non-local couplings by the same factor. This shift on the interaction axis now takes us from the high scale regime into the regime of strongly varying scales, cf. figure 5.10. Now, the critical scales for bi- and trilayer end up in the range $\lesssim 0.01t \approx 30$ meV which is much closer to the experimental values for gap sizes and already in the correct order of magnitude.

In the experiments on bi- and trilayer graphene of these types, the energy gap in the trilayer [Bao11] came out higher by a factor 2-3 than in the bilayer [Vel12a; Fre12; Bao12; Vel12b]. In the fRG, the ratio between the critical scales for these two systems depends on the parameter values for the interactions. However, for interactions where single layer graphene does not undergo a phase transition, the larger density of states near the Fermi level of the trilayer case leads to a larger critical scale in theory as well, see figure 5.10. Hence the different energy gaps in bi- and trilayers are qualitatively captured by this theory. Remarkably, with this choice of interaction parameters, the instabilities in ABC trilayer occur on an energy scale where remote hoppings start to be important (≈ 10 meV, see figure 5.10).

5.6 Conclusion

We have performed extensive fRG calculations on honeycomb trilayer systems with different stacking orders, as model systems for trilayer graphene. In doing this, we have used as much as possible the available input parameters from ab initio calculations. Moreover, we have taken into account the full six-band band-structure obtained within the model with one effective p_z -type orbital per carbon site.

First, let us mention the main results of the present trilayer study, before we get to the connections with graphene systems and experiments. Comparing the different trilayer stackings with the Bernal-stacked bilayer and the monolayer results, we could identify the ABC trilayer as the system that is most prone toward instabilities, with larger energy scales for ordering than the AB-bilayer. The ABA trilayer, without the additional interlayer remote hoppings, is comparable in its critical scales to the bilayer, but we showed that the remote hopping terms with the suggested realistic parameter values (called ABA*

structure here) are likely to remove the instability, at least for smaller, possibly realistic, interaction strengths. Interestingly, for the Hubbard on-site interaction case, the minimal U value for obtaining a gapped ground state in the ABA* structure is close to the one for the single layer. Taking the current experimental knowledge for bi- and trilayer graphene, these theoretical findings regarding the systematic differences are fully consistent with the observations.

Due to the uncertainties about the parameter values for the theoretical model and the approximations made in our approach, we cannot expect a fully quantitative description. However, the phenomenological input of requiring the single layer to remain semi-metallic puts bounds on the bare interaction parameters that should be used in our model. The idea used in section 5.5 is to scale down the ab initio parameters for the interactions by an appropriate factor in order to compensate for the approximations, so as to render the fRG flow for the single layer free of divergences. With this remedy for the inexactness of our approach, the ABA* trilayer with remote hoppings remains semi-metallic and the energy scales of the unstable systems, namely the bilayer and the ABC trilayer, come out in a quite realistic region below 30 meV.

For the interaction parameters determined by ab initio methods [Weh11], our calculations show a strong competition between AFM SDW ordering and the interaction-driven Kane-Mele QSH state. As in the bilayer model, we did not encounter a nematic instability. For the trilayer, a recent self-consistent study by Jung and MacDonald [JM12] found good qualitative agreement with our studies. The nematic order was shown to be unstable in this case.

Which tendency wins depends on the detailed spatial profile of the interactions. A more longer ranged behavior favors the QSH instability, and for pure on-site repulsions, the AF-SDW state is the clear winner. Both states would open up a bulk gap. The SDW states should have an interesting modulation of the ordered moments depending on the number of nearest neighbors, with smaller moments for higher coordination numbers [Lan12]. The QSH state should be a true two-dimensional topological insulator for the trilayer case, as time-reversal invariant edge defects will not suffice to gap the three pairs of helical edge states completely, in contrast to the bilayer case (for a discussion of the edge-state robustness, see [QZ11]). Hence, at least one pair of counter moving, spin-resolved helical edge states should survive time-reversal-invariant edge disorder and could, hence, serve as a smoking gun for such a correlated ground state. This perspective is rather exciting, as this would be the first realization of the concept of an interaction-driven topological insulator ('topological Mott insulator' [Rag08]).

Chapter 6

Multiband Effects on Superconducting Instabilities Driven by Electron-Electron Interactions

In this chapter, we explore multi-band effects on d-wave superconducting instabilities driven by electron-electron interactions. Our models on the two-dimensional square lattice consist of a main band, with an extended Fermi surface and predominant weight from $d_{x^2-y^2}$ orbitals, whose orbital character is influenced by the admixture of other energetically neighboring orbitals. We study how the energy scale for pairing and, hence, the critical temperature is affected by the band-structure and find that a reduction of orbital admixture as function of the orbital energies can cause a T_c -enhancement, although the Fermi surface becomes more curved and hence less favorable for AFM spin-fluctuations. While our study does not allow a quantitative understanding of the T_c differences in realistic high- T_c cuprate systems, it may reveal an underlying mechanism contributing to the actual material trends.

Large parts of this chapter have previously been published in [UH12a].

Contents

6.1	Introduction	85
6.2	Models	88
6.3	Functional Renormalization Group Treatment	91
6.4	Results for the Two-Band Model	93
6.5	Simplified Picture: Two-Patch Model	95
6.6	Results for the Three-Band Model	98
6.7	Conclusion	104

6.1 Introduction

In the research on iron superconductors (for a review, see e.g. [PG10]), theorists have undertaken efforts to determine how details of the crystal and, hence, electronic structure can account for the differences in the transition temperatures, and in the form of the superconducting gap through the families of

compounds [Kur09; IAK10; Zha10c; Tho11a; Pla12]. Similar ideas were then applied to the cuprates as well [Sak10]. These works tackle the full complexity of the many-orbital problem with approximate many-body techniques. The results are interesting and promising, as they show the existence of various tuning parameters for T_c . On the other hand, the problem of correlation-driven superconductivity should also be approached from a constructive point of view using simpler models, by asking what changes occur if one takes a separated Fermi surface with a superconducting instability, and adds to it the orbital character of the band, or allows other bands to come close in energy. The main question is whether one can find explainable trends that can be used as guide lines in a search for higher T_c 's or other desired properties. This is one of the motivations for the study described in this chapter.

Another direct motivation for considering electron-electron-interaction-driven pairing in multiband models is the T_c trend in the high- T_c cuprates. As pointed out by O.K. Andersen's group [Pav01], there appears to be a positive correlation between the experimental T_c 's and the theoretically derived second-nearest-neighbor hopping parameter t' or a related parameter r . Here, the higher T_c 's occur for a rounder Fermi surface, i.e., for larger t' and larger r . This contradicts at least the naive expectations in a spin-fluctuation-induced pairing scenario, where a smaller amount of nesting leads to a weaker pairing interaction, and, hence, a round Fermi surface with larger t' should, at least over some parameter range, have a smaller T_c . This thinking is purely based on the geometry of the Fermi surface (plus van Hove singularities nearby) and does not include any information on the orbital content of the band at the Fermi level. Also numerical studies on the one-band Hubbard model using the dynamical cluster approach [Mai00] and density matrix renormalization group calculations on t - J ladders [WS99] have shown the trend that a larger t' leads to smaller T_c , in contradiction with the above mentioned findings (see also [SB07]). Only in the t - t' - J model, comprehensive QMC studies by Spanu et al. [Spa08] showed a slight enhancement of pairing at optimal doping with non-zero t' , however, to a smaller extent than in earlier variational QMC studies by Shih et al. [Shi04]. Hence, in the one-band model, both at weak and strong coupling, the theoretical expectations are inconclusive and certainly not fully consistent with the empirical trend. The simple question, now, is whether the theoretical picture is altered, when orbital information of the multiband case is included. Therefore, we revisit this problem in simple multiband models for the band-structure of the cuprates.

The change of the next-nearest-neighbor hopping parameter t' is caused by changes in the multiorbital electronic structure of the cuprates. In downfolded four-orbital models for the cuprates [Pav01; Han09], its increase is related to a lowering in energy of the so-called axial orbital toward the Cu $3d_{x^2-y^2}$ -level. The axial orbital is basically a linear antibonding combination of the local Cu $4s$ and the surrounding oxygen $2p_z$ states. It can be decreased by reducing

the overlap between these two orbitals, which happens if the oxygens move further out of plane [Han09]. In this way, crystal and electronic structures are correlated, and the hope is to relate the structural differences between different cuprates to the differences in their superconducting properties.

The material trend pointed out by Pavarini et al. [Pav01] also spurred exciting suggestions to produce band-structures and Fermi surfaces with even higher r parameters in $\text{LaNiO}_3/\text{LaAlO}_3$ -heterostructures [Han09]. For such systems, taking over the trend from the cuprates would result in T_c 's above 100K . Therefore, a more detailed understanding of the relation between the low-lying electronic structure and the superconducting transition temperature becomes an important question in the field of tailored transition metal oxide systems.

The relation of finer differences in the multiband electronic structure to the pairing strength for different cuprates has been addressed theoretically, by at least two works. Kent et al. [Ken08] studied downfolded dpp three-band Hubbard models using the dynamical cluster approach with QMC impurity solver. The authors found a very strong sensitivity of the resulting T_c on choice of the downfolding technique and the localization of the Wannier functions. Small longer ranged hopping had a marked influence on the results. We take this as an indication that a direct parameter-free theoretical approach with a non-perturbative (cluster) many-body technique is still too challenging, and that a qualitative understanding of how the different building blocks of the model affect the resulting T_c 's would be very useful.

A theoretical study that was successful in obtaining a significant difference in pairing strength between La-based and Hg-based cuprates in the right direction came from the group around Kuroki, Arita, and Aoki [Sak10]. These authors considered two- and three-orbital models obtained using maximally localized Wannier orbitals to represent the low-lying DFT band-structure. The models were then treated by the fluctuation-exchange (FLEX) approximation, which yields effective coupling strengths for d -wave pairing. Upon changing the oxygen height h_O with respect to the Cu plane, the band-structure was altered continuously from a situation corresponding to La_2CuO_4 to roughly that of $\text{HgBa}_2\text{CuO}_4$. The parameter in the two- or three-orbital models, that responded most to this structural change, was the difference ΔE of the on-site kinetic energy between the two Cu $3d_{x^2-y^2}$ ($d_{x^2-y^2}$)- and Cu $3d_{3z^2-r^2}$ (d_{z^2})-dominated Wannier states. If a third Cu $4s$ (s) orbital was included into the model, its energy difference to the d_{z^2} was found to be roughly constant along this patch, while in the two-orbital model, this change was effectively absorbed into the model parameters. In both models, the coupling strength for d -wave pairing was found to increase when h_O or ΔE were increased, i.e., when the axial s level moved closer to the $d_{x^2-y^2}$ -level from above, and the d_{z^2} moved further down below the $d_{x^2-y^2}$ -level. Along this patch, the Fermi surface became more rounded. This study shows, that differences in pairing strength can indeed be related to changes in two- or three-band model parameters. The

present study was motivated by this work. The goal of the study described in this chapter is to acquire a clearer understanding why these model parameters changes actually the pairing strength in a d -wave pairing situation, and if one can identify a simple mechanism behind the observed trends. This might be useful for prescribing other band-structures that should have high transition temperatures. Below we will show that in the weak-coupling picture, there is actually a parameter window, where the detrimental effect of orbital admixture to the $d_{x^2-y^2}$ -like conduction band is reduced more strongly than the other negative factor of Fermi surface rounding increases. This can lead to an increase in the pairing scale as function of the relevant parameters.

6.2 Models

First, we study a two-orbital model that can be thought to arise from one s -like and one planar $d_{x^2-y^2}$ -like orbital on the two-dimensional square lattice [And95]. All other relevant orbitals, e.g., oxygen p states, should be considered as included in these effective orbitals. The free Hamiltonian reads

$$H = \sum_{k,\sigma} \begin{pmatrix} c_{s,\sigma}^\dagger(k) \\ c_{d,\sigma}^\dagger(k) \end{pmatrix}^T \begin{pmatrix} \epsilon_s(k) + \Delta E_{sd} - \mu & v(k) \\ v(k) & \epsilon_d(k) - \mu \end{pmatrix} \begin{pmatrix} c_{s,\sigma}(k) \\ c_{d,\sigma}(k) \end{pmatrix}, \quad (6.1)$$

with the nearest-neighbor hopping dispersions $\epsilon_{s/d}(k) = -2t_{s/d}(\cos k_x + \cos k_y)$, the hybridization term $v(k) = -2t_{sd}(\cos k_x - \cos k_y)$ and the chemical potential μ . Here, $t_{s/d}$ denotes the hoppings within the s or $d_{x^2-y^2}$ orbital respectively, t_{sd} is the hopping between the two orbitals, k is the momentum vector in the Brillouin zone and $\sigma \in \{\uparrow, \downarrow\}$ denotes the spin projection. $c_{s/d,\sigma}^\dagger(k)$, $c_{s/d,\sigma}(k)$ are creation and annihilation operator of a single particle excitation in the s or $d_{x^2-y^2}$ orbital respectively. The d -wave like symmetry of $v(k)$ arises due to the symmetry of the orbitals that hybridize. The lattice constant has been set to unity.

With a proper chosen field transformation of the type of equation (2.29) the matrix in orbital space can be diagonalized, leading to two bands. We are interested in the situation where ΔE_{sd} is rather large and positive. In this case, only the band which is dominated by the contribution of the $d_{x^2-y^2}$ orbital has a Fermi surface. For chemical potential $\mu = 0$ and large ΔE_{sd} , the Fermi surface is a perfectly nested square, while, if we decrease ΔE_{sd} , the Fermi surface gets rounded by the hybridization term. For the lower band around the Fermi level, we have the dispersion

$$E_c(k) = \frac{\epsilon_s(k) + \Delta E_{sd} + \epsilon_d(k)}{2} - \mu - \sqrt{\left[\frac{\epsilon_s(k) + \Delta E_{sd} - \epsilon_d(k)}{2} \right]^2 + v^2(k)}. \quad (6.2)$$

The Fermi surface opens up at the van Hove points and becomes similar on

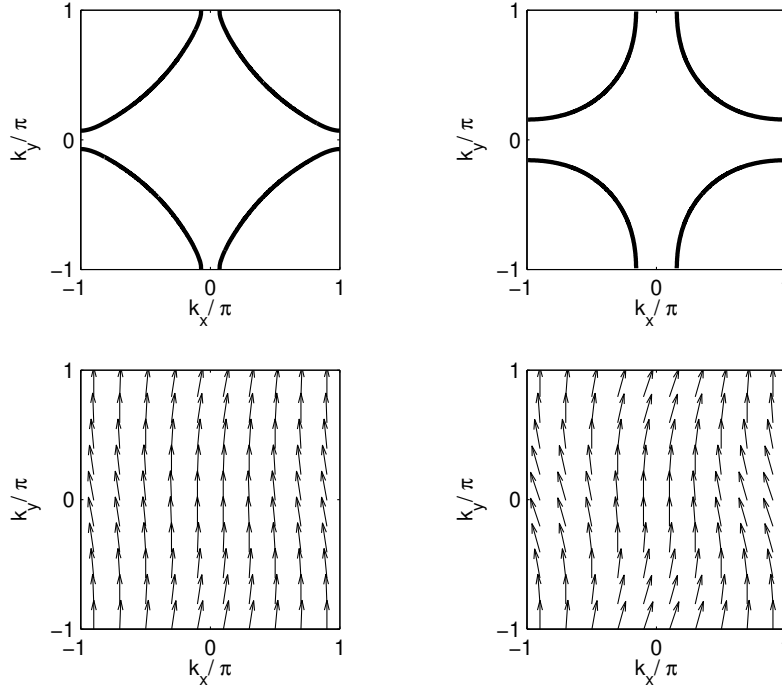


Figure 6.1: Left: Fermi surface of the two-band model for large $\Delta E_{sd} = 12eV$; $t_d = 0.45eV$, $t_s = 0.5eV$, $t_{sd} = 0.6eV$ (upper plot), and the orbital weights of the lower $d_{x^2-y^2}$ -like band through the Brillouin zone (lower plot). The vertical component of the vector arrows represents the $d_{x^2-y^2}$ orbital admixture, and the horizontal component denotes the s orbital admixture. The hybridization is strongest at $(\pi, 0)$ and $(0, \pi)$. The filling is fixed to $\langle n \rangle = 0.84$ per site. Right: The same for smaller $\Delta E_{sd} = 6eV$.

shape as the Fermi surfaces observed in high- T_c cuprates. In figure 6.1, we show two examples. In these plots, the maximal admixture of the s orbital to the band with Fermi surface is only about 10%, but, below, we will see that already this has a measurable effect on the critical scale.

We include interaction in the form of intraorbital and interorbital repulsions, $U_{s/d} = U$ and U' as well as a Hund's rule coupling J_H and pair-hopping term J_P . We write the interaction Hamiltonian as

$$\begin{aligned}
 H_I = & U \sum_{R,o} n_{o,\uparrow}(R) n_{o,\downarrow}(R) + \frac{U'}{2} \sum_{\substack{R,\sigma,\sigma', \\ \sigma \neq \sigma'}} n_{o,\sigma}(R) n_{o',\sigma'}(R) \\
 & + \frac{J_H}{2} \sum_{\substack{R,o \neq o', \\ \sigma,\sigma'}} c_{o,\sigma}^\dagger(R) c_{o',\sigma'}^\dagger(R) c_{o,\sigma'}(R) c_{o',\sigma}(R)
 \end{aligned}$$

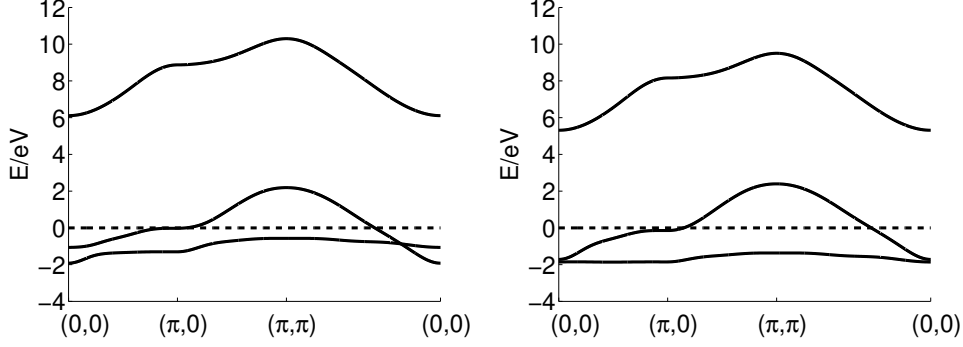


Figure 6.2: Left: band-structure of the three-band model with s -, $d_{x^2-y^2}$ - and d_{z^2} -like orbitals, with parameters corresponding to La_2CuO_4 . Right: same band-structure for larger $\Delta E = t_{0,0}^d - t_{0,0}^z$ but same $t_{0,0}^s - t_{0,0}^z$, roughly corresponding to $\text{HgBa}_2\text{CuO}_4$ according to Wien2Wannier [Kun10; Mos08; Bla01]. Filling: $\langle n \rangle = 2.84$.

$$+ \frac{J_P}{2} \sum_{\substack{R, o \neq o', \\ \sigma, \sigma'}} c_{o,\sigma}^\dagger(R) c_{o,\sigma'}^\dagger(R) c_{o',\sigma'}(R) c_{o,\sigma}(R). \quad (6.3)$$

Here R and $o, o' = \{s, d\}$ denote the lattice sites and orbitals respectively and $n_{o,\sigma}(R) = c_{o,\sigma}^\dagger(R) c_{o,\sigma}(R)$.

Below we will also study a three-band model, which now also contains an orbital below the Fermi level, with the symmetry of a d_{z^2} -like orbital as in [Sak10]. For this model, we use parameters obtained with the Wien2Wannier scheme [Kun10].¹ We drop all hoppings in the third direction, in order to keep the model two dimensional. The free part of the Hamiltonian is then given by

$$H = \sum_{k,\sigma} \begin{pmatrix} c_{s,\sigma}^\dagger(k) \\ c_{d,\sigma}^\dagger(k) \\ c_{z,\sigma}^\dagger(k) \end{pmatrix}^T \begin{pmatrix} \epsilon_s(k) & h_{sd}(k) & h_{sz}(k) \\ h_{sd}(k) & \epsilon_d(k) & h_{dz}(k) \\ h_{sz}(k) & h_{dz}(k) & \epsilon_z(k) \end{pmatrix} \begin{pmatrix} c_{s,\sigma}(k) \\ c_{d,\sigma}(k) \\ c_{z,\sigma}(k) \end{pmatrix}, \quad (6.4)$$

with the diagonal terms

$$\epsilon_o(k) = \sum_{m_x, m_y} t_{m_x, m_y}^o e^{i(m_x k_x + m_y k_y)} - \mu, \quad (6.5)$$

and the hybridization terms

$$h_{o_1, o_2}(k) = \sum_{m_x, m_y} t_{m_x, m_y}^{o_1, o_2} e^{i(m_x k_x + m_y k_y)}, \quad (6.6)$$

¹ *Wannier90* is introduced in [Mos08] and for *WIEN2k* see [Bla01]. The parameters were provided by Ryotaro Arita.

where the coefficients t_{m_x, m_y}^o and $t_{m_x, m_y}^{o_1, o_2}$, with o, o_1, o_2 denoting the respective orbitals, are the parameters derived from the ab initio calculation [Kun10; Mos08; Bla01]. The indices s, d , and z are used to label the $s, d_{x^2-y^2}$, and d_{z^2} orbitals respectively, to shorten the notation. We include hoppings between sites on the two-dimensional square lattice with a maximum distance of five lattice constants in each lattice direction, that is the sum in equations (6.5, 6.6) runs over all integer values m_x, m_y from -5 to $+5$.

The resulting band-structures are plotted in figure 6.2. Now, we have one s -dominated band above the Fermi level and one d_{z^2} -dominated band below the Fermi level. The band at the Fermi level is primarily of $d_{x^2-y^2}$ -character.

Again, we use interactions of intraorbital, interorbital, Hund's rule and pair hopping type according to equation (6.3), where now the sums o and o' go over all three orbitals $o = \{s, d, z\}$. In order to keep the analysis simple, we refrain from using orbital-dependent interaction parameters.

6.3 Functional Renormalization Group Treatment

We will apply the fRG method detailed in chapter 2, to analyze the effect of the inclusion of the bands which do not touch the Fermi surface, on the emergence of the d-wave pairing instability. We will neglect the flow of the self-energy and three-particle vertex and the frequency dependence as before.

For the parameter values, which are relevant for the actual electronic structure of the cuprates, the $d_{x^2-y^2}$ -like band has a Fermi surface and the other s -like and d_{z^2} -like bands are energetically separated from the Fermi surface. Then, if we are interested in the interaction effects at low temperatures and set up a perturbation expansion in the bare interactions, we can expect that virtual excitations into the bands away from the Fermi level only play a smaller role, as they generally lead to larger energy denominators in the corresponding diagrams. For this reason, we will only take into account the $d_{x^2-y^2}$ -dominated band, when solving the flow equations, i.e. the coupling function is now only wavevector-dependent and the band index is dropped, as we restrict to the vertices in the conduction band. In this approximation, the influence from the multiband character of the model enters only via the orbital admixture of the bare interaction vertex, due to the orbital-to-band transformation, written in equation (2.29), that makes the bare interactions projected onto the conduction band wavevector-dependent. The integration of the fRG equation then takes into account all one-loop corrections with both internal lines in the low-energy window and thereby reconstructs the most important parts from the perturbation expansion of the band near the Fermi level. For the integration in momentum space we employ the N-patch scheme described in section 2.6 with 64 patches. The patching points, at which the coupling function is calculated, are set on the Fermi surface, as in previous fRG studies (e.g. [Hon01; HS01]).

The orbital content is the new aspect in comparison with one-band models.

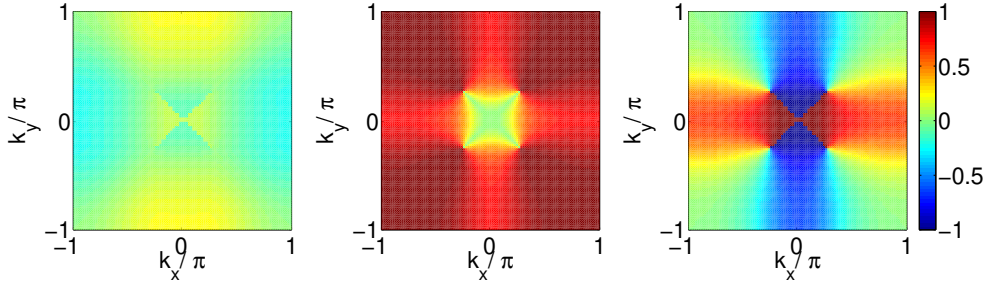


Figure 6.3: Admixture of the three orbitals to the $d_{x^2-y^2}$ -dominated band with the Fermi surface, the orbitals s , $d_{x^2-y^2}$, d_{z^2} are shown from right to left in that order, respectively. Shown are the three elements of the transformation $u_{c,o}(k)$ in equation (2.29) with c denoting the $d_{x^2-y^2}$ -dominated conduction band and $o \in \{d, z, s\}$.

In context with unconventional superconductivity, this raises interesting questions, in particular, whether the bare interaction already contains an attractive component in some symmetry channel, or if the generation of such an attraction (that in one-band models is usually accomplished by particle-hole fluctuations) is somehow influenced by this extra structure. In section 6.5 on the two-patch model, we will give more details on which interaction processes are increased by this and which are reduced. We will see that under quite general conditions, the orbital content does not help d -wave superconductivity.

As pointed out in section 2.7, there is some freedom of choice in the transformation of the orbital-to-band transformation. In the present case, the leading contribution to the conduction band comes from the $d_{x^2-y^2}$ orbital. We, therefore, choose the prefactor of the eigenvector corresponding to the conduction band such that the matrix element of the transformation $u_{c,d}(k)$ does not have a sign change on the path along the Fermi surface, where the subscript c stands for the $d_{x^2-y^2}$ -dominated conduction band. This leads to the transformation shown in figure 6.3. With this choice, the interaction vertex in the three-band model transitions continuously to the values of the one-band model, if the additional orbitals are shifted far away from the Fermi level. That is, e.g. for the case of an on-site repulsion only, the bare interaction is constant and in particular positive for all momenta. We made the same choice for the two band model in figure 6.1, as well as in its two-band version in section 6.4 and 6.5. Due to the symmetry of the included orbitals, sign changes of the orbital admixture of the d_{z^2} and s orbitals occur on the Brillouin zone diagonal.

Let us now discuss the first step to include virtual processes into these bands, i.e. inter-band transition. If we write a perturbation series for the full two- or three-orbital model, and compare the various one-loop terms entering there to what we get in the fRG for the conduction band, we find that the next important terms that are not included in the fRG treatment are diagrams with at least

one internal line in one of the bands away from the Fermi surface. While these diagrams will not become singular as their energy denominator will never go to zero, they might induce additional wavevector dependencies to the interactions, that might be measurable for the unconventional pairing studied here. Actually, the cRPA formalism sums up a part of these contributions to infinite order, which results in an additional screening of the Coulomb interaction [Ary04; Ary06]. Including these effects more systematically into the fRG for a single band, is a separate issue that we do not touch here. Instead, we will study the impact of an additional second-order correction due to these virtual processes with one and also two internal lines away from the conduction band, whereas the contribution of the latter is confirmed to be comparably small. This correction, which we will refer to as high-energy second-order correction, is added to the initial condition of the flow in the conduction band. It is given by all one-loop diagrams (particle-particle and particle-hole) with bare interactions at the vertices and at least one internal line in a band above or below the conduction band. We will see that it has a definite impact for smaller energy gaps between the bands. Due to the energetic separation of the bands away from the Fermi surface, we expect that this second-order treatment is already quite good, and that the higher-order corrections neglected here only have a small effect.

The different types of divergences in the flow for the single band Hubbard model as function of the system parameters have been analyzed and classified in a number of previous publications ([Met12] and references therein). In the present case, the fRG flow almost exclusively favors a d -wave pairing instability that is understood to be driven by AFM spin fluctuations. Here, we mainly discuss the critical scale Λ_c of this d -wave instability. This scale can be understood as a measure or upper estimate for the transition temperature T_c into the d -wave superconducting state. It takes an analogous role as the quantity $\hbar\omega_D e^{1/\rho_0 g}$ in a simple BCS problem with Debye frequency ω_D , density of states ρ_0 and attractive interaction g .

6.4 Results for the Two-Band Model

Let us now apply the N -patch fRG scheme to the lower band of the two-band model described in section 6.2. We therefore, fix the hopping parameters of the bands to be $t_d = 0.45eV$, $t_s = 0.5eV$, and the hybridization to $t_{sd} = 0.6eV$. The tuning parameter is the energy separation between the band centers, ΔE_{sd} .

In the plots of figure 6.4 we additionally choose two sets of interaction parameters according to the sum rule $U - U' = 2J_H = 2J_P$ [DHM01]. The density is fixed to 16% hole doping of the lower band, i.e. $\langle n \rangle = 0.84$ per site. In the left plot, the critical scale for the d -wave pairing instability, Λ_c , in dependence of the energy difference ΔE_{sd} of the two orbitals is shown. The direction of the horizontal axis is inverted so that the plots can be compared better with the ones for the three-band model in section 6.6. We can see that moving the

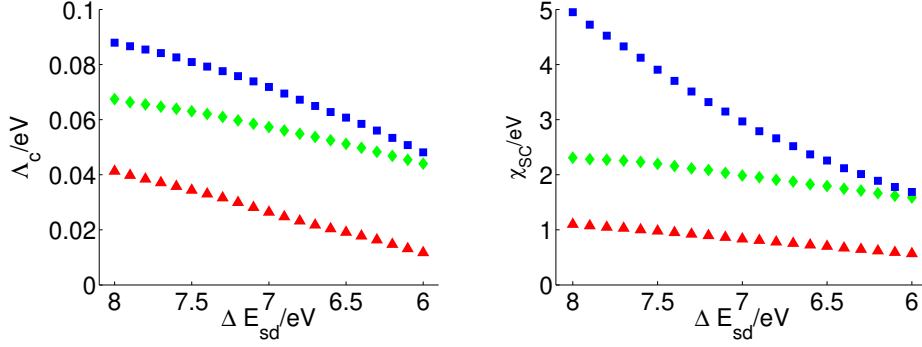


Figure 6.4: Critical scale (left) and superconducting susceptibility at a fixed scale $0.09eV$ (right) vs ΔE_{sd} , computed with 64 patches on the Fermi surface. Red triangles: with orbital mixing, green diamonds: orbital mixing cut out by hand, $U = 1.8eV$, $U' = 1.44eV$, $J_H = J_P = 0.18eV$. Blue squares: with larger interactions $U = 2.2eV$, $U' = 1.76eV$, $J_H = J_P = 0.22eV$, with orbital mixing. Parameters: $t_d = 0.45eV$, $t_s = 0.5eV$, $t_{sd} = 0.6eV$, $\langle n \rangle = 0.84$.

two bands closer to each other, i.e., reducing ΔE_{sd} , decreases the critical scale Λ_c . This behavior is robust with respect to the interaction strength. We also plot Λ_c vs ΔE_{sd} when the orbital content is ignored and the bare interaction is simply U for all wavevector combinations. In this case, Λ_c is higher. This allows us to distinguish the effect of the orbital content from that of the Fermi surface shape, which also changes as a function of the energy separation ΔE_{sd} . Here, we only calculated data for the parameter set with smaller interaction, as the one-loop approximation is not justified, if the interaction is too large. With included orbital mixing however the average of the coupling function at the beginning of the flow is below half of the bandwidth. Summarizing our findings, we can state that the expected decrease of Λ_c with the Fermi surface becoming rounder when ΔE_{sd} becomes smaller is not compensated by the orbital content or stronger hybridization in the $d_{x^2-y^2}$ -band. Rather, this latter effect leads to an additional reduction of the pairing scale.

We also plot in figure 6.4 the effective strength of the d -wave superconducting channel at a small fixed $\Lambda > \Lambda_c(\Delta E_{sd})$, which is defined as

$$\chi_{sc} = \frac{1}{N^2} \sum_{k,p} V^\Lambda(k, -k, p) f(k) f(p). \quad (6.7)$$

Here, the sums run over all N patches of our patching scheme and $f(k)$ and $f(p)$ are d -wave form factors and are given by $f(k) = \cos(k_x) - \cos(k_y)$, and $V^\Lambda(k, -k, p)$ is the running interaction at the small fixed scale. This measure of the strength of the superconducting channel gives a qualitatively similar picture. Again, both factors, Fermi surface deformation and orbital makeup,

reduce the tendency toward d -wave pairing.

In this sense, a well separated $d_{x^2-y^2}$ -like band appears to be the optimal situation for a high critical scale or high T_c . The two-band model with the s orbital above the $d_{x^2-y^2}$ orbital can not give an explanation why the cuprates with rounder Fermi surface have higher T_c , as indicated by the DFT trends. Our data clearly show that the perturbation of the dispersion, as well as the orbital content, reduce the critical scale.

In order to understand this finding more directly, and to see how general it is, we will now turn to a simplified description in terms of the two-patch model.

6.5 Simplified Picture: Two-Patch Model

Let us consider again the situation where only the lower $d_{x^2-y^2}$ -like band has a Fermi surface, and let this Fermi surface be near the van Hove points at $A = (\pi, 0)$ and $B = (0, \pi)$. Then a common approximation is the so-called two-patch model [Sch87; FRS98], where only the fermionic degrees of freedom in small circles around these van Hove points are considered, and the interactions between these regions are approximated by four constants g_1 to g_4 [Hon01]. These are defined by

$$g_1 = V(A, B, B, A) = V(B, A, A, B) , \quad (6.8)$$

$$g_2 = V(A, B, A, B) = V(B, A, B, A) , \quad (6.9)$$

$$g_3 = V(A, A, B, B) = V(B, B, A, A) , \quad (6.10)$$

$$g_4 = V(A, A, A, A) = V(B, B, B, B) , \quad (6.11)$$

where, again, the first two entries k_1 and k_2 of $V(k_1, k_2, k_3, k_4)$ are the incoming wavevectors, and that the first incoming particle with k_1 and the first outgoing with k_3 have the same spin projection σ , while the second incoming k_2 and the second outgoing k_4 have σ' . Such a modeling has been used to explore the basic phase diagram of the two-dimensional single band t - t' Hubbard model near van Hove filling. There, the initial value for the g_i from the bare interaction is just U . A very similar model has been used for the study of the iron arsenide superconductors [CEE08].

We shortly recapitulate some results of the two-patch study of the Hubbard model in [FRS98], following [Hon01]. The fRG treatment of the two-patch model, where only the singular one-loop contributions of the particle-particle loop with zero incoming momentum and the particle-hole loop with momentum transfer (π, π) are kept, leads to the flow equations [FRS98]

$$\dot{g}_1 = 2\dot{d}_1 g_1 (g_2 - g_1) , \quad (6.12)$$

$$\dot{g}_2 = \dot{d}_1 (g_2^2 + g_3^2) , \quad (6.13)$$

$$\dot{g}_3 = -2\dot{d}_0 g_3 g_4 + 2\dot{d}_1 g_3 (2g_2 - g_1) , \quad (6.14)$$

$$\dot{g}_4 = -\dot{d}_0(g_3^2 + g_4^2), \quad (6.15)$$

with $\dot{d}_0, \dot{d}_1 > 0$ as scale derivatives of the particle-particle and particle-hole loop, respectively. Possible instabilities in the d -wave pairing, AFM SDW, and CDW channel are then associated with the unbounded growth of the combinations $g_3 - g_4$, $g_2 + g_3$ and $-2g_1 + g_2 - g_3$, respectively. In the one-band Hubbard model for $d_0 = d_1$, corresponding to perfect nesting, the coupling constants diverge as $g_{2,3} \rightarrow \infty$, $g_4 \rightarrow -\infty$, g_1 diverges more slowly. As long as g_4 is positive, the two terms on the right hand side of equation (6.14) have opposite sign and give competing contributions, but eventually g_4 becomes negative and both terms in equation (6.14) drive the flow to strong coupling (cf. [Hon01]). Then the d -wave pairing $g_3 - g_4$ diverges, but usually, for non-zero U , the SDW combination $g_2 + g_3$ has grown much larger. Hence, the instability for $d_1 = d_0$ is of multichannel [Hon10] type, with the SDW tendencies being strongest. For $d_1 < d_0$, corresponding to non-zero t' , the SDW channel is less dominating and one gets a regime where the d -wave coupling $g_3 - g_4$ diverges more strongly. This is what we call the d -wave pairing regime. More details are given in [FRS98].

For the single band model, the comparison with the fRG calculations taking into account the full wavevector dependence of the interactions around the Fermi surface showed that most trends can already be inferred from the two-patch model, so that the latter should serve as a good starting point to study the main effects.

We will now use the two-patch model to assess the impact of the orbital content on the type and energy scale of the instability of the weakly-coupled state due to the interactions. At the van Hove points, the transformation that diagonalizes the hopping Hamiltonian of the two-band model can be expressed as

$$u_{c,d}(A) = \cos \phi, \quad u_{c,d}(B) = \cos \phi, \quad (6.16)$$

$$u_{c,s}(A) = -\sin \phi, \quad u_{c,s}(B) = \sin \phi, \quad (6.17)$$

where $u_{c,s}$ and $u_{c,d}$ are the orbital weights of s and $d_{x^2-y^2}$ orbitals in the conduction band c , which is the one with the Fermi surface near the van Hove points. The angle ϕ is a measure for the strength of the orbital mixing and can be understood as the angle between the vertical and the arrow at the van Hove points in figure 6.1. In the case of $\phi = 0$, the mixing is zero and we recover the pure one band model without mixing effects. The sign change of the s admixture in $u_{c,s}(B)$ compared to $u_{c,s}(A)$ comes from the different in-plane symmetry of the $d_{x^2-y^2}$ orbital. It is crucial for the following. Note that this sign change would also occur for any other orbital that is admixed to the $d_{x^2-y^2}$ orbital that transforms trivially under 90 degree rotation in the plane, i.e. also for d_{z^2} or p_z orbitals. Hence, qualitatively, the results hold more generally for a wider class of admixed orbitals.

Next, we consider here only local intra- and interorbital repulsion U and U'

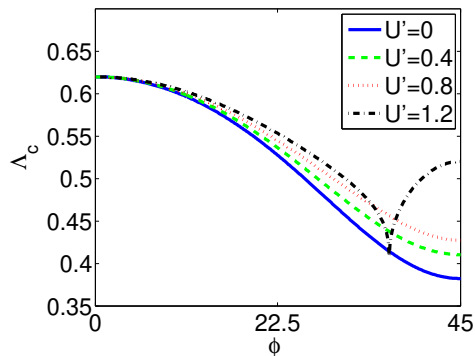


Figure 6.5: Critical scale of the two-patch model as a function of the mixing parameter ϕ in degrees for $U = 1$ and different U' . For most parameters, the instability is of AFM SDW or d -wave pairing type, and the critical scale decreases with larger admixture ϕ . Only for $U' > U$ and ϕ large enough, the instability turns into a CDW instability, and the critical scale is increased by further increasing ϕ (black dashed dotted curve).

to keep it simple. Hund's couplings and pair hopping terms in a realistic range are smaller than these parameters, and should not lead to qualitative differences in the results. For the intraorbital interaction, the orbital content gives a factor $\cos^4 \phi$, while for the interorbital interaction U' the two incoming and the two outgoing particles are in different orbitals, contributing $\pm 2 \sin^2 \phi \cos^2 \phi$. The sign now depends on whether the particle in the s orbital remains in the same patch, say A , or whether it gets scattered to the other patch, say from A to B . In total, we obtain for the initial values of the four coupling constants:

$$g_{1,3} = U \left(\cos^4 \phi + \sin^4 \phi \right) - 2U' \cos^2 \phi \sin^2 \phi, \quad (6.18)$$

$$g_{2,4} = U \left(\cos^4 \phi + \sin^4 \phi \right) + 2U' \cos^2 \phi \sin^2 \phi. \quad (6.19)$$

We see that the orbital content $\phi \neq 0$ in this $d_{x^2-y^2}$ -case quite generally suppresses the bare interaction strength. For a non-zero value of $U' > 0$, this suppression is stronger for $g_{1,3}$ and weaker for $g_{2,4}$. Generally, a larger g_2 and g_3 would lead to a higher critical scale for d -wave pairing, as these couplings drive the AFM fluctuations that form the pairing glue. More repulsive g_1 and g_4 leads to a smaller critical scale. For the desired d -wave pairing instability, the relative enhancement of g_4 with respect to g_3 for $\phi \neq 0$ is exactly the wrong way. It corresponds to an additional repulsion in the d -wave pairing channel and reduces the critical scale.

We have performed a numerical analysis of the flow equations (6.12 – 6.15), in order to investigate the influence of the mixing on the critical scale. Figure 6.5 shows the critical scale obtained for the two-patch model for different U' .

It turns out that the critical scale is suppressed by mixing as long as U' does not get too large. Only for $U' > U$, we encounter the CDW instability and here the s admixture $\phi \rightarrow \pi/2$ can actually increase the critical scale in a certain range. Here, the initial value of g_3 becomes negative and thus g_3 flows to $-\infty$, as the second term of the right hand side of equation (6.14) is negative and the first term eventually becomes negative when $g_4 < 0$. In this numerical treatment, we assumed that the relevant loops d_0 and d_1 have the same value during the flow, which should be an acceptable assumption for these qualitative conclusions. However, we checked that the qualitative results do not depend on the individual behavior of the loops during the flow.

Thus, we conclude that already the simple two-patch model can give us a simple explanation how orbital mixing effects lower the critical temperature of a d -wave superconducting instability.

6.6 Results for the Three-Band Model

So far, we have seen that admixing a single orbital to the $d_{x^2-y^2}$ -derived band leads to a reduction of the critical scale for d -wave pairing. This causes problems to understand the mentioned apparent material trend in the copper based high- T_c superconductors that lowering an axial orbital in energy from above results in higher critical temperatures. Here, we will show that this trend can be recovered, if additional orbitals are considered. To this end, we now consider a two-dimensional three-band model, which includes the $d_{x^2-y^2}$, d_{z^2} , and s orbitals. The Hamiltonian of this model is given in equation (6.4).

To find out whether the mentioned material trend can be explained by mixing effects, we study the critical scale for d -wave pairing with different values for the on-site kinetic energy of the d_{z^2} and s orbitals. We follow the path through the parameter space proposed by Sakakibara et al. [Sak10]. More precisely, we increase $\Delta E = t_{0,0}^d - t_{0,0}^z$ by hand but leaving the difference between d_{z^2} and s orbital constant. This is motivated by the observation that in the cuprate $\text{HgBa}_2\text{CuO}_4$ with $T_c \approx 90\text{K}$ both the d_{z^2} and s orbital are lowered with respect to the $d_{x^2-y^2}$ orbital, compared to La_2CuO_4 with lower $T_c \approx 30\text{K}$ (see also [Sak10]). $\text{HgBa}_2\text{CuO}_4$ has a higher T_c and a more rounded Fermi surface than La_2CuO_4 . As the change in ΔE appears to be the most striking effect, we do not consider a variation of other hopping parameters to keep our analysis simple. Note that a larger $\Delta E = t_{0,0}^d - t_{0,0}^z$ thus corresponds to a smaller ΔE_{sd} of section 6.4, which is written as $\Delta E_{sd} = t_{0,0}^s - t_{0,0}^d$ in terms of the three-band model in equations (6.4 – 6.6). All calculations presented in this section are done at 16% hole doping, that is, $\langle n \rangle = 2.84$ per site.

The left plot of figure 6.6 shows the Fermi surface of our model for the two situations. While the s orbital lowers the energy of the van Hove point, the d_{z^2} orbital has the opposite effect, because it lies below the $d_{x^2-y^2}$ orbital. Thus, the combined effect of the s and d_{z^2} orbitals can lead to a roughly square-like

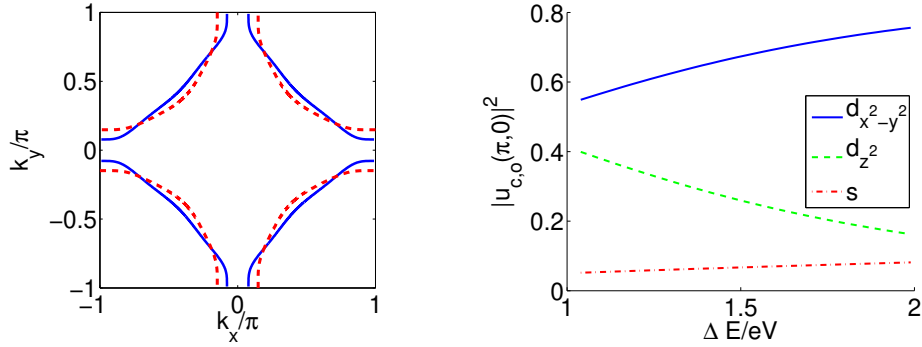


Figure 6.6: Left: shape of the Fermi surface for parameters corresponding to La_2CuO_4 (blue solid line) and for $\Delta E \approx 2\text{eV}$ (red dashed line), corresponding to $\text{HgBa}_2\text{CuO}_4$, $\langle n \rangle = 2.84$. Right: admixture of the three orbitals to the $d_{x^2-y^2}$ -dominated band with the Fermi surface, the orbitals $d_{x^2-y^2}$, d_{z^2} and s are shown as a blue solid, green dashed, and red dotted lines, respectively.

Fermi surface, as it would be without mixing at all. The plot on the right shows the relative orbital admixture at the van Hove point for different ΔE . $|u_{c,o}(\pi,0)|^2$ is the squared absolute value of the coefficients in the orbital-band transformation given in equation (2.29), where the index c as above denotes the $d_{x^2-y^2}$ -dominated conduction band. This quantity serves as a measure for the orbital admixture. The contributions from the three orbitals add up to one due to the unitarity of the transformation.

With larger ΔE , the Fermi surface becomes more rounded, due to a larger perturbation from the s orbital and a smaller influence from the d_{z^2} orbital. The total mixing, i.e., the non- $d_{x^2-y^2}$ -content, is weakened with larger ΔE . This mainly comes from the decreasing influence of the d_{z^2} orbital when it moves down in energy. On the other hand, the s orbital gets closer to the $d_{x^2-y^2}$ orbital with larger ΔE and, thus, increases the mixing. This effect, however, is much smaller due to the larger gap between $d_{x^2-y^2}$ - and s orbitals, and because the s band is rather wide. We conclude that the lowering of ΔE leads to two competing effects on the critical scale. First, the Fermi surface gets more rounded, which, according to the results in one-band models, decreases the critical scale. Second, and this is now different from the two-orbital case, the orbital mixing is reduced, and the $d_{x^2-y^2}$ character increases. As we have seen in the previous section, this favors an enhancement of the critical scale.

In figure 6.7, the critical scale, obtained from the fRG calculation, is shown. Here, the interaction parameters are chosen to be $U = 2.2\text{eV}$, $J_H = U_P = 0.1U$, and $U' = 0.8U$. With the interaction parameters chosen here, the average coupling constant at the beginning of the flow is below half of the bandwidth. Both approximations, with and without high-energy second order correction, show the same qualitative trend. The two competing effects now induce a

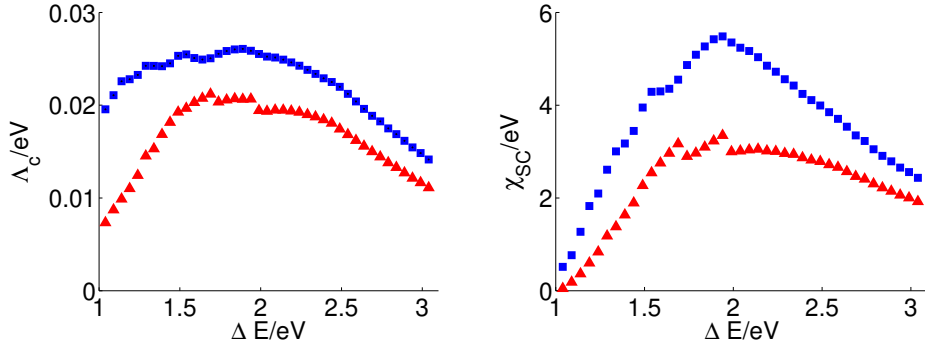


Figure 6.7: FRG data for the three-band model with interaction parameters $U = 2.2eV$, $U' = 1.76eV$, $J_H = J_P = 0.22eV$ computed with 64 patches, $\langle n \rangle = 2.84$. Left: critical scale Λ_c vs $\Delta E = t_{0,0}^d - t_{0,0}^z$. Right: average d -wave pairing at a fixed scale $\Lambda = 0.027eV$ vs ΔE ; without high-energy second-order correction (blue squares), with high-energy second-order correction (red triangles), explained in section 6.3.

maximum in the critical scale and χ_{SC} at some ΔE^* . For larger $\Delta E > \Delta E^*$ the reduced orbital mixing of the vertices cannot compensate the change of the Fermi surface. To separate the effect of the orbital mixing on the interaction and the dispersion, we run the same fRG flow, but now starting with a simple on-site repulsion regardless of the orbital mixing. In other words, we cut out the mixing effect on the vertices by hand. As expected from the results of the two-patch model the critical scale without the orbital content is indeed drastically increased and we do not get an enhancement of the critical scale with increasing ΔE , because now only the Fermi surface effect of the shift comes into play.

Additionally, we run the fRG flow again, but now shift only the s or the d_{z^2} orbital respectively, to see if the interpretation suggested from the two-patch-model holds. As expected, if we only lower the s orbital, the critical scale decreases, since the mixing of the d_{z^2} orbital is not reduced and the positive effect on the critical scale is not present. If we, on the other hand, lower only the d_{z^2} orbital, but keep the s orbital constant, the qualitative picture from figure 6.7 is recovered.

The value ΔE^* with highest critical scale depends on the strength of the interactions. For smaller bare values, the Fermi surface shape is more important, and ΔE^* shifts to smaller values and even disappears. In figure 6.8, we again show critical scale and d -wave pairing strength vs ΔE as in figure 6.7, but now for reduced on-site interaction $U = 2eV$, while the other interaction parameters are reduced accordingly, so that the ratio to the on-site interaction remains constant. Now, without second-order correction of the additional orbitals, the critical scale decreases over the entire range. Our data quite generally suggests

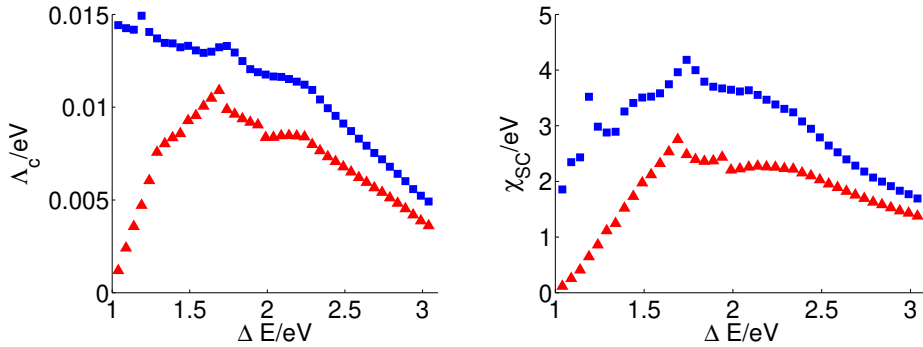


Figure 6.8: FRG data for the three-band model with interaction parameters $U = 2.0eV$, $U' = 1.6eV$, $J_H = J_P = 0.2eV$ computed with 64 patches, $\langle n \rangle = 2.84$. Left: critical scale Λ_c vs $\Delta E = t_{0,0}^d - t_{0,0}^z$. Right: average d -wave pairing at a fixed scale $\Lambda = 0.015eV$ vs ΔE ; without high-energy second-order correction (blue squares), with high-energy second-order correction (red triangles), explained in section 6.3. The steps in the data are due to the discretization of the wavevector dependence of the coupling function.

that at least without high-energy corrections the effect of an enhancement of the critical scale with larger ΔE is less pronounced, when the critical scale is lower, that is for smaller interaction strength or, e.g., larger J_H , which usually suppresses the flow to strong coupling. Turning this observation around, we can argue that the enhancement effect might even be larger, if we used realistic interaction values for the cuprates. We refrain from running the fRG flow with such large interaction parameters, as the one-loop approximation of the fRG equation is then no longer justified.

It can be seen that the inclusion of the high-energy vertices within second-order perturbation can have a profound effect on the critical scale. Especially, for smaller interaction strength, the instability is strongly suppressed at small ΔE , so that, in contrast to the case without high-energy correction, even at smaller interaction strength, a maximum in the critical scale can be found. It seems worthwhile to study the renormalization of the vertices due to higher energy modes, in more detail. This may be an additional contribution to the observed material trends, as the curves with included high-energy corrections exhibit a stronger increase in the critical scale than the ones without.

We can compare our findings and our idea, why this T_c -trend occurs, with the FLEX two-orbital and three-orbital calculations by Sakakibara et al. [Sak10]. Although their Eliashberg eigenvalues cannot be compared directly to the fRG critical scales, it seems that we can qualitatively reproduce their results. Clearly, at least for their two-band calculation, the orbital admixture to the conduction band is certainly lower for the higher T_c 's with the rounder surfaces, supporting

the conclusion, that orbital mixing reduces T_c . Quantitatively, our results are sensible to the interaction strength and a direct comparison would require data at larger on-site interaction of $3eV$, as used for the FLEX calculation. As the bandwidth of the conduction band is only $\approx 4eV$, we refrain from running the fRG for such large interactions. Also, we expect that self-energy effects, which were included by Sakakibara et al., but not in our work, will probably still cause a noticeable quantitative difference.

Within this downfolded three-band electronic structure, $\text{HgBa}_2\text{CuO}_4$ with T_c of 90K would roughly correspond to $\Delta E = 2eV$ [Sak10], close to where the maximal critical scale occurs in figure 6.7. While this is promising, we note that the band-structure change from La_2CuO_4 to $\text{HgBa}_2\text{CuO}_4$ may be more complex, and taking into account these additional changes may affect the observed enhancement as well. In any case, on a quantitative level and possibly different from Ref. [Sak10], our weak-coupling fRG studies cannot be expected to explain the experimental trend, because the real cuprates are more strongly interacting. We propose that strong-coupling methods should be used to find out whether the picture drawn here works the same (and quantitatively better) at strong coupling. Nevertheless, we have identified ΔE as an important tuning parameter.

The model with the La_2CuO_4 -like band-structure parameters has a nested Fermi surface. Consequently, aside from the superconducting instability, we observe a strong tendency toward long-range AFM order. With larger ΔE , the nesting of the Fermi surface becomes poorer, so that the AFM tendency is more and more suppressed. To have a closer look on the two competing instabilities, we compare the effective strengths of the respective channels. The d -wave superconducting channel can be measured by χ_{SC} given in equation (6.7). Similarly, the AFM channel is

$$\chi_{\text{AFM}} = \frac{1}{N} \sum_k V^\Lambda(k, k_2 \approx (\pi, 0), k_3 \approx (0, \pi)) , \quad (6.20)$$

where k_2 and k_3 are chosen so that they lie close to the two van Hove points and the corresponding momentum transfer is $k_2 - k_3 \approx (\pi, \pi)$. The corresponding ordering susceptibilities diverge if these averaged strengths of the channels diverge. Thus, the defined quantities can be regarded as a measure for the strength of the respective instabilities. The left plots of figures 6.7 and 6.8 show that the superconducting channel has, as expected, a similar behavior as the critical scale as function of ΔE . However, at $U = 2eV$ a qualitative difference arises in the effective strength of the superconducting channel in comparison with the critical scale (see figure 6.8). The effective strength still exhibits a maximum, although it is not as distinct as for larger interactions.

We also compare the relative strength of the channels for different ΔE in figure 6.9. For small ΔE in the left plot the AFM tendency is larger than the d -wave pairing strength, and both averages grow with similar exponent. As

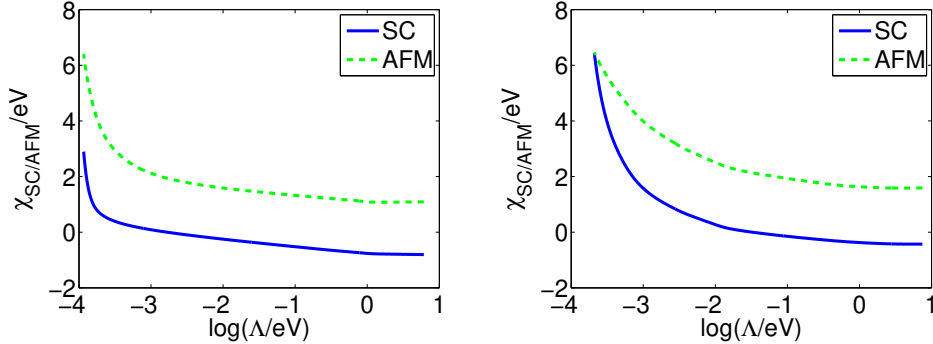


Figure 6.9: Flow of the AFM (green dashed line) and superconducting (blue solid line) interaction strengths for the La_2CuO_4 -like band-structure (left) and for the $\text{HgBa}_2\text{CuO}_4$ -like band-structure with $\Delta E \approx 2\text{eV}$ (right) for the same parameters as in figure 6.7. In the first case, both channels compete, while in the second case, the d -wave pairing channel clearly dominates at low scales.

ΔE becomes larger, the AFM tendency is weakened due to poorer nesting of the Fermi surface. Then, the superconducting channel is leading at low enough scales.

Usually, the critical scale Λ_c is regarded as an upper estimate for actual transition temperatures into ordered states. Regarding the question what the true superconducting transition temperatures might be in the two situations compared here, it is now very likely that, in the case of strong competition between two channels, the transition temperature will actually be significantly reduced compared to Λ_c , while for the cleaner pairing instability in the non-nested situation, T_c might be closer to Λ_c . We expect that an inclusion of the self-energy, which is not considered in this work, would capture this effect. Thus, the true superconducting transition temperatures at small ΔE , would be even smaller, and consequently increasing ΔE should increase the superconducting channel even more than in our calculation.

Summarizing these observations, we state that the multiorbital model with orbital energy variations in accordance with actual material differences, is able to reproduce to some degree the phenomenological tendency that critical temperatures can grow although the Fermi surface gets more rounded. This trend cannot be understood within the framework of one-band models. At least on a qualitative level, we have shown that the orbital mixing provides a mechanism for a T_c enhancement at weak to moderate interactions and confirmed the trend found in [Sak10]. If this mechanism still works at the realistic interaction strength, it could, at least in part, be responsible for observed material trend for the T_c 's of the high T_c cuprates.

6.7 Conclusion

We have studied two-orbital and three-orbital models on the two-dimensional square lattice that mimic the low-lying electronic structure of the high- T_c cuprates. We have computed the critical scale for d -wave pairing, which can be used as an estimate for the critical temperature for d -wave superconductivity. In one-band models with simple on-site repulsion, this energy scale is mainly dominated by the Fermi surface shape and decreases when the Fermi surface gets more rounded (see e.g. section 7.4). The material trend for the real high- T_c cuprates, or more precisely, the combination of experimental T_c and electronic structure calculations for a series of cuprates, seems to contradict this trend, as materials with more rounded Fermi surfaces have higher experimental T_c 's [Pav01]. Our goal was to see if orbital admixture to the conduction band reverts the shape-related T_c variation and allows one to understand this material trend.

We have found that for spin-fluctuation-induced d -wave pairing on the square lattice at a higher critical scale, it is best to have an energetically well-separated $d_{x^2-y^2}$ -like band. The admixture of bands with symmetry different from $d_{x^2-y^2}$ from above and below in energy typically reduces the critical scale for pairing compared to the situation without admixture. Reducing the consideration to the two-patch model allowed us to relate the orbital admixture to an additional repulsion in the d -wave channel, which explains the reduction of the d -wave pairing tendencies. In this setup, it can also clearly be seen that admixing orbitals of s , d_{z^2} , or, possibly, p_z character have a similar negative effect, as the sign structure of the admixture is the same.

With the knowledge that a single nearby band disturbs the pairing, we then analyzed situations with more than two bands. Here, a change of the orbital energies with one empty band moving closer toward the Fermi level can still result in a relative enhancement of the superconducting instability scale, consistent with the actual material trend. We have shown that in three-band models for the cuprates, the approach of the wider s band can have a smaller negative effect on T_c than the positive effect of the d_{z^2} band moving further down to lower energies simultaneously. This constitutes a possible path how the d -wave T_c , generated by the spin-fluctuation mechanism, can be increased as a function of the energetic separation of orbitals near the Fermi level, although the Fermi surface of the $d_{x^2-y^2}$ -dominated band gets more rounded. The main reason for this effect is that the T_c -raising reduction in the orbital admixture to the conduction band overcompensates the decrease in T_c , due to the rounder Fermi surface. All this is in agreement with the previous study of Sakakibara et al. [Sak10].

We have seen that choosing DFT-derived band-structure parameters we can qualitatively reproduce experimental trends in T_c differences between La_2CuO_4 and $\text{HgBa}_2\text{CuO}_4$. However, our calculations are only valid in the weak to moderate coupling regime, and if the interaction parameters are chosen to small,

the expected behavior is not rigorously reproduced. On the other hand, we have shown that the T_c enhancement works better for larger interactions. The real cuprates are of course quite strongly correlated, beyond the interaction range where we can apply our method. There, the T_c enhancement might be even more drastic, but based on our weak-coupling study, this is far from proven. Furthermore, the T_c increase may be even stronger than indicated by our numbers already for weaker interactions, as the less rounded Fermi surfaces have a stronger channel competition, which should result in a further lowering of the critical temperature for d -wave pairing. Both these observations suggest that the mechanism considered in this work might be more effective in the actual materials. It should be interesting to look for the same tendency, e.g., with cluster-DMFT techniques. It should also be interesting to quantify the degree of admixture to the $d_{x^2-y^2}$ band through the series of high- T_c cuprates that obeys the proclaimed relation between T_c and the electronic structure, and to see whether the T_c increase is correlated with this.

We have focused on one single aspect that may distinguish different cuprate materials, expressed by the orbital energies in three-orbital effective Hamiltonians. This allowed to obtain some understanding of how the pairing tendencies change. Very likely, there are other model parameters that exert additional influence on the energy scale of superconducting pairing. For example, depending on the hybridization with the surrounding orbitals and the spread of the respective Wannier functions, the interaction parameters might vary. It appears to be an interesting topic to study these additional effects again in isolated form, and to understand their importance. Then, it might be possible to compose a combined picture that might ultimately be used to guide the search for higher transition temperatures.

Chapter 7

Self-Energy Feedback and Frequency-Dependent Interactions

We study the impact of including self-energy feedback and frequency-dependent interactions on fRG flows for the two-dimensional Hubbard model on the square lattice at weak to moderate coupling strength. Previous studies using fRG had ignored these two ingredients to a large extent, and the question is how much the flows to strong coupling analyzed by this method depend on these approximations. Here, we include the imaginary part of the self-energy on the imaginary axis and the frequency-dependence of the running interactions on a frequency mesh of 10 frequencies on the Matsubara axis. We find that i) the critical scales for the flows to strong coupling are shifted downwards by a factor that is usually of order 1 but can get larger in specific parameter regions, and ii) that the leading channel in this flow does not depend strongly on whether self-energies and frequency-dependence is included or not. We also discuss the main features of the self-energies developing during the flows.

This chapter has previously been published in [UH12b].

Contents

7.1	Introduction	107
7.2	Model and Method	109
7.3	Case without Instability	111
7.4	Critical Scales and Leading Instabilities	112
7.5	Flow of the Self-Energy	117
7.6	Discussion	122

7.1 Introduction

In previous chapters, we employed the fRG for the investigation of weakly coupled fermions on two-dimensional lattices. The main object of interest was the flowing interaction vertex, whose strongest components give information on the leading correlations in the effective theory at lower scales. Here, frequency dependence of the vertex and the flow of the self-energy have been neglected, as discussed in section 2.6. This approach is widely used in the literature

(e.g. Refs. [ZS98; ZS00; HM00; Hon01; HS01], and many more works cited in [Met12]) and, therefore, a check of the approximations is of high interest.

Self-energy has been included in a couple of previous works. Either the flow of the self-energy was computed without allowing for a feedback on the flow of the interaction vertex [KK04; RM05], or the self-energy was parametrized using a quasi-particle weight [Zan01; HS03; Kat09]. These studies gave the following information:

1. The fRG flows with neglected self-energy are good approximations in the sense that in typical cases the leading low-energy instabilities are not altered in their existence and character, by including (parts of) the self-energy.
2. A detailed study of the self-energy suggests the occurrence of interesting and observable effects such as anisotropic quasi-particle degradation [Met12], dispersion renormalizations and partial gap openings.

The frequency dependence of the interaction vertex is usually absent in the initial condition of the flow, i.e. the bare electron-electron interaction is not retarded. But during the flow, the subsequent inclusion induces a frequency dependence that can cause at least quantitative effects. Again, the frequency dependence of the vertex has been taken along in a handful of studies [KT06; FHL06; Tam07; HFL07]. The upshot here is again that the previous flows without frequency dependence are not so bad and no drastic changes of the leading instabilities are expected when the approximation is improved.

All these rather qualitative results are encouraging, but, in order to develop the fRG into a quantitative method that is able to describe materials more directly, the approach has to be improved. One group of workers have embarked on this mission using ansatzes for the frequency dependences of vertex functions and self energies [HS09; HGS12]. Here we want to use a more direct approach. We treat the frequency dependence of the self-energy and the interaction vertex by discretizing the Matsubara axis in $N_\omega = 10$ patches, in a similar spirit as the wavevector dependence is patched into $N_k = 32$ patches around the Fermi surface. In this way, the interaction vertex of the one-band model becomes an object with $(N_k \times N_\omega)^3$ components that can still be dealt with numerically. Also, the imaginary part of the self-energy is computed with some resolution, given by N_ω values on the Matsubara axis. This allows us, e.g., to test how adequate it is to use a simple Z -factor in order to describe the flowing self-energy. The self-energy is then fed back into the flow of the interaction vertex by using full Green's functions on the internal lines of the one-loop diagrams in their flow.

The main questions we can ask using this refined scheme are as follows:

1. What is the impact of the self-energy feedback and/or the frequency dependence on the type and energy scale of the leading instabilities? Can we use the critical scales in this approximation as estimates for gap sizes

in the ordered state at lower scales ?

2. What can be learned about the flowing self-energy? How is its frequency and wavevector-dependence for typical situations in the one-band Hubbard model? Is there any non-Fermi-liquid physics that can be deduced from these flows?

7.2 Model and Method

We study the two-dimensional Hubbard model on a square lattice with nearest- and next-nearest-neighbor hoppings t and t' , respectively, and a simple on-site interaction U . The Hamiltonian is given by

$$H = \sum_{k,\sigma} \xi(k) c_\sigma^\dagger(k) c_\sigma(k) + \sum_{r_i} U n_\uparrow(r_i) n_\downarrow(r_i). \quad (7.1)$$

Here $c_\sigma^\dagger(k)$ and $c_\sigma(k)$ are creation and annihilation operators with momentum k and spin $\sigma \in \{\uparrow, \downarrow\}$ and $n_\sigma(r_i) = c_\sigma^\dagger(r_i) c_\sigma(r_i)$ is the density operator at site r_i . The dispersion relation reads as

$$\xi(k) = -2t(\cos k_x + \cos k_y) + 4t' \cos k_x \cos k_y - \mu, \quad (7.2)$$

where μ is the chemical potential and the lattice constant is set to unity.

We employ the fRG formalism detailed in chapter 2. We will disregard contributions from the three-particle vertex as before. However, in this chapter, we will keep the frequency dependence of the vertex and the self-energy feedback in the treatment of the flow equations. Note, that we stick to the expression (2.25) and do not employ the Katanin-modification [Kat04], i.e. the replacement of the single scale propagator $S^\Lambda(p)$ by $\frac{d}{d\Lambda} G^\Lambda(p)$ in equations (2.21 – 2.23), as this would increase the numerical effort very strongly in this two-dimensional problem. We do not expect any qualitative effects of not employing this replacement, as there is no reason why the instabilities should not take place. Comparing our results with the recent study of Giering and Salmhofer [GS12], who can take the Katanin-replacement into account, as they use a simplified parametrization of the vertex, confirms that this point is not crucial to the question at hand.

We divide the Brillouin zone into $N_k = 32$ patches to cover the momentum-dependence of the vertices at the Fermi surface (see figure 7.1), as in previous studies (e.g. [Hon01]). Additionally, we divide the Matsubara axis in N_ω patches and calculate the Matsubara sum numerically. We use two different patching schemes. In the first scheme (D1) the vertices and self-energy are calculated at the 10 Matsubara frequencies with the smallest absolute values. The Matsubara frequencies of the respective patches are thus given by $\omega_p = \{\pm 1, \pm 3, \pm 5, \pm 7, \pm 9\} \times \pi T$. We keep the smallest frequencies as

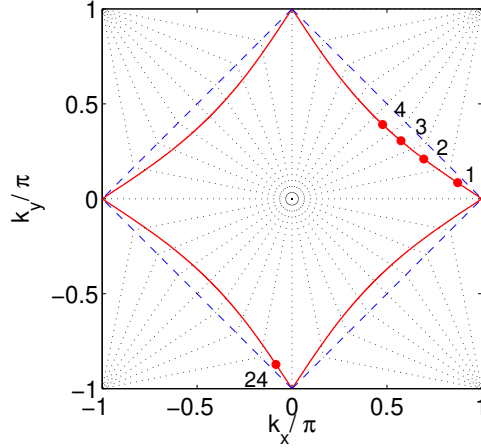


Figure 7.1: N-patch discretization scheme with $N_k = 32$. The Fermi surface with $t' = 0.2t$, $\mu = -4t'$ is plotted in red. The patches are divided by black dotted lines. The red dots denote the momenta, at which the coupling function and self-energy is computed. The umklapp-surface is shown as the blue dashed line. Modified from [HS01].

these are expected to give the leading contributions to the flow [Met12]. Additionally, we consider a patching where the frequencies of the patches are at $\omega_p = \{\pm 1, \pm 3, \pm 5, \pm 11, \pm 21\} \times \pi T$ to cover the dependence at higher frequencies more accurately. This discretization is referred to as D2. In both schemes the vertices and self-energy at all other frequencies occurring in the loops are assumed to have the same value as the closest frequency-patch. This amounts to keeping the frequency-dependence in self-energy and interactions constant above the largest positive or smallest negative discretization frequency.

In the loop diagrams with self-energy inclusion, the Matsubara sums have to be performed numerically. To do this, we truncate the Matsubara sums at some ω_∞ and check whether further increasing this frequency cutoff changes our results. In practice we chose $\omega_\infty = 1500\pi T$, as further increasing the maximum frequency did not lead to major changes in self-energy or critical scales.

In this way, we calculate the vertex and self-energy only for a given set of Matsubara frequencies and momentum vectors on the Fermi surface. The flowing self-energy then appears on the internal lines of the loop diagrams. Importantly, we neglect the real part of the self-energy. This is because a feedback of the real part of the self-energy would lead to a Fermi surface shift which is hard to handle within the N -patch scheme, as the Fermi surface could be shifted into a momentum region which has already been integrated out in previous fRG steps, causing severe singularities in the flow. From previous studies [Hon01; Ueb09] and a recent, similar work by Giering and Salmhofer [GS12], we know, however, that the effects due to the real part are less important.

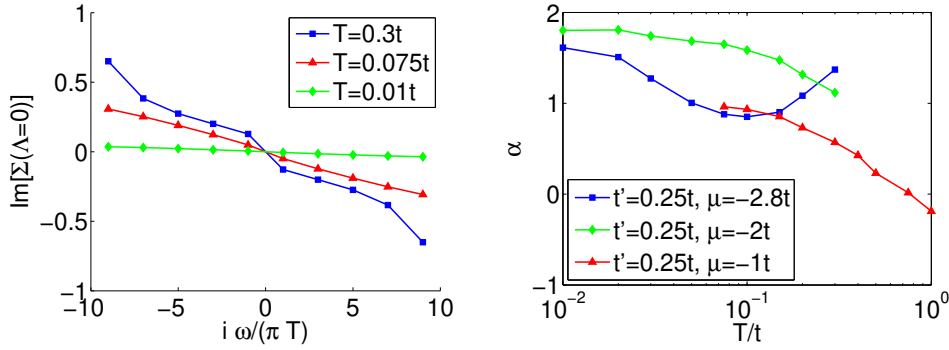


Figure 7.2: Left: Imaginary part of the self-energy in units of t for different $T > T_c$. $t' = 0.25t$, $\mu = -2t$. Shown are the values at momentum $k = 1$ (see figure 7.1). The largest couplings at $\Lambda = 0$ are of the order of $4t$. Right: Estimation for the exponent in equation (7.3) for $t' = 0.25$ at van Hove filling (red triangles) and away from van Hove filling (blue squares, green diamonds), obtained via equations (7.4, 7.5) for $k = 1$ (see figure 7.1). All data for $U = 3t$ with self-energy feedback in the discretization D1.

7.3 Case without Instability

First, as a check in order to get familiar with the data that we obtain from the fRG, let us look at a case, in which the flow indicates normal metallic behavior. For that we choose $t' = 0.25t$ and $\mu = -2t$ such that the Fermi surface is away from the van Hove situation and from the AFM SDW instability. Then, if we stay away from the lowest temperatures, the fRG flow does not lead to strong coupling, i.e. we can integrate out all modes without encountering a strong growth of any components of the coupling function. In figure 7.2, we show the imaginary parts of the self-energy as a function of the Matsubara index for different temperatures. In addition to a decrease of the self-energy toward lower T , we observe a monotonic frequency-dependence that features some kind of downward step around zero frequency. The slope of the overall curve can easily be interpreted as quasi-particle weight or Z -factor, while the step can be understood as a finite lifetime τ .

Note that for higher frequencies of the scale of the bandwidth, the imaginary part of the self-energy should approach zero again, but our frequency window is not large enough to capture this behavior. In our treatment, the self-energy at frequencies outside the discretization window (i.e. for Matsubara indices higher than ± 10) is approximated by the value at the closest discretization frequency. This may underestimate the true self-energy in the frequency range where the linear slope around zero frequency still continues, but may overestimate it at higher frequencies where the imaginary part of the self-energy is a decreasing function of the absolute value of the frequency. To some extent these two effects

will cancel each other, and in any case the large-frequency self-energy is less relevant for the Fermi surface instabilities considered here. Therefore, we think that our simple scheme of treating the self-energy behavior at higher frequencies is qualitatively adequate.

We can analyze the behavior of the quasi-particle lifetime obtained from the step around zero frequency a bit more closely. Let us test if the law

$$\tau^{-1} \sim T^\alpha \quad (7.3)$$

is verified by our data, where we should find $\alpha = 2$ for a Fermi-liquid with a round Fermi surface (e.g. [SCP98]). At van Hove filling, due to the divergence of the density of states, the exponent is expected to be altered to $\alpha = 1$ [LR87]. Note, however, that all these literature values are obtained by finite-order perturbation theory, while the fRG sums up infinite orders in the bare coupling. The fRG estimate for the life-time is obtained by linearly extrapolating the self-energy for the two lowest frequencies to $\omega = 0$

$$\tau^{-1} = \Delta \Sigma^\Lambda = \frac{1}{2} \text{Im}[\Sigma^\Lambda(k_F, 3\pi T)] - \frac{3}{2} \text{Im}[\Sigma^\Lambda(k_F, \pi T)]. \quad (7.4)$$

The expression

$$\alpha_{T_i} = \frac{\Delta(\log(\tau^{-1}))}{\Delta(\log(T))} = \frac{\log(\tau_{T_{i+1}}^{-1}) - \log(\tau_{T_i}^{-1})}{\log(T_{i+1}) - \log(T_i)} \quad (7.5)$$

gives an estimate for the exponent, extracted from data at two temperatures T_i and T_{i+1} . The right plot of figure 7.2 shows the temperature-dependence of α . Although we do not observe a constant α , presumably due to the error of the extrapolation, at least α for the rounded Fermi surface is near the expected value of 2 for low enough temperatures, and similarly, for van Hove filling, α is close to one for low temperatures.

7.4 Critical Scales and Leading Instabilities

Now let us address cases with flows to strong coupling. The first question we want to ask is whether the inclusion of frequency dependence and feedback from the imaginary part of the self-energy leads to a different leading instability or a change in the critical scale. Here, we study this question along the parameter line of van Hove fillings, where the Fermi surface contains the points $(\pi, 0)$ and $(0, \pi)$. These are saddle points of the dispersion and cause a divergence of the density of states. From previous works, it is known that this van Hove situation leads to competing ordering tendencies (e.g. [HS01; HS09]). Hence, this situation is a good arena to study the impact of the inclusion of frequency dependence and self-energy feedback.

First, let us look at the van Hove situation at half-filling, where, in addition,

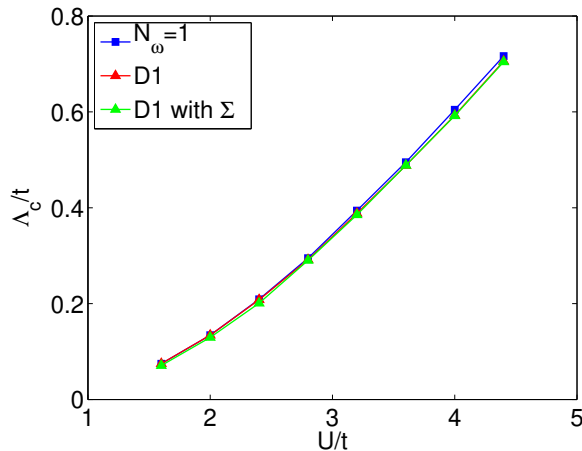


Figure 7.3: Critical scale, at which the couplings exceed $20t$, vs. U for the fully nested case, with $T = 0.01t$, $t' = 0$, and $\mu = 0$ for the flows with frequency-independent vertices and without self-energy feedback (blue squares), with frequency-dependent vertices and without self-energy feedback (red triangles), and with frequency-dependent vertices and with self-energy feedback (green diamonds), all in the discretization D1.

the Fermi surface is perfectly nested. Previous fRG works have clearly established an AFM instability, signaling an AFM SDW ground state for this case (e.g. [HS01]). This is in accordance with the expectations from simple RPA arguments, and also with QMC results [Var09].

For $t' = 0$, $\mu = 0$, the character of the instability in the fRG does not change when we include a frequency dependence of the effective interactions, or when we include the self-energy feedback. This means that the couplings that drive the AFM susceptibility with wavevector transfer (π, π) diverge most strongly, as described in earlier works [Met12]. In figure 7.3, we show the critical scales obtained in the fRG in the various approximations (without frequency dependence of the effective interactions and without self-energy feedback, with frequency dependence of the effective interactions but without self-energy feedback, and with frequency dependence of the effective interactions and with self-energy feedback) as a function of the interaction strength U . These scales do not differ much quantitatively. One way to understand the agreement is that the instability in this case is very close to a standard RPA instability, where only the most singular frequency transfer matters, and different frequency transfers do not couple, hence the frequency resolution does not come into play. Furthermore, the flow goes off to strong coupling at scales before the self-energy becomes noticeable. Nevertheless, with respect to the plain RPA, the critical scales are reduced by the channel coupling in the fRG. Hence, in this case, the simplest fRG approximation without frequency dependence and without self-

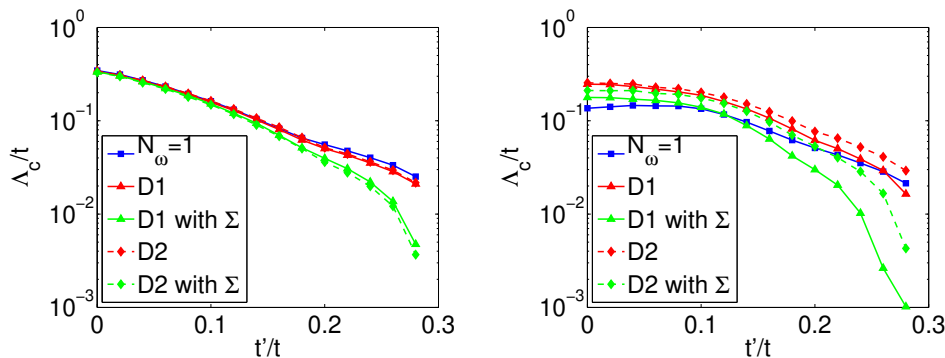


Figure 7.4: Critical scale Λ_c , at which the couplings exceed $20t$, vs. next-nearest-neighbor hopping t'/t at van Hove filling for $U = 3t$ with $N_\omega = 1$ and without self-energy feedback (blue squares), with frequency-dependent vertices and without self-energy feedback (red), with frequency-dependent vertices and with self-energy feedback (green). Two different frequency discretization D1 (triangles, solid lines) and D2 (diamonds, dashed line) are used. Left: $T = 0.01t$. Right: $T = \Lambda_c^{0.01}$ is the t' dependent critical scale for $T = 0.01t$ without self-energy feedback with discretization D1 (red solid line in the left plot).

energy feedback is already quite good and cannot be improved much, within the range of numerical possibilities. Besides the discretizations of wavevector and frequency dependences, the remaining approximations are the neglect of the real part of the self-energy and the truncation of the flow hierarchy after the four-point function, as discussed in sections 2.4 and 2.6. We expect that the remaining differences arise due to these two approximations. In particular for larger $U \approx 4t$, there should be precursors of the spectral weight transfer that ultimately leads to the opening of a Mott gap at $U \approx 8t$. As it is believed that the truncated fRG does not allow the description of the Mott transition, it is plausible that the spectral weight transfer is still not described correctly in our improved approximation. Furthermore, the physics of collective fluctuations might not be captured to some extent due to the truncation after the four-point vertex. Hence, if we compare roughly to gap scales found in non-perturbative cluster calculations for large clusters [MJ01], the Λ_c -curve seems to rise too steeply as function of U . However, regarding the critical scale as an estimate of the gap scale, up to a factor of order one, the fRG is in the right range.

Let us now look at the situation, in which the particle-hole nesting is destroyed by larger t' . In figure 7.4, we plot the critical scale vs. the next-nearest-neighbor hopping t' at van Hove filling (i.e. chemical potential $\mu = -4t'$), at which the van Hove energy with a logarithmic diverging density of states is at

the Fermi level. The fRG flows in the left plot of figure 7.4 have been computed at $T = 0.01t$. Lowering the temperature further increases the numerical effort, as the maximum cutoff frequency ω_∞ then has to be taken larger as well.

As can be seen in figure 7.4 (left) for $T = 0.01t$ the inclusion of frequency dependence and the different discretizations affect the critical scale only slightly. The self-energy feedback however reduces the critical scale significantly especially for larger t' . The data we show are for $U = 3t$, but the agreement is similar for other interaction strengths for which reasonable (i.e. $\geq 10^{-3}t$ for our numerics) critical scales are detected.

One might suspect that the critical scale for higher t' is more strongly suppressed because the critical scale comes closer to the chosen temperature, so that the difference in the critical scale is merely a finite-temperature effect. To check this, we make a second run, where we adjust the temperature for each value of t' , to the value $T = \Lambda_c^{0.01}$, which is the critical scale we obtain for the respective t' at $T = 0.01T$ without self-energy feedback. In other words, the temperature is varied according to the red solid curve in the left plot of figure 7.4. Now the ratio of temperature and critical scale is comparable for all t' . We see that inclusion of self-energy-feedback suppresses the critical scale now already for small t' , but definitely more strongly at larger values of t' .

Interestingly, we find that increasing the temperature reduces the critical scale more strongly, when frequency dependence is neglected, especially at small t' , so that we discover a parameter space, in which now the critical scale increases when one includes frequency dependence in contrast to the left plot of figure 7.4.

We also compared how different patchings on the Matsubara axis affect the critical scales. In figure 7.4 we show data for the two different discretizations of the Matsubara axis D1 and D2, explained in section 7.2. At low temperatures, both discretization schemes lead to very similar results, while at higher temperatures the two discretizations show quantitative differences, depending on t' . The flows with the discretization D2 now exhibit a larger critical scale than the flows with D1. Hence the precision of the approach is better at low T .

We want to have a closer look at the origin of the behavior observed in figure 7.4. A natural question to ask is whether the AFM SDW and the superconducting tendencies respond differently to the inclusion of frequency dependence and self-energy, and whether the tentative phase diagrams drawn by determining the leading instability are changed by these improvements of the scheme. We therefore consider, similarly to the preceding chapter, the effective coupling strengths of the AFM and superconducting channel, which we define as

$$\chi_{\text{AFM}} = \frac{1}{N_k} \sum_{k'} V^\Lambda ((k', \omega_0), (k = 1, \omega_0), (k = 24, \omega_0)) , \quad (7.6)$$

$$\chi_{\text{SC}} = \frac{1}{N_k^2} \sum_{k, k'} V^\Lambda ((k, \omega_0), (-k, -\omega_0), (k', \omega_0)) f(k) f(k') . \quad (7.7)$$

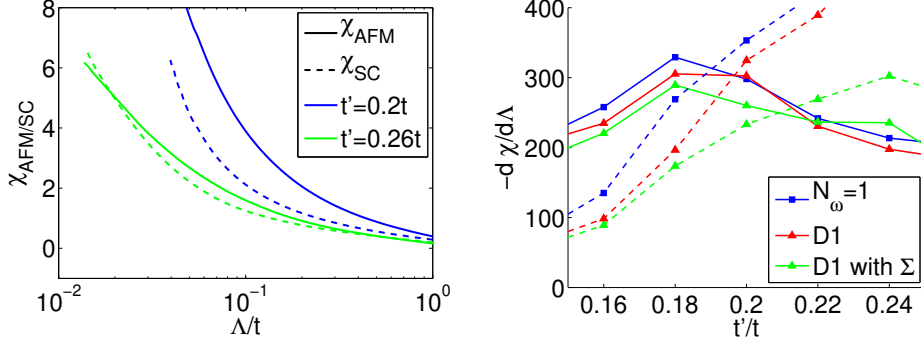


Figure 7.5: Left: Flow of the effective strength of the AFM (solid lines) and superconducting (dashed lines) channel given in equation (7.6, 7.7) in units of t for $t' = 0.2t$ (blue) and $t' = 0.26t$ (green) in the discretization scheme D1 and with self-energy feedback. Right: Slope of the effective strength of the AFM (solid lines) and superconducting (dashed lines) channel at the scale Λ_c , at which the couplings exceed $20t$. Shown are the data with frequency-independent vertices and without self-energy feedback (blue squares), without self-energy feedback (red triangles), and with self-energy feedback (green triangles), both in the discretization scheme D1. The intersection point of the two curves is used as an estimate for the boundary between the AFM and d-wave superconducting regime. All data with $U = 3t$, at van Hove filling and $T = 0.01t$.

Here, $k = 1$ and $k = 24$ denote the patches with momentum vectors closest to the van Hove singularities roughly connected by momentum transfer (π, π) (see figure 7.1) and $\omega_0 = \pi T$. $f(k)$ is a d -wave form factors and given by $f(k) = \cos(k_x) - \cos(k_y)$. We consider the vertices of the smallest Matsubara frequencies, as these grow most strongly during the fRG flow. If these averages diverge, the corresponding susceptibilities diverge as well, so that these quantities can be used as a measure of the coupling strengths of the respective channel. Typical flows of these quantities are shown in the left plot of figure 7.5. As a criterium for the leading instability, we choose the derivatives of the coupling strength of the channels with respect to Λ at Λ_c . Λ_c is again defined as the scale, at which the couplings exceed a value of $20t$. The results are shown in the right plot of figure 7.5. The intersection of the respective curves for the AFM and superconducting coupling strength is taken as an estimate for the boundary between the regimes. Of course, the precise values from this procedure depend somewhat on the chosen definition of Λ_c . On the other hand, this procedure suffices for the more qualitative discussion, in which we are interested, namely the impact of frequency dependence and self-energy effects on the competition between the different orders. The comparison for the different cases, i.e. with and without frequency dependence and self-energy feedback, is summarized in

	without Σ			with Σ	
	$N_\omega = 1$	D1	D2	D1	D2
$T = 0.01t$	0.19	0.2	0.21	0.21	0.22
$T = \Lambda_c^{0.01}$	0.22	0.27	$\gtrsim 0.28$	> 0.28	> 0.28

Table 7.1: Approximate values for t'/t , for the transition from the AFM to the superconducting regime at van Hove filling and $U = 3t$. The values are obtained by the comparison of the slope of the effective strength of the respective channels at the scale Λ_c , at which the couplings exceed $20t$ (see also figure 7.5).

table 7.1.

At $T = 0.01t$, and without self-energy the boundary between the regimes lies at $t' \approx 0.19t$ and without frequency-dependent vertices. If we include the feedback of self-energy, this boundary is shifted towards higher t' . We conclude that, not unexpectedly, life-time effects harm the superconducting instability more than the AFM instability.

For the second run at higher temperatures, $T = \Lambda_c^{0.01}$, the phase boundary is generally shifted towards higher t' as well. This basically reflects the fact that the relevant energy scale of the superconducting instability is lower than that of the AFM instability. Hence, the pairing channel is more strongly affected by the finite temperature. The difference between the different levels of approximations is much larger than at $T = 0.01t$ in correspondence with the larger discrepancy in the critical scales in figure 7.4. Furthermore, we note that the different discretization schemes yield qualitatively similar results, which confirms that the picture drawn here for the leading instabilities is fortunately rather independent of the details of the numerical implementation.

The overall conclusion we can draw from this analysis is that the frequency dependence of the couplings and the self-energy effects are certainly important for quantitative questions. However, in general they do not qualitatively change the physical picture obtained from the simpler flow schemes with frequency-independent couplings, and with neglected self-energy.

7.5 Flow of the Self-Energy

Next, we consider the flow of the self-energy for finite temperatures above T_c . The main goal, now, is to analyze the frequency- and wavevector-dependence.

We run the fRG flow for different $T > T_c$ such that all modes can be integrated out. Practically, the flow is stopped at a scale $\Lambda = 2 \times 10^{-4}t$, which is much lower than the temperature. Below these scales, the vertices and self-energies do not get renormalized substantially, by lowering Λ even further. We stay in the weakly to moderately coupled regime at all scales.

In figure 7.6 the imaginary part of the self-energy is plotted over the Matsub-

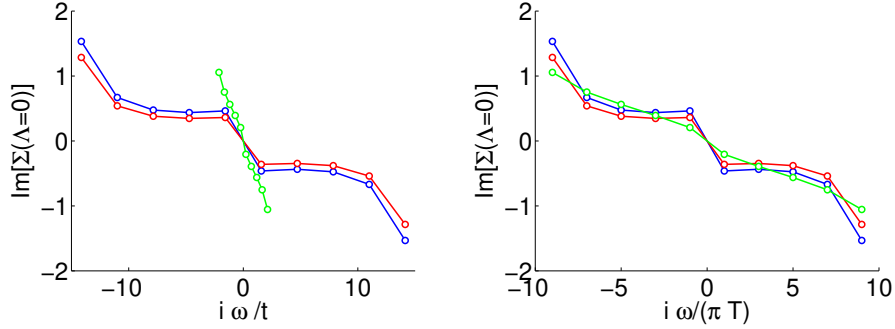


Figure 7.6: Imaginary part of the self-energy in units of t for $T > T_c$ at $\Lambda = 0$ for three parameter choices at van Hove filling, $U = 3t$. $T = 0.5t$, $t' = 0$ (blue); $T = 0.5t$, $t' = 0.25t$ (red); $T = 0.1t$, $t' = 0.25t$ (green). Shown are the data for the patch $k = 1$; the curves for different momenta at the Fermi surface (not shown) are nearly the same, which implies a very weak angular dependence. The left and right plot show the same data with different scaling of the frequency axis. All data with discretization scheme D1 and feedback of self-energy. The largest couplings at $\Lambda = 0$ are of the order of $10t$ for $T = 0.5t$, $t' = 0.25t$ (red). The parameter choices shown in blue and green are close to the critical temperature, here the largest couplings are close to $20t$.

ara frequency for different momentum patches, for the fully nested case with $t' = 0$ at half-filling and for van Hove filling with $t' = 0.25t$. The curves for different patches are nearly on top of each other (not shown in figure 7.6 for better readability). Thus, there is only a weak angular dependence at these elevated temperatures above the instability, independent of the Fermi surface shape. We checked that the weak angular dependence is reproduced in the other frequency discretization schemes as well. On the left-hand side of the plot, we show the data as a function of the Matsubara frequency, i.e. with a different frequency window $\sim T$ for the two temperatures. On the right hand side, we show the same data vs. $i\omega/(\pi T)$ as a function of the Matsubara frequency index.

At higher temperatures, $T = 0.5t$, we observe again a step-like discontinuity in the self-energy at zero frequency on the Matsubara axis. This can be interpreted as an inverse lifetime of the quasi-particle peak. If we go to lower temperatures but remain above the instability (now only for the curved Fermi surface, as, otherwise, the critical scale is too high), this step gets much smaller (also because the Matsubara frequencies move close together) and we are left with a rather linear frequency-dependence, which can again be captured by a quasi-particle weight Z . This, again, turns out to be rather independent of the location on the Fermi surface. So, all these data at fixed temperature look quite consistent with a rather normal and isotropic metallic system, at least at these

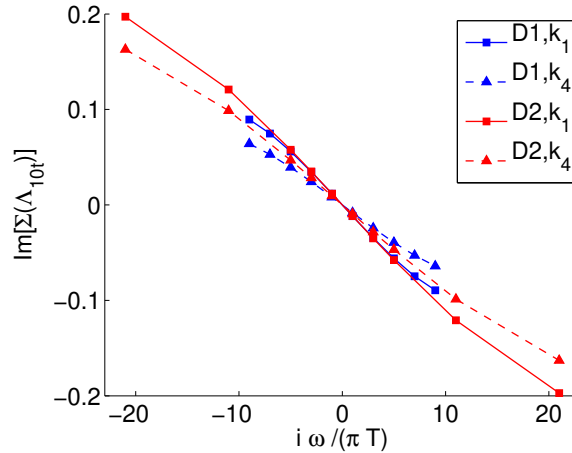


Figure 7.7: Imaginary part of the self-energy in units of t for different discretization schemes D1, D2 at the scale Λ_{10t} , at which the couplings exceed a value of $10t$. $\Lambda_{10t} = 0.084t$ ($\Lambda_{10t} = 0.093t$) for D1 (D2). Shown are different momenta at the Fermi surface $k = 1$ and $k = 4$ (see figure 7.1). All data for $T = 0.01t$, $t' = 0.2t$, $U = 3$, at van Hove filling, and with feedback of self-energy.

temperatures above the instability.

There have been a number of more detailed studies (e.g. [GGV96; FS08]) of the self-energy in the case of van Hove filling, pointing out special, non-Fermi-liquid-like properties due to the diverging density of states. At a given T , it is difficult to read out any particular self-energy property from our data at $t' = 0.25t$. However, if we measure the temperature-dependence of the step-like feature that we interpreted as inverse lifetime and fit it to the law T^α , we obtain a different exponent with α approaching 1 toward lower T . This marginal Fermi-liquid behavior [Var89] is shown in figure 7.2 and is consistent with second-order predictions for the van-Hove situation [LR87; HR95].

In figure 7.7, we show data at lower temperatures for the frequency-dependence of the self-energy, now comparing different frequency discretizations. We compare data at a scale, at which the couplings exceed a value $10t$. Note that this is at slightly different scales in both cases. We see that for low frequencies the discretizations compare quite well. At larger frequencies the quantitative agreement becomes worse. However, the qualitative features, such as, for instance, a larger slope of the self-energy near the saddle points compared to the Brillouin zone diagonal, is found consistently in both schemes. Quite generally, our data show that the self-energies in the two schemes are more consistent at lower temperatures.

For $T < T_c$ the flows go to strong coupling. If we stop the flow when the vertices exceed a value of the bandwidth, the momentum dependence of the self-

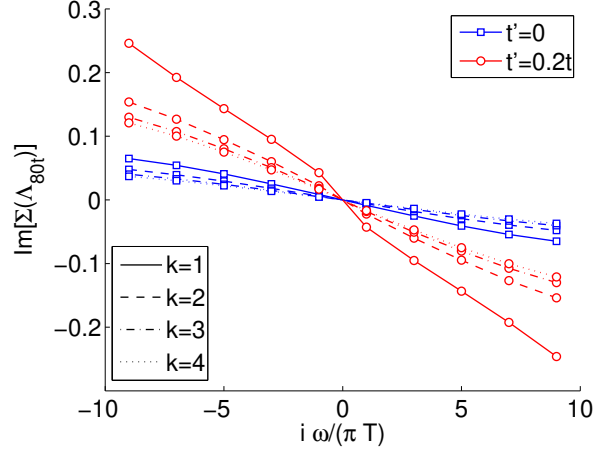


Figure 7.8: Imaginary part of the self-energy in units of t for $t' = 0$ (blue) and $t' = 0.2$ (red) at van Hove filling for $U = 3t$, at the scale Λ_{80t} , where the couplings exceed a value of $80t$. $\Lambda_{80t} = 0.26t$ ($\Lambda_{80t} = 0.019t$) for $t' = 0$ ($t' = 0.2t$). Shown are different momenta at the Fermi surface $k = 1$ (solid line), $k = 2$ (dashed line), $k = 3$ (dashed dotted line), and $k = 4$ (dotted line) (see figure 7.1). All data with discretization scheme D1 and with feedback of self-energy.

energy is rather weak. However, if we continue to flow towards the instability, stronger anisotropies are found. Strictly speaking, for these large values of the vertices the truncation of the fRG flow equation with neglect of the higher-order vertices is no longer justified. We expect, however, that we can still get some qualitative insight into the breakdown of the Fermi-liquid behavior for low temperatures, similar to the argumentation in previous works [KK04; RM05]. The corresponding data are shown in figure 7.8.

In general, the frequency-dependence of the imaginary part of the self-energy at these low temperatures near the instability is dominated by a linear decrease that gets steeper, the closer we get to the critical scale. We can measure this angle-dependent slope Σ'^{Λ} on the frequency window and encode it in a quasi-particle weight at the Fermi level

$$Z^{\Lambda} = \left[1 - \Sigma'^{\Lambda}\right]^{-1}, \quad (7.8)$$

where we define Σ'^{Λ} as

$$\Sigma'^{\Lambda} = \frac{\Sigma^{\Lambda}(k_F, \omega_m) - \Sigma^{\Lambda}(k_F, -\omega_m)}{2\omega_m}. \quad (7.9)$$

Here, $\Sigma^{\Lambda}(k_F, \pm\omega_m)$ are the self-energies at the Matsubara frequencies with the largest absolute value $\omega_m = 9\pi T$ available in discretization D1. The flow of

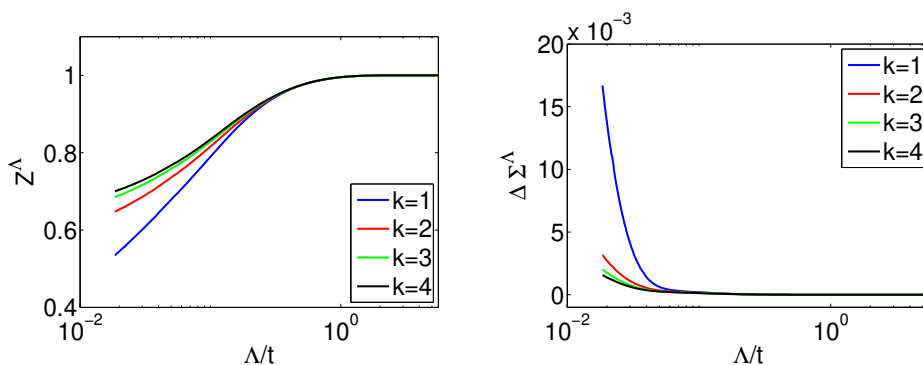


Figure 7.9: Flow of the Z -factor as given by equations (7.8, 7.9) and the step $\Delta \Sigma^\Lambda$ of the self-energy in units of t at $\omega = 0$ defined as in equation (7.4) for different momenta at the Fermi surface (see figure 7.1). $U = 3t$, $t' = 0.2t$, van Hove filling, $T = 0.01t$, with discretization scheme D1 and with feedback of self-energy.

these weights is shown in figure 7.9. We see that the Z -factor diminishes toward the instability, but in a rather weak, almost logarithmic way, such that this is possibly not the most severe effect in the self-energy. In addition to this slope, we also notice again a step $\Delta \Sigma^\Lambda$ around zero frequency, that grows rapidly toward the instability, as shown in the right plot of figure 7.9. We also show curves for different locations on the Fermi surface. These different lines indicate the growth of the anisotropy toward the instability for the van Hove situation away from half-filling, with stronger self-energy effects for Fermi surface points near the van Hove points. In the perfectly nested case, the anisotropy is less pronounced.

Previous works on the flow of the self-energy, using different approximations, have arrived at some similar but also some different conclusions regarding the self-energy flow. In Refs. [KK04; RM05] the anisotropy appears to be somewhat more pronounced in the sense that the Fermi surface point closest to the van Hove points showed indications for a break-up of the quasi-particle peak into two peaks, with a spectral gap opening between them. For this to occur, one needs an additional low-energy feature in the self-energy. On the imaginary axis, this shows up as an increase of the absolute value of the self-energy imaginary part towards low frequencies, which turns around the linear slope and eventually leads to a $1/(i\omega)$ -pole. In [KK04] this could only be seen clearly by interpolating between the lowest Matsubara frequencies, an option we cannot choose in our flow with frequency-dependent coupling. However, the growing step $\Delta \Sigma^\Lambda$ can be interpreted as a precursor of this effect, as it leads to a breaking up of the simple linear decrease. It is quite possible that these subtle effects very close to the instability come out in a different extent in the different approximations. Also in [RM05], where the self-energy is evaluated directly on the real frequency

axis, a low-energy feature in the self-energy emerges very close to the instability and eventually splits the quasi-particle peak in two. Another aspect of this feature is a rise in the scattering rate, which is consistent with our increasing step $\Delta\Sigma^\Lambda$. On the real axis, the linear slope of the self-energy real part goes into the Z -factor. In [RM05], this slope, after subtracting the additional low-energy feature is not strongly scale-dependent, very much like our data, where the Z -factor does not really dive to zero, towards the instability. Since the precision of the truncated flows is not very high in this regime, we refrain from a more elaborate discussion of these differences. One message one may learn from these studies is however that the self-energy in this regime should not only be parametrized with a Z -factor. At least close to the instability, it develops additional low-energy structures besides this linear envelope captured by the Z -factor.

7.6 Discussion

We have analyzed the low-energy properties of effective interactions and self-energies in the two-dimensional Hubbard model, using a fRG scheme, which takes into account the frequency-dependence of the interactions and the feedback of important parts of the self-energy on the flow of the latter. This is in contrast to the approach in previous chapters and other works on the same model (e.g. [ZS00; HM00; Hon01; HS01] and many works cited in [Met12]). Here, we discretized the Matsubara frequency axis in different schemes with $N_\omega = 10$ patches. For the self-energy, we took into account the imaginary part (on the Matsubara axis) only, while we ignored the real part. The argument for ignoring the latter is mainly feasibility, i.e., a flowing dispersion is technically difficult to deal with, and would require additional devices to keep the particle number fixed. Our experience from previous studies [Ueb09] is that the impact of the dispersion renormalization on the instability is mainly quantitative and does not alter the regime found from the flows to strong coupling.

The main goal of this study was to see how the fRG flows of the simpler studies are altered by the straightforward inclusion of frequency-dependence and (the imaginary part of the) self-energy feedback. Here, after a first sanity check on a case without flow to strong coupling, we analyzed how the critical scales for the flow to strong coupling change, and how the character of the instability in terms of the leading ordering tendency changes depending on the different approximations. The overall result is that the frequency-dependence and the imaginary part of the self-energy usually decrease the critical scales by a factor at most of order 1. Only near quantum critical points, where the critical scales vary strongly and become small, can the change be more drastic. Furthermore, the competition for the leading instability is also affected only quantitatively. We find the same structure of the phase diagrams, and we have not seen that any of the regimes found previously are wiped out by these alterations of the

scheme. In particular, there is a sizable regime with dominating d -wave pairing in the ground state.

Above the instability temperatures, the self-energy did not show strong signatures in its frequency- or wavevector-dependence. The basic structure could be captured by an inverse lifetime or scattering rate and a Z -factor for the quasi-particle weight. These parameters turned out to be weakly wavevector-dependent around the Fermi surface unless one gets close to the instability at lower temperatures. At van Hove filling and away from perfect nesting, the scattering rate above the instability turns out to be consistent with marginal Fermi-liquid behavior, as found in previous studies [LR87; HR95]. However, this does not prevent the low- T instabilities from occurring, i.e. even if the self-energy behaves differently from a Fermi-liquid, the instabilities found without inclusion of the self-energy are still present.

These findings on the behavior of the self-energy above the instability make a lot of sense, but they do not reveal any unexpected physics. Certainly, the self-energy flows corroborate second-order-perturbation theory results on the non-Fermi-liquid behavior at the van Hove filling, and the low- T instabilities are not changed qualitatively. Hence the present work represents an important check for the body of knowledge that has been obtained using simple fRG flows without self-energy feedback ([Met12] and references therein). Basically, the message we infer from the data is that frequency-dependence and self-energy effects are necessary to deal with if one is trying to obtain truly quantitative results, but on a qualitative level, regarding the leading instabilities and orders of magnitude, these improvements do not lead to significant changes. So the simple flows without self-energy are expected to be good guides through the basic phase diagrams. Similar statements also hold for parameter trends, e.g. as a function of the chemical potential of the band-structure parameters. Here, we have found that these trends occur irrespective of the approximation level.

In this work, we do not discuss explicitly the frequency structure of the effective interactions. This is quite rich and contains some interesting aspects, some of which have been discussed without self-energy feedback in [HFL07]. Here, however, it is difficult to describe the data with a few simple parameters, and less literature is available for comparison. Hence we did not elaborate on this here. It would be interesting, however, to compare the frequency-resolved vertex functions from this weak-coupling approach with data obtained with QMC or dynamical mean-field-like cluster methods, in order to assess the effects of strong correlations (possibly difficult for the fRG) and larger distances (possibly less well captured by the strong-coupling approaches) on these objects.

Regarding the theoretical approach chosen here, we were able to show that it leads to useful results. On the other hand, in order to look for subtle effects near the instability such as pseudogaps or more detailed non-Fermi-liquid behavior, the chosen approach appears to be somewhat too heavy and inflexible. The numerical effort due to a vertex that depends on three wavevectors and

frequencies makes it rather cumbersome to compare different discretizations or implementations. Here, some clever reduction of the information carried along might be useful. Our current code might serve as a guide to assess the value of these alternatives.

Recently, another publication treating the self-energy feedback in fRG flows in the two-dimensional Hubbard model has appeared [GS12] which may point in the right direction. This study employs the channel decomposition of the interaction vertex proposed by Husemann and Salmhofer [HS09]. The restriction to a few form factors of the interaction channels then allows the authors to reach a higher momentum space and frequency precision than is achieved in our straightforward patching scheme, and to safely go to the lowest temperatures and frequencies. Furthermore they also consider the flow of the real part of the self-energy which was ignored in our scheme for simplicity. The choice of a soft frequency cutoff, instead of a momentum-shell cutoff, picks up ferromagnetic tendencies, which are ignored in our approach and which would be important for $t' > 0.3t$ near van Hove filling. So, the results of both schemes should only be compared at small t' . There seems to be good agreement at least in two aspects, namely the suppression of the critical scales due to self-energy effects, and the stability of the d -wave pairing regime with respect to inclusion of these aspects. Ref. [GS12] also describes a non-Fermi-liquid behavior of the self-energy at the van Hove-filling with exponent $3/4$ at $t' = 0.355t$, which is slightly less than our second-order-like exponent near 1 determined for $t' = 0.25t$. In comparing the pros and cons of these two related schemes, it is important to notice that our direct patching implementation without channel decomposition does allow the vertex to depend on three different wavevectors and Matsubara frequencies, while the approach in [GS12] only allows for certain form factors in momentum space and treats the frequency-dependence as the sum of three functions, each depending on one particular frequency combinations. However, it is hoped that these constraints do not influence the results too strongly. Indeed, our study shows that taking along more frequency- and momentum-structure does not change the main results and does not reveal any additional physics. Hence, it is quite likely that the channel-resolved formalism of [GS12] turns out to be a better compromise, as it reduces the amount of information carried along in the flow in a physically meaningful way. In this way, one might obtain more precise data and be able to go on to more involved systems without reducing the precision again. In a way, the approach chosen in this work can be viewed as complementary, as it is less versatile but puts less of a bias in the momentum and frequency dependencies of the vertex functions.

Chapter 8

Conclusion and Outlook

In this work, we studied various quasi two-dimensional multiorbital systems by means of the fRG formalism. The approach is well suited for the application to various band-structures, multiple orbitals or different interaction parameters. In particular, we profited from the fact that one does not need to rely on an educated guess for the types of ordering, which are most relevant for a given model. In the following, we recap the main results of the treated subjects and give an outlook on possible directions of future research.

One motivation for the research described in chapters 3 – 5 was the search for interaction-induced topological insulators. The question is, whether one can find materials, where topological insulators emerge from symmetry breaking by electron-electron interaction. This possibility opens up an entire new direction for the search of topological insulators.

First, we considered two models featuring a single QBCP. The emergence of topological non-trivial QAH and QSH phase was found for interaction parameters that appear quite natural. Due to the finite density of states at the Fermi level, no particularly strong interaction is needed, to stabilize topological phases. We have seen, that the orbital admixture, which manifests itself in the winding of the Bloch eigenvectors around the band crossing point, is crucial for the emergence of topological phases. This study serves as a reference point for the investigation of more involved models and provides basic insight that a system with a QBCP is a good starting point for the search of topologically non-trivial phases induced by interactions.

Afterwards, we investigated in a similar spirit the instabilities of electrons on the honeycomb bi- and trilayer. These models have a direct realization in thin graphene layers, so that the theoretical results can be directly compared to experimental observations in these materials. We observed CDW and AFM SDW instabilities, as well as an instability towards a QSH phase, whose edge states, in the case of the trilayer, are topologically protected. For the interaction parameters extracted from ab initio calculations [Weh11], SDW and QSH instability are in close competition and it depends on the precise shape of the interaction, which one is leading. We observed a discrepancy between the experimentally observed gaps and the energy scales inferred from the critical scale of the fRG flow, when one takes the interaction strength derived from DFT+cRPA. However, with rescaled interactions, which leave the single layer in the semi-metallic

phase, the fRG is able to qualitatively reproduce experimental gap sizes in bi- and trilayer graphene consistently. The type of the leading instability is not affected by this rescaling procedure.

It will be interesting whether the nature of the ground state can be pinpointed from the experimental side and whether our predictions on the ground state can be confirmed. Especially, the possible realization of an interaction-driven topological insulator presents an exciting perspective for future research.

From the theory side, an extension of the examined parameter space might be worthwhile. Spin-spin interactions for instance have been shown to promote pairing instabilities in the honeycomb single layer at finite chemical potential [Hon08]. Also, the effect of long-ranged Coulomb interactions and trigonal warping terms is yet to be analyzed in more detail.

Whereas in the cases described above the multiorbital character was absolutely necessary, we additionally studied the influence of orbital admixture in a model, which can be considered as an extension of the usual one-band Hubbard model. This work was motivated by an intriguing material trend in the cuprates namely that compounds which in a single band picture exhibit a larger next-nearest-neighbor hopping, i.e. a rounder Fermi surface, generally exhibit larger critical temperatures than compounds with a more nested Fermi surface [Pav01]. This is highly unexpected from the perspective of a naive picture from spin-fluctuation theories.

The inclusion of additional orbitals, namely the $4s$ and $3d_{22}$ orbitals can at least partly resolve this issue. We discovered that the effect from orbital mixing in the fRG flow is detrimental to the critical scale. This effect can be made very transparent within a simplified two-patch-model, which only takes into account interactions at the van Hove points. Based on this insight one can explain how compounds with a rounder Fermi surface can exhibit higher critical temperatures, namely due to the reduced orbital mixing, in accordance with a previous study by Sakakibara et al. [Sak10]. The fRG calculation on the three-band model confirmed this trend, at least in some parameter window, which is however most relevant for the actual materials. The data suggests that this mechanism is even more effective at strong coupling, which we cannot investigate within the fRG scheme due to the employed approximations. Therefore, it would be highly interesting to study the influence of higher bands with methods, which are suited for the strong coupling case, to see whether the picture we obtained from fRG remains valid. Moreover, the consideration of additional parameters which can influence the critical temperature, and the extension of the one-band Hubbard model to different models, as for instance the Emery model, seem to be promising subjects for future research. We have seen, that virtual processes in the high-energy sector, which we treated within second order perturbation theory, can have a pronounced impact on the behavior of the fRG flows. Therefore, a more rigorous inclusion of virtual excitations in higher bands [MH12], which can for instance lead to a non-trivial frequency

dependence of interaction parameters [Hon12], is desirable.

Although traditionally the cuprates have been by far mostly studied within the one-band description of the cuprates and there is good reason to consider this a suitable approximation, the study presented in chapter 6 substantiates the proposition that the story of the high- T_c superconductivity in copper compounds cannot be told completely by referring exclusively to the one-band model.

Lastly, we investigated the feedback of the imaginary part of the self-energy and the inclusion of frequency dependence of the vertices in the fRG flow in chapter 7. The basic conclusion we can draw from this study, is that phase diagrams, that are obtained with neglect of these contributions as in the rest of this thesis and in numerous other works, should give qualitatively reasonable results. Generally, the self-energy tends to lower energy scales, at which correlation effects become strong, however a drastic change has been observed only in the vicinity of a critical point.

To develop the fRG into a more quantitative method, further research in this direction is needed. Despite rapidly increasing available computing power, the rigorous inclusion of self-energy and frequency dependence is still a delicate matter. Significant improvement of the quantitative predictive power of the fRG might be possible, by using a parametrization for the most relevant contributions to the flow [HS09]. This, however, is not straightforwardly generalizable to more complicated, e.g. multiorbital, systems. Therefore, the approach of neglecting self-energy and frequency dependence, which has been employed in large parts of this thesis and in many other works, is a sensible compromise, in order to obtain a reliable qualitative picture of the low energy behavior of a weakly or moderately coupled system at reasonable expense.

Appendix A

Improved Patching for the Checkerboard Lattice Model

In section 3.5, we have found non-local order parameters corresponding to the QAH and QSH phase. Here, we want to discuss the manifestation of this non-locality, i.e. the corresponding modulation factor in momentum space, by reference to the QAH order parameter given in equation (3.22).

In the standard setup, employed in chapter 3, the patching points are located on a ring in the close vicinity of the QBCP, which is located at (π, π) . The radius of the ring is chosen to be $k_r = 0.3\pi$ (The lattice constant has been set to unity). With this setup, the modulation of the order parameter corresponding to the prefactor $\sin \frac{k_x}{2} \sin \frac{k_y}{2}$ in equation (3.22) is not observed, because the prefactor, evaluated at the locations of the patching points, is nearly a constant.

Therefore, we introduced additional radial patches for a better resolution of the momentum-dependent variation of the interaction vertex. If the interac-

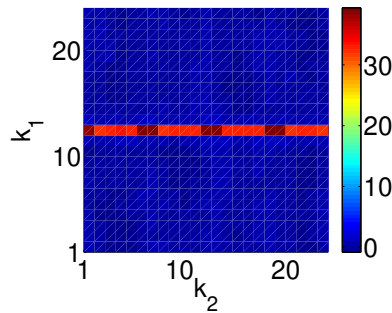


Figure A.1: Effective interaction near the critical scale in the QAH phase of the lattice model in units of t . The patch k_1 (k_2) of the first (second) ingoing leg is plotted on the y (x) axis, with the discretization similar to the one shown in figure 3.1, but with two rings of patching points, at which the vertex is computed. The number of patches is chosen to be $N = 24$. $k_3 = 12$ is kept fixed. Here k_2 is set on the outer ring, so that the modulation of the order parameter in equation (3.22) can be observed. In our convention, the first and the third line have the same spin. Shown are the vertices with the orbitals $o_1 = o_2 \neq o_3 = o_4$.

tion vertex is computed at larger distance, one can clearly observe 4 maxima when varying, say k_2 around the QBCP at fixed $k_1 = k_3$, which reflects the modulation factor written in equation (3.22). More precisely, we introduced a second ring of momenta, at which the coupling function is computed, with a radius of $k_r = 0.9\pi$. A snapshot of the interaction vertex near the critical scale of the QAH instability is shown in figure A.1. Here, k_3 is fixed, and k_1 is varied around the QBCP on the inner ring, whereas k_2 is set on the outer ring, going once around the QBCP. We clearly observe the four maxima corresponding to the momentum dependence in equation (3.22). The corresponding analysis for the case of the QSH instability yields a similar picture.

Appendix B

Critical Scale from RPA

In sections 4.5 and 5.3, we provided expressions for the dependence of the critical scale on the initial interactions for the honeycomb bi- and trilayer, expected from RPA. Here, we present the corresponding calculation. An analogue derivation is done, for instance, in [HS01] for instabilities in the one-band Hubbard model.

We consider a model with a particle-hole symmetric dispersion relation, that fulfills the nesting condition at vanishing momentum transfer $\epsilon_1(k) = -\epsilon_2(k)$. If we consider only the crossed particle-hole diagram with vanishing momentum transfer at zero frequency, we can write down a simplified flow equation for the interaction vertex V^Λ , which sums up the corresponding RPA ladder

$$\dot{V}^\Lambda = -L^\Lambda (V^\Lambda)^2 . \quad (\text{B.1})$$

The particle-hole loop with all contributions from modes with energy larger than a scale Λ is given by

$$L = 2 \int_{\Lambda}^W d\epsilon \rho(\epsilon) \frac{n_F(\epsilon) - n_F(\epsilon')}{\epsilon - \epsilon'} , \quad (\text{B.2})$$

where $\rho(\epsilon)$ is the density of states, $n_F(\epsilon)$ the Fermi-function and $\epsilon' = -\epsilon$ is the energy of the second leg on the lower band. W is the bandwidth. The factor two arises from the two contributions $\epsilon > 0$ and $\epsilon < 0$, which are identical, due to the particle-hole symmetry. The particle-hole loop at scale Λ is then given by $L^\Lambda = d/d\Lambda L$. At zero temperature this can be simplified, yielding

$$L^\Lambda = \frac{d}{d\Lambda} \int_{\Lambda}^W d\epsilon \rho(\epsilon) \left(-\frac{1}{\epsilon}\right) = \rho(\Lambda) \frac{1}{\Lambda} . \quad (\text{B.3})$$

We assume the density of states to be of the form $\rho(\epsilon) = \rho_0 \epsilon^\alpha$, with $\alpha \neq 0$ and ρ_0 being constant, and solve equation (B.1) by separating the variables

$$\int_{V^\Lambda}^{V_0} \frac{dV}{V^2} = - \int_{\Lambda}^W d\Lambda' L^{\Lambda'} , \quad (\text{B.4})$$

with V_0 being the initial interaction strength. This yields the solution of the

flow equation

$$V^\Lambda = \frac{V_0}{1 - \frac{V_0\rho_0}{\alpha}(W^\alpha - \Lambda^\alpha)} . \quad (\text{B.5})$$

The denominator vanishes at the critical scale

$$\Lambda_c = \left(W^\alpha - \frac{\alpha}{V_0\rho_0} \right)^{\frac{1}{\alpha}} . \quad (\text{B.6})$$

For $\alpha = -\frac{1}{3}$, as is the case for the ABC stacked trilayer with a cubic dispersion relation $\epsilon_{1,2}(k) \sim \pm|k|^3$, this gives

$$\Lambda_c = \left(\frac{3V_0\rho_0}{1 + 3V_0\rho_0 W^{-\frac{1}{3}}} \right)^3 , \quad (\text{B.7})$$

which, for small V_0 , can be approximated to

$$\Lambda_c \sim V_0^3 , \quad (\text{B.8})$$

as stated in section 5.3.

For the dispersion with QBCPs, we have a constant density of states $\rho(\epsilon) = \rho_0$, so that $\alpha = 0$. With the same steps as above, we arrive at the solution for the flow equation

$$V^\Lambda = \frac{V_0}{1 - V_0\rho_0 \log\left(\frac{W}{\Lambda}\right)} . \quad (\text{B.9})$$

The critical scale, at which the denominator vanishes, reads

$$\Lambda_c = W \exp\left(-\frac{1}{V_0\rho_0}\right) . \quad (\text{B.10})$$

This well known exponential behavior of the critical scale has been confirmed by the fRG data for the models on the honeycomb bilayer and the ABA stacked trilayer without remote hoppings in sections 4.5 and 5.3.

Bibliography

- [And06] S. Andergassen. “Functional Renormalization-Group Analysis of Luttinger Liquids with Impurities”. <http://arxiv.org/abs/cond-mat/0603341>. PhD thesis. Universität Stuttgart, 2006.
- [And95] O. K. Andersen, A. I. Liechtenstein, O. Jepsen, and F. Paulsen. “LDA energy bands, low-energy hamiltonians, t' , t'' , $t_{\perp}(k)$, and J_{\perp} ”. *Journal of Physics and Chemistry of Solids* 56 (1995). Proceedings of the Conference on Spectroscopies in Novel Superconductors, 1573–1591. DOI: 10.1016/0022-3697(95)00269-3.
- [APP10] A. A. Avetisyan, B. Partoens, and F. M. Peeters. “Stacking order dependent electric field tuning of the band gap in graphene multilayers”. *Phys. Rev. B* 81 (2010), 115432. DOI: 10.1103/PhysRevB.81.115432.
- [Ary04] F. Aryasetiawan, M. Imada, A. Georges, G. Kotliar, S. Biermann, and A. I. Liechtenstein. “Frequency-dependent local interactions and low-energy effective models from electronic structure calculations”. *Phys. Rev. B* 70 (2004), 195104. DOI: 10.1103/PhysRevB.70.195104.
- [Ary06] F. Aryasetiawan, K. Karlsson, O. Jepsen, and U. Schönberger. “Calculations of Hubbard U from first-principles”. *Phys. Rev. B* 74 (2006), 125106. DOI: 10.1103/PhysRevB.74.125106.
- [AS06] A. Altland and B. Simons. *Condensed Matter Field Theory*. Cambridge University Press, 2006. ISBN: 9780521845083.
- [Bao10] W. Bao, Z. Zhao, H. Zhang, G. Liu, P. Kratz, L. Jing, J. Velasco, D. Smirnov, and C. N. Lau. “Magnetoelectronic Oscillations and Evidence for Fractional Quantum Hall States in Suspended Bilayer and Trilayer Graphene”. *Phys. Rev. Lett.* 105 (2010), 246601. DOI: 10.1103/PhysRevLett.105.246601.
- [Bao11] W. Bao, L. Jing, J. Velasco, Y. Lee, G. Liu, D. Tran, B. Standley, M. Aykol, S. B. Cronin, D. Smirnov, M. Koshino, E. McCann, M. Bockrath, and C. N. Lau. “Stacking-dependent band gap and quantum transport in trilayer graphene”. *Nat. Phys.* 7 (2011), 948–952. DOI: 10.1038/nphys2103.

- [Bao12] W. Bao, J. Velasco, F. Zhang, L. Jing, B. Standley, D. Smirnov, M. Bockrath, A. H. MacDonald, and C. N. Lau. “Evidence for a spontaneous gapped state in ultraclean bilayer graphene”. *Proceedings of the National Academy of Sciences* 109 (2012), 10802–10805. DOI: 10.1073/pnas.1205978109.
- [BCR12] Y. Barlas, R. Côté, and M. Rondeau. “Quantum Hall to Charge-Density-Wave Phase Transitions in *ABC*-Trilayer Graphene”. *Phys. Rev. Lett.* 109 (2012), 126804. DOI: 10.1103/PhysRevLett.109.126804.
- [BDS11] J. Braun, S. Diehl, and M. M. Scherer. “Finite-size and particle-number effects in an ultracold Fermi gas at unitarity”. *Phys. Rev. A* 84 (2011), 063616. DOI: 10.1103/PhysRevA.84.063616.
- [BHZ06] B. A. Bernevig, T. L. Hughes, and S.-C. Zhang. “Quantum Spin Hall Effect and Topological Phase Transition in HgTe Quantum Wells”. *Science* 314 (2006), 1757–1761. DOI: 10.1126/science.1133734.
- [Bla01] P. Blaha, K. Schwarz, G. Madsen, D. Kvasnicka, and J. Luitz. “Wien2k-package” (2001). <http://www.wien2k.at>.
- [BTW02] J. Berges, N. Tetradis, and C. Wetterich. “Non-perturbative renormalization flow in quantum field theory and statistical physics”. *Physics Reports* 363 (2002), 223–386. DOI: 10.1016/S0370-1573(01)00098-9.
- [Cas09] A. H. Castro Neto, F. Guinea, N. M. R. Peres, K. S. Novoselov, and A. K. Geim. “The electronic properties of graphene”. *Rev. Mod. Phys.* 81 (2009), 109–162. DOI: 10.1103/RevModPhys.81.109.
- [CEE08] A. V. Chubukov, D. V. Efremov, and I. Eremin. “Magnetism, superconductivity, and pairing symmetry in iron-based superconductors”. *Phys. Rev. B* 78 (2008), 134512. DOI: 10.1103/PhysRevB.78.134512.
- [CTV12] V. Cvetkovic, R. E. Throckmorton, and O. Vafek. “Electronic multicriticality in bilayer graphene”. *Phys. Rev. B* 86 (2012), 075467. DOI: 10.1103/PhysRevB.86.075467.
- [DD02] M. S. Dresselhaus and G. Dresselhaus. “Intercalation compounds of graphite”. *Advances in Physics* 51 (2002), 1–186. DOI: 10.1080/00018730110113644.
- [DHM01] E. Dagotto, T. Hotta, and A. Moreo. “Colossal magnetoresistant materials: the key role of phase separation”. *Physics Reports* 344 (2001), 1–153. DOI: 10.1016/S0370-1573(00)00121-6.
- [DW06] S. Diehl and C. Wetterich. “Universality in phase transitions for ultracold fermionic atoms”. *Phys. Rev. A* 73 (2006), 033615. DOI: 10.1103/PhysRevA.73.033615.

-
- [DW07] S. Diehl and C. Wetterich. “Functional integral for ultracold fermionic atoms”. *Nuclear Physics B* 770 (2007), 206–272. DOI: 10.1016/j.nuclphysb.2007.02.026.
- [EM10] A. Eberlein and W. Metzner. “Parametrization of Nambu Vertex in a Singlet Superconductor”. *Progress of Theoretical Physics* 124 (2010), 471–491. DOI: 10.1143/PTP.124.471.
- [Ens05] T. Enss. “Renormalization, Conservation Laws and Transport in Correlated Electron Systems”. PhD thesis. Universität Stuttgart, 2005.
- [FHL06] H. C. Fu, C. Honerkamp, and D.-H. Lee. “Renormalization group study of the electron-phonon interaction in high- T_c cuprates”. *Europhys. Lett.* 75 (2006), 146. DOI: 10.1209/epl/i2006-10082-0.
- [Fis74] M. E. Fisher. “The renormalization group in the theory of critical behavior”. *Rev. Mod. Phys.* 46 (1974), 597–616. DOI: 10.1103/RevModPhys.46.597.
- [Flo08] S. Floerchinger, M. Scherer, S. Diehl, and C. Wetterich. “Particle-hole fluctuations in BCS-BEC crossover”. *Phys. Rev. B* 78 (2008), 174528. DOI: 10.1103/PhysRevB.78.174528.
- [FMY09] B. E. Feldman, J. Martin, and A. Yacoby. “Broken-symmetry states and divergent resistance in suspended bilayer graphene”. *Nat. Phys.* 5 (2009), 889–893. DOI: 10.1038/nphys1406.
- [Fre12] F. Freitag, J. Trbovic, M. Weiss, and C. Schönenberger. “Spontaneously Gapped Ground State in Suspended Bilayer Graphene”. *Phys. Rev. Lett.* 108 (2012), 076602. DOI: 10.1103/PhysRevLett.108.076602.
- [FRS98] N. Furukawa, T. M. Rice, and M. Salmhofer. “Truncation of a Two-Dimensional Fermi Surface due to Quasiparticle Gap Formation at the Saddle Points”. *Phys. Rev. Lett.* 81 (1998), 3195–3198. DOI: 10.1103/PhysRevLett.81.3195.
- [FS08] J. Feldman and M. Salmhofer. “Singular Fermi Surfaces II: The Two-Dimensional Case”. *Rev. Math. Phys.* 20 (2008), 275–334. DOI: 10.1142/S0129055X08003304.
- [Ger05] R. Gersch, C. Honerkamp, D. Rohe, and W. Metzner. “Fermionic renormalization group flow into phases with broken discrete symmetry: charge-density wave mean-field model”. *The European Physical Journal B - Condensed Matter and Complex Systems* 48 (2005), 349–358. DOI: 10.1140/epjb/e2005-00416-8.
- [GGV96] J. González, F. Guinea, and M. A. H. Vozmediano. “Renormalization group analysis of electrons near a van Hove singularity”. *Europhys. Lett.* 34 (1996), 711. DOI: 10.1209/epl/i1996-00519-4.

- [GHM08] R. Gersch, C. Honerkamp, and W. Metzner. “Superconductivity in the attractive Hubbard model: functional renormalization group analysis”. *New Journal of Physics* 10 (2008), 045003. DOI: 10.1088/1367-2630/10/4/045003.
- [Gie06] H. Gies. “Introduction to the functional RG and applications to gauge theories” (2006). <http://arxiv.org/abs/hep-ph/0611146>.
- [GLS11] R. van Gelderen, L.-K. Lim, and C. M. Smith. “Spin and band ferromagnetism in trilayer graphene”. *Phys. Rev. B* 84 (2011), 155446. DOI: 10.1103/PhysRevB.84.155446.
- [Gmi09] M. Gmitra, S. Konschuh, C. Ertler, C. Ambrosch-Draxl, and J. Fabian. “Band-structure topologies of graphene: Spin-orbit coupling effects from first principles”. *Phys. Rev. B* 80 (2009), 235431. DOI: 10.1103/PhysRevB.80.235431.
- [GN07] A. K. Geim and K. S. Novoselov. “The rise of graphene”. *Nat. Mater.* 6 (2007), 183–191. DOI: 10.1038/nmat1849.
- [Gor12] E. V. Gorbar, V. P. Gusynin, V. A. Miransky, and I. A. Shovkovy. “Coexistence and competition of nematic and gapped states in bilayer graphene”. *Phys. Rev. B* 86 (2012), 125439. DOI: 10.1103/PhysRevB.86.125439.
- [Got12] S. Göttel, S. Andergassen, C. Honerkamp, D. Schuricht, and S. Wessel. “Critical scales in anisotropic spin systems from functional renormalization”. *Phys. Rev. B* 85 (2012), 214406. DOI: 10.1103/PhysRevB.85.214406.
- [GS12] K.-U. Giering and M. Salmhofer. “Self-energy flows in the two-dimensional repulsive Hubbard model” (2012). <http://arxiv.org/abs/1208.6131>.
- [Hal88] F. D. M. Haldane. “Model for a Quantum Hall Effect without Landau Levels: Condensed-Matter Realization of the "Parity Anomaly"”. *Phys. Rev. Lett.* 61 (1988), 2015–2018. DOI: 10.1103/PhysRevLett.61.2015.
- [Han09] P. Hansmann, X. Yang, A. Toschi, G. Khaliullin, O. K. Andersen, and K. Held. “Turning a Nickelate Fermi Surface into a Cuprate-like One through Heterostructuring”. *Phys. Rev. Lett.* 103 (2009), 016401. DOI: 10.1103/PhysRevLett.103.016401.
- [HFL07] C. Honerkamp, H. C. Fu, and D.-H. Lee. “Phonons and d -wave pairing in the two-dimensional Hubbard model”. *Phys. Rev. B* 75 (2007), 014503. DOI: 10.1103/PhysRevB.75.014503.

-
- [HGS12] C. Husemann, K.-U. Giering, and M. Salmhofer. “Frequency-dependent vertex functions of the (t, t') Hubbard model at weak coupling”. *Phys. Rev. B* 85 (2012), 075121. DOI: 10.1103/PhysRevB.85.075121.
- [HK10] M. Z. Hasan and C. L. Kane. “Colloquium: Topological insulators”. *Rev. Mod. Phys.* 82 (2010), 3045–3067. DOI: 10.1103/RevModPhys.82.3045.
- [HLA11] M. Hohenadler, T. C. Lang, and F. F. Assaad. “Correlation Effects in Quantum Spin-Hall Insulators: A Quantum Monte Carlo Study”. *Phys. Rev. Lett.* 106 (2011), 100403. DOI: 10.1103/PhysRevLett.106.100403.
- [HM00] C. J. Halboth and W. Metzner. “Renormalization-group analysis of the two-dimensional Hubbard model”. *Phys. Rev. B* 61 (2000), 7364–7377. DOI: 10.1103/PhysRevB.61.7364.
- [HNE12] E. A. Henriksen, D. Nandi, and J. P. Eisenstein. “Quantum Hall Effect and Semimetallic Behavior of Dual-Gated ABA-Stacked Tri-layer Graphene”. *Phys. Rev. X* 2 (2012), 011004. DOI: 10.1103/PhysRevX.2.011004.
- [Hon01] C. Honerkamp, M. Salmhofer, N. Furukawa, and T. M. Rice. “Breakdown of the Landau-Fermi liquid in two dimensions due to umklapp scattering”. *Phys. Rev. B* 63 (2001), 035109. DOI: 10.1103/PhysRevB.63.035109.
- [Hon04] C. Honerkamp, D. Rohe, S. Andergassen, and T. Enss. “Interaction flow method for many-fermion systems”. *Phys. Rev. B* 70 (2004), 235115. DOI: 10.1103/PhysRevB.70.235115.
- [Hon08] C. Honerkamp. “Density Waves and Cooper Pairing on the Honeycomb Lattice”. *Phys. Rev. Lett.* 100 (2008), 146404. DOI: 10.1103/PhysRevLett.100.146404.
- [Hon10] C. Honerkamp. “Iron pnictide superconductors studied by the functional renormalization group”. *The European Physical Journal - Special Topics* 188 (2010), 33–47. DOI: 10.1140/epjst/e2010-01295-x.
- [Hon12] C. Honerkamp. “Effective interactions in multiband systems from constrained summations”. *Phys. Rev. B* 85 (2012), 195129. DOI: 10.1103/PhysRevB.85.195129.
- [Hot06] T. Hotta. “Orbital ordering phenomena in d- and f-electron systems”. *Reports on Progress in Physics* 69 (2006), 2061. DOI: 10.1088/0034-4885/69/7/R02.

- [HR95] R. Hlubina and T. M. Rice. “Resistivity as a function of temperature for models with hot spots on the Fermi surface”. *Phys. Rev. B* 51 (1995), 9253–9260. DOI: 10.1103/PhysRevB.51.9253.
- [HS01] C. Honerkamp and M. Salmhofer. “Temperature-flow renormalization group and the competition between superconductivity and ferromagnetism”. *Phys. Rev. B* 64 (2001), 184516. DOI: 10.1103/PhysRevB.64.184516.
- [HS03] C. Honerkamp and M. Salmhofer. “Flow of the quasiparticle weight in the N -patch renormalization group scheme”. *Phys. Rev. B* 67 (2003), 174504. DOI: 10.1103/PhysRevB.67.174504.
- [HS09] C. Husemann and M. Salmhofer. “Efficient parametrization of the vertex function, Ω scheme, and the t, t' Hubbard model at van Hove filling”. *Phys. Rev. B* 79 (2009), 195125. DOI: 10.1103/PhysRevB.79.195125.
- [Hub63] J. Hubbard. “Electron Correlations in Narrow Energy Bands”. *Proceedings of the Royal Society of London A. Mathematical and Physical Sciences* 276 (1963), 238–257. DOI: 10.1098/rspa.1963.0204.
- [Hus09] C. Husemann. “Competing Orders in the Hubbard Model”. PhD thesis. Universität Leipzig, 2009.
- [IAK10] H. Ikeda, R. Arita, and J. Kuneš. “Phase diagram and gap anisotropy in iron-pnictide superconductors”. *Phys. Rev. B* 81 (2010), 054502. DOI: 10.1103/PhysRevB.81.054502.
- [Jha11] S. H. Jhang, M. F. Craciun, S. Schmidmeier, S. Tokumitsu, S. Russo, M. Yamamoto, Y. Skourski, J. Wosnitza, S. Tarucha, J. Eroms, and C. Strunk. “Stacking-order dependent transport properties of trilayer graphene”. *Phys. Rev. B* 84 (2011), 161408. DOI: 10.1103/PhysRevB.84.161408.
- [JM12] J. Jung and A. H. MacDonald. “Gapped broken symmetry states in ABC trilayer graphene” (2012). <http://arxiv.org/abs/1208.0116>.
- [JZM11] J. Jung, F. Zhang, and A. H. MacDonald. “Lattice theory of pseudospin ferromagnetism in bilayer graphene: Competing interaction-induced quantum Hall states”. *Phys. Rev. B* 83 (2011), 115408. DOI: 10.1103/PhysRevB.83.115408.
- [Kam08] Y. Kamihara, T. Watanabe, M. Hirano, and H. Hosono. “Iron-Based Layered Superconductor $\text{La}[\text{O}_{1-x}\text{F}_x]\text{FeAs}$ ($x = 0.05 - 0.12$) with $T_c = 26\text{K}$ ”. *Journal of the American Chemical Society* 130 (2008), 3296–3297. DOI: 10.1021/ja800073m.

-
- [Kat04] A. A. Katanin. “Fulfillment of Ward identities in the functional renormalization group approach”. *Phys. Rev. B* 70 (2004), 115109. DOI: 10.1103/PhysRevB.70.115109.
- [Kat09] A. A. Katanin. “Two-loop functional renormalization group approach to the one- and two-dimensional Hubbard model”. *Phys. Rev. B* 79 (2009), 235119. DOI: 10.1103/PhysRevB.79.235119.
- [KBS10] P. Kopietz, L. Bartosch, and F. Schütz. *Introduction to the Functional Renormalization Group*. Vol. 798. Lecture Notes in Physics. Springer, 2010. ISBN: 9783642050930.
- [KDP80] K. v. Klitzing, G. Dorda, and M. Pepper. “New Method for High-Accuracy Determination of the Fine-Structure Constant Based on Quantized Hall Resistance”. *Phys. Rev. Lett.* 45 (1980), 494–497. DOI: 10.1103/PhysRevLett.45.494.
- [Ken08] P. R. C. Kent, T. Saha-Dasgupta, O. Jepsen, O. K. Andersen, A. Macridin, T. A. Maier, M. Jarrell, and T. C. Schulthess. “Combined density functional and dynamical cluster quantum Monte Carlo calculations of the three-band Hubbard model for hole-doped cuprate superconductors”. *Phys. Rev. B* 78 (2008), 035132. DOI: 10.1103/PhysRevB.78.035132.
- [Kha12] M. Kharitonov. “Correlated antiferromagnetic state in bilayer graphene” (2012). <http://de.arxiv.org/abs/1109.1553>.
- [Kho12] T. Khodkov, F. Withers, D. C. Hudson, M. F. Craciun, and S. Russo. “Electrical transport in suspended and double gated trilayer graphene”. *Appl. Phys. Lett.* 100 (2012), 013114. DOI: 10.1063/1.3675337.
- [Kie12] M. L. Kiesel, C. Platt, W. Hanke, D. A. Abanin, and R. Thomale. “Competing many-body instabilities and unconventional superconductivity in graphene”. *Phys. Rev. B* 86 (2012), 020507. DOI: 10.1103/PhysRevB.86.020507.
- [KK04] A. A. Katanin and A. P. Kampf. “Quasiparticle Anisotropy and Pseudogap Formation from the Weak-Coupling Renormalization Group Point of View”. *Phys. Rev. Lett.* 93 (2004), 106406. DOI: 10.1103/PhysRevLett.93.106406.
- [KM05a] C. L. Kane and E. J. Mele. “Quantum Spin Hall Effect in Graphene”. *Phys. Rev. Lett.* 95 (2005), 226801. DOI: 10.1103/PhysRevLett.95.226801.
- [KM05b] C. L. Kane and E. J. Mele. “ Z_2 Topological Order and the Quantum Spin Hall Effect”. *Phys. Rev. Lett.* 95 (2005), 146802. DOI: 10.1103/PhysRevLett.95.146802.

- [KM09] M. Koshino and E. McCann. “Trigonal warping and Berry’s phase $N\pi$ in ABC-stacked multilayer graphene”. *Phys. Rev. B* 80 (2009), 165409. DOI: 10.1103/PhysRevB.80.165409.
- [KM11] M. Koshino and E. McCann. “Landau level spectra and the quantum Hall effect of multilayer graphene”. *Phys. Rev. B* 83 (2011), 165443. DOI: 10.1103/PhysRevB.83.165443.
- [Kon07] M. König, S. Wiedmann, C. Brüne, A. Roth, H. Buhmann, L. W. Molenkamp, X.-L. Qi, and S.-C. Zhang. “Quantum Spin Hall Insulator State in HgTe Quantum Wells”. *Science* 318 (2007), 766–770. DOI: 10.1126/science.1148047.
- [Kot12] V. N. Kotov, B. Uchoa, V. M. Pereira, F. Guinea, and A. H. Castro Neto. “Electron-Electron Interactions in Graphene: Current Status and Perspectives”. *Rev. Mod. Phys.* 84 (2012), 1067–1125. DOI: 10.1103/RevModPhys.84.1067.
- [KT06] F. D. Klironomos and S.-W. Tsai. “Phonon-mediated tuning of instabilities in the Hubbard model at half-filling”. *Phys. Rev. B* 74 (2006), 205109. DOI: 10.1103/PhysRevB.74.205109.
- [Kum11] A. Kumar, W. Escoffier, J. M. Poumirol, C. Faugeras, D. P. Arovas, M. M. Fogler, F. Guinea, S. Roche, M. Goiran, and B. Raquet. “Integer Quantum Hall Effect in Trilayer Graphene”. *Phys. Rev. Lett.* 107 (2011), 126806. DOI: 10.1103/PhysRevLett.107.126806.
- [Kun10] J. Kuneš, R. Arita, P. Wissgott, A. Toschi, H. Ikeda, and K. Held. “Wien2wannier: From linearized augmented plane waves to maximally localized Wannier functions”. *Computer Physics Communications* 181 (2010), 1888–1895. DOI: 10.1016/j.cpc.2010.08.005.
- [Kur09] K. Kuroki, H. Usui, S. Onari, R. Arita, and H. Aoki. “Pnictogen height as a possible switch between high- T_c nodeless and low- T_c nodal pairings in the iron-based superconductors”. *Phys. Rev. B* 79 (2009), 224511. DOI: 10.1103/PhysRevB.79.224511.
- [Kuz09] A. B. Kuzmenko, I. Crassee, D. van der Marel, P. Blake, and K. S. Novoselov. “Determination of the gate-tunable band gap and tight-binding parameters in bilayer graphene using infrared spectroscopy”. *Phys. Rev. B* 80 (2009), 165406. DOI: 10.1103/PhysRevB.80.165406.
- [LAF12] Y. Lemonik, I. Aleiner, and V. I. Fal’ko. “Competing nematic, antiferromagnetic, and spin-flux orders in the ground state of bilayer graphene”. *Phys. Rev. B* 85 (2012), 245451. DOI: 10.1103/PhysRevB.85.245451.

-
- [Lan12] T. C. Lang, Z. Y. Meng, M. M. Scherer, S. Uebelacker, F. F. Assaad, A. Muramatsu, C. Honerkamp, and S. Wessel. “Antiferromagnetism in the Hubbard Model on the Bernal-Stacked Honeycomb Bilayer”. *Phys. Rev. Lett.* 109 (2012), 126402. DOI: 10.1103/PhysRevLett.109.126402.
- [Lem10] Y. Lemonik, I. L. Aleiner, C. Toke, and V. I. Fal’ko. “Spontaneous symmetry breaking and Lifshitz transition in bilayer graphene”. *Phys. Rev. B* 82 (2010), 201408. DOI: 10.1103/PhysRevB.82.201408.
- [Lic12] J. Lichtenstein. “*Untersuchungen zu 1111-Eisen-Arseniden mittels funktionaler Renormierungsgruppe*”. Master thesis. RWTH Aachen University. 2012.
- [LR87] P. A. Lee and N. Read. “Why is T_c of the oxide superconductors so low?” *Phys. Rev. Lett.* 58 (1987), 2691–2694. DOI: 10.1103/PhysRevLett.58.2691.
- [Lui11] C. H. Lui, Z. Li, K. F. Mak, E. Cappelluti, and T. F. Heinz. “Observation of an electrically tunable band gap in trilayer graphene”. *Nat. Phys.* 7 (2011), 944–947. DOI: 10.1038/nphys2102.
- [MAF07] E. McCann, D. S. L. Abergel, and V. I. Fal’ko. “Electrons in bilayer graphene”. *Solid State Communications* 143 (2007), 110–115. DOI: 10.1016/j.ssc.2007.03.054.
- [Mai00] T. Maier, M. Jarrell, T. Pruschke, and J. Keller. “ d -Wave Superconductivity in the Hubbard Model”. *Phys. Rev. Lett.* 85 (2000), 1524–1527. DOI: 10.1103/PhysRevLett.85.1524.
- [Mar10] J. Martin, B. E. Feldman, R. T. Weitz, M. T. Allen, and A. Yacoby. “Local Compressibility Measurements of Correlated States in Suspended Bilayer Graphene”. *Phys. Rev. Lett.* 105 (2010), 256806. DOI: 10.1103/PhysRevLett.105.256806.
- [May11] A. S. Mayorov, D. C. Elias, M. Mucha-Kruczynski, R. V. Gorbachev, T. Tudorovskiy, A. Zhukov, S. V. Morozov, M. I. Katsnelson, V. I. Fal’ko, A. K. Geim, and K. S. Novoselov. “Interaction-Driven Spectrum Reconstruction in Bilayer Graphene”. *Science* 333 (2011), 860–863. DOI: 10.1126/science.1208683.
- [Men10] Z. Y. Meng, T. C. Lang, S. Wessel, F. F. Assaad, and A. Muramatsu. “Quantum spin liquid emerging in two-dimensional correlated Dirac fermions”. *Nature* 464 (2010), 847–851. DOI: 10.1038/nature08942.
- [Met12] W. Metzner, M. Salmhofer, C. Honerkamp, V. Meden, and K. Schönhammer. “Functional renormalization group approach to correlated fermion systems”. *Rev. Mod. Phys.* 84 (2012), 299–352. DOI: 10.1103/RevModPhys.84.299.

- [MH12] S. A. Maier and C. Honerkamp. “Effective three-particle interactions in low-energy models for multiband systems”. *Phys. Rev. B* 85 (2012), 064520. DOI: 10.1103/PhysRevB.85.064520.
- [Min08] H. Min, G. Borghi, M. Polini, and A. H. MacDonald. “Pseudospin magnetism in graphene”. *Phys. Rev. B* 77 (2008), 041407. DOI: 10.1103/PhysRevB.77.041407.
- [MJ01] S. Moukouri and M. Jarrell. “Absence of a Slater Transition in the Two-Dimensional Hubbard Model”. *Phys. Rev. Lett.* 87 (2001), 167010. DOI: 10.1103/PhysRevLett.87.167010.
- [MJZ12] A. H. MacDonald, J. Jung, and F. Zhang. “Pseudospin order in monolayer, bilayer and double-layer graphene”. *Physica Scripta* 2012 (2012), 014012. DOI: 10.1088/0031-8949/2012/T146/014012.
- [MK12] E. McCann and M. Koshino. “The electronic properties of bilayer graphene” (2012). <http://arxiv.org/abs/1205.6953>.
- [Mos08] A. A. Mostofi, J. R. Yates, Y.-S. Lee, I. Souza, D. Vanderbilt, and N. Marzari. “wannier90: A tool for obtaining maximally-localised Wannier functions”. *Computer Physics Communications* 178 (2008), 685–699. DOI: 10.1016/j.cpc.2007.11.016.
- [MW66] N. D. Mermin and H. Wagner. “Absence of Ferromagnetism or Antiferromagnetism in One- or Two-Dimensional Isotropic Heisenberg Models”. *Phys. Rev. Lett.* 17 (1966), 1133–1136. DOI: 10.1103/PhysRevLett.17.1133.
- [NK10] W. Norimatsu and M. Kusunoki. “Selective formation of ABC-stacked graphene layers on SiC(0001)”. *Phys. Rev. B* 81 (2010), 161410. DOI: 10.1103/PhysRevB.81.161410.
- [NL10a] R. Nandkishore and L. Levitov. “Dynamical Screening and Excitonic Instability in Bilayer Graphene”. *Phys. Rev. Lett.* 104 (2010), 156803. DOI: 10.1103/PhysRevLett.104.156803.
- [NL10b] R. Nandkishore and L. Levitov. “Quantum anomalous Hall state in bilayer graphene”. *Phys. Rev. B* 82 (2010), 115124. DOI: 10.1103/PhysRevB.82.115124.
- [NO98] J. W. Negele and H. Orland. *Quantum Many-Particle Systems*. Advanced Book Classics. Perseus Books, 1998. ISBN: 9780738200521.
- [Nov04] K. S. Novoselov, A. K. Geim, S. V. Morozov, D. Jiang, Y. Zhang, S. V. Dubonos, I. V. Grigorieva, and A. A. Firsov. “Electric Field Effect in Atomically Thin Carbon Films”. *Science* 306 (2004), 666–669. DOI: 10.1126/science.1102896.

-
- [Oht07] T. Ohta, A. Bostwick, J. L. McChesney, T. Seyller, K. Horn, and E. Rotenberg. “Interlayer Interaction and Electronic Screening in Multilayer Graphene Investigated with Angle-Resolved Photoemission Spectroscopy”. *Phys. Rev. Lett.* 98 (2007), 206802. DOI: 10.1103/PhysRevLett.98.206802.
- [Pav01] E. Pavarini, I. Dasgupta, T. Saha-Dasgupta, O. Jepsen, and O. K. Andersen. “Band-Structure Trend in Hole-Doped Cuprates and Correlation with $T_{c\max}$ ”. *Phys. Rev. Lett.* 87 (2001), 047003. DOI: 10.1103/PhysRevLett.87.047003.
- [Paw07] J. M. Pawłowski. “Aspects of the functional renormalisation group”. *Annals of Physics* 322 (2007), 2831–2915. DOI: 10.1016/j.aop.2007.01.007.
- [PG10] J. Paglione and R. L. Greene. “High-temperature superconductivity in iron-based materials”. *Nat. Phys.* 6 (2010), 645–658. DOI: 10.1038/nphys1759.
- [PHH09] C. Platt, C. Honerkamp, and W. Hanke. “Pairing in the iron arsenides: a functional RG treatment”. *New Journal of Physics* 11 (2009), 055058. DOI: 10.1088/1367-2630/11/5/055058.
- [Pla12] C. Platt, R. Thomale, C. Honerkamp, S.-C. Zhang, and W. Hanke. “Mechanism for a pairing state with time-reversal symmetry breaking in iron-based superconductors”. *Phys. Rev. B* 85 (2012), 180502. DOI: 10.1103/PhysRevB.85.180502.
- [Pol84] J. Polchinski. “Renormalization and effective lagrangians”. *Nuclear Physics B* 231 (1984), 269–295. DOI: 10.1016/0550-3213(84)90287-6.
- [PSS10] M. Pletyukhov, D. Schuricht, and H. Schoeller. “Relaxation versus Decoherence: Spin and Current Dynamics in the Anisotropic Kondo Model at Finite Bias and Magnetic Field”. *Phys. Rev. Lett.* 104 (2010), 106801. DOI: 10.1103/PhysRevLett.104.106801.
- [QWZ06] X.-L. Qi, Y.-S. Wu, and S.-C. Zhang. “Topological quantization of the spin Hall effect in two-dimensional paramagnetic semiconductors”. *Phys. Rev. B* 74 (2006), 085308. DOI: 10.1103/PhysRevB.74.085308.
- [QZ11] X.-L. Qi and S.-C. Zhang. “Topological insulators and superconductors”. *Rev. Mod. Phys.* 83 (2011), 1057–1110. DOI: 10.1103/RevModPhys.83.1057.
- [Rag08] S. Raghu, X.-L. Qi, C. Honerkamp, and S.-C. Zhang. “Topological Mott Insulators”. *Phys. Rev. Lett.* 100 (2008), 156401. DOI: 10.1103/PhysRevLett.100.156401.

- [RLH10] S. Rachel and K. Le Hur. “Topological insulators and Mott physics from the Hubbard interaction”. *Phys. Rev. B* 82 (2010), 075106. DOI: 10.1103/PhysRevB.82.075106.
- [RM05] D. Rohe and W. Metzner. “Pseudogap at hot spots in the two-dimensional Hubbard model at weak coupling”. *Phys. Rev. B* 71 (2005), 115116. DOI: 10.1103/PhysRevB.71.115116.
- [RTT11] J. Reuther, R. Thomale, and S. Trebst. “Finite-temperature phase diagram of the Heisenberg-Kitaev model”. *Phys. Rev. B* 84 (2011), 100406. DOI: 10.1103/PhysRevB.84.100406.
- [Sak10] H. Sakakibara, H. Usui, K. Kuroki, R. Arita, and H. Aoki. “Two-Orbital Model Explains the Higher Transition Temperature of the Single-Layer Hg-Cuprate Superconductor Compared to That of the La-Cuprate Superconductor”. *Phys. Rev. Lett.* 105 (2010), 057003. DOI: 10.1103/PhysRevLett.105.057003.
- [Sal04] M. Salmhofer, C. Honerkamp, W. Metzner, and O. Lauscher. “Renormalization Group Flows into Phases with Broken Symmetry”. *Progress of Theoretical Physics* 112 (2004), 943–970. DOI: 10.1143/PTP.112.943.
- [Sal99] M. Salmhofer. *Renormalization: An Introduction*. Springer, 1999. ISBN: 9783540646662.
- [SB07] J. R. Schrieffer and J. S. Brooks. *Handbook of High-Temperature Superconductivity*. Springer, 2007. ISBN: 9780387350714.
- [Sch09] H. Schoeller. “A perturbative nonequilibrium renormalization group method for dissipative quantum mechanics”. *The European Physical Journal - Special Topics* 168 (2009), 179–266. DOI: 10.1140/epjst/e2009-00962-3.
- [Sch12] M. M. Scherer, S. Uebelacker, D. D. Scherer, and C. Honerkamp. “Interacting electrons on trilayer honeycomb lattices”. *Phys. Rev. B* 86 (2012), 155415. DOI: 10.1103/PhysRevB.86.155415.
- [Sch87] H. J. Schulz. “Superconductivity and Antiferromagnetism in the Two-Dimensional Hubbard Model: Scaling Theory”. *Europhys. Lett.* 4 (1987), 609. DOI: 10.1209/0295-5075/4/5/016.
- [SCP98] H. J. Schulz, G. Cuniberti, and P. Pieri. “Fermi liquids and Luttinger liquids” (1998). <http://de.arxiv.org/abs/cond-mat/9807366>.
- [SGM08] P. Strack, R. Gersch, and W. Metzner. “Renormalization group flow for fermionic superfluids at zero temperature”. *Phys. Rev. B* 78 (2008), 014522. DOI: 10.1103/PhysRevB.78.014522.
- [SH01] M. Salmhofer and C. Honerkamp. “Fermionic Renormalization Group Flows”. *Progress of Theoretical Physics* 105 (2001), 1–35. DOI: 10.1143/PTP.105.1.

-
- [Sha94] R. Shankar. “Renormalization-group approach to interacting fermions”. *Rev. Mod. Phys.* 66 (1994), 129–192. DOI: 10.1103/RevModPhys.66.129.
- [Shi04] C. T. Shih, T. K. Lee, R. Eder, C.-Y. Mou, and Y. C. Chen. “Enhancement of Pairing Correlation by t' in the Two-Dimensional Extended t - J Model”. *Phys. Rev. Lett.* 92 (2004), 227002. DOI: 10.1103/PhysRevLett.92.227002.
- [Spa08] L. Spanu, M. Lugas, F. Becca, and S. Sorella. “Magnetism and superconductivity in the t - t' - J model”. *Phys. Rev. B* 77 (2008), 024510. DOI: 10.1103/PhysRevB.77.024510.
- [SUH12] M. M. Scherer, S. Uebelacker, and C. Honerkamp. “Instabilities of interacting electrons on the honeycomb bilayer”. *Phys. Rev. B* 85 (2012), 235408. DOI: 10.1103/PhysRevB.85.235408.
- [Sun09] K. Sun, H. Yao, E. Fradkin, and S. A. Kivelson. “Topological Insulators and Nematic Phases from Spontaneous Symmetry Breaking in 2D Fermi Systems with a Quadratic Band Crossing”. *Phys. Rev. Lett.* 103 (2009), 046811. DOI: 10.1103/PhysRevLett.103.046811.
- [SZ10] A. Sinner and K. Ziegler. “Effect of the Coulomb interaction on the gap in monolayer and bilayer graphene”. *Phys. Rev. B* 82 (2010), 165453. DOI: 10.1103/PhysRevB.82.165453.
- [Tam07] K.-M. Tam, S.-W. Tsai, D. K. Campbell, and A. H. Castro Neto. “Retardation effects in the Holstein-Hubbard chain at half filling”. *Phys. Rev. B* 75 (2007), 161103. DOI: 10.1103/PhysRevB.75.161103.
- [Tay11] T. Taychatanapat, K. Watanabe, T. Taniguchi, and P. Jarillo-Herrero. “Quantum Hall effect and Landau-level crossing of Dirac fermions in trilayer graphene”. *Nat. Phys.* 7 (2011), 621–625. DOI: 10.1038/nphys2008.
- [Tho11a] R. Thomale, C. Platt, W. Hanke, and B. A. Bernevig. “Mechanism for Explaining Differences in the Order Parameters of FeAs-Based and FeP-Based Pnictide Superconductors”. *Phys. Rev. Lett.* 106 (2011), 187003. DOI: 10.1103/PhysRevLett.106.187003.
- [Tho11b] R. Thomale, C. Platt, W. Hanke, J. Hu, and B. A. Bernevig. “Exotic d -Wave Superconducting State of Strongly Hole-Doped $\mathbf{K}_x\text{Ba}_{1-x}\text{Fe}_2\text{As}_2$ ”. *Phys. Rev. Lett.* 107 (2011), 117001. DOI: 10.1103/PhysRevLett.107.117001.
- [TV11] R. E. Throckmorton and O. Vafek. “Fermions on bilayer graphene: symmetry breaking for $B=0$ and $\nu=0$ ” (2011). <http://de.arxiv.org/abs/1111.2076>.

- [UCN07] B. Uchoa and A. H. Castro Neto. “Superconducting States of Pure and Doped Graphene”. *Phys. Rev. Lett.* 98 (2007), 146801. DOI: 10.1103/PhysRevLett.98.146801.
- [Ueb09] S. Uebelacker. “Renormierungsgruppenfluss der Selbstenergie im zweidimensionalen Hubbard-Modell”. Diploma thesis. Universität Würzburg. 2009.
- [UH11] S. Uebelacker and C. Honerkamp. “Instabilities of quadratic band crossing points”. *Phys. Rev. B* 84 (2011), 205122. DOI: 10.1103/PhysRevB.84.205122.
- [UH12a] S. Uebelacker and C. Honerkamp. “Multiband effects on superconducting instabilities driven by electron-electron interactions”. *Phys. Rev. B* 85 (2012), 155122. DOI: 10.1103/PhysRevB.85.155122.
- [UH12b] S. Uebelacker and C. Honerkamp. “Self-energy feedback and frequency-dependent interactions in the functional renormalization group flow for the two-dimensional Hubbard model”. *Phys. Rev. B* 86 (2012), 235140. DOI: 10.1103/PhysRevB.86.235140.
- [Vaf10] O. Vafek. “Interacting fermions on the honeycomb bilayer: From weak to strong coupling”. *Phys. Rev. B* 82 (2010), 205106. DOI: 10.1103/PhysRevB.82.205106.
- [Var09] C. N. Varney, C.-R. Lee, Z. J. Bai, S. Chiesa, M. Jarrell, and R. T. Scalettar. “Quantum Monte Carlo study of the two-dimensional fermion Hubbard model”. *Phys. Rev. B* 80 (2009), 075116. DOI: 10.1103/PhysRevB.80.075116.
- [Var11] C. N. Varney, K. Sun, M. Rigol, and V. Galitski. “Topological phase transitions for interacting finite systems”. *Phys. Rev. B* 84 (2011), 241105. DOI: 10.1103/PhysRevB.84.241105.
- [Var89] C. M. Varma, P. B. Littlewood, S. Schmitt-Rink, E. Abrahams, and A. E. Ruckenstein. “Phenomenology of the normal state of Cu-O high-temperature superconductors”. *Phys. Rev. Lett.* 63 (1989), 1996–1999. DOI: 10.1103/PhysRevLett.63.1996.
- [Vel12a] J. Velasco, L. Jing, W. Bao, Y. Lee, P. Kratz, V. Aji, M. Bockrath, C. N. Lau, C. Varma, R. Stillwell, D. Smirnov, F. Zhang, J. Jung, and A. H. MacDonald. “Transport spectroscopy of symmetry-broken insulating states in bilayer graphene”. *Nature Nanotechnology* 7 (2012), 156–160. DOI: 10.1038/nnano.2011.251.
- [Vel12b] A. Veligura, H. J. van Elferen, N. Tombros, J. C. Maan, U. Zeitler, and B. J. van Wees. “Transport gap in suspended bilayer graphene at zero magnetic field”. *Phys. Rev. B* 85 (2012), 155412. DOI: 10.1103/PhysRevB.85.155412.

-
- [VY10] O. Vafek and K. Yang. “Many-body instability of Coulomb interacting bilayer graphene: Renormalization group approach”. *Phys. Rev. B* 81 (2010), 041401. DOI: 10.1103/PhysRevB.81.041401.
- [Wan09] F. Wang, H. Zhai, Y. Ran, A. Vishwanath, and D.-H. Lee. “Functional Renormalization-Group Study of the Pairing Symmetry and Pairing Mechanism of the FeAs-Based High-Temperature Superconductor”. *Phys. Rev. Lett.* 102 (2009), 047005. DOI: 10.1103/PhysRevLett.102.047005.
- [Wan12] W.-S. Wang, Y.-Y. Xiang, Q.-H. Wang, F. Wang, F. Yang, and D.-H. Lee. “Functional renormalization group and variational Monte Carlo studies of the electronic instabilities in graphene near 1/4 doping”. *Phys. Rev. B* 85 (2012), 035414. DOI: 10.1103/PhysRevB.85.035414.
- [Weh11] T. O. Wehling, E. Şaşıoğlu, C. Friedrich, A. I. Lichtenstein, M. I. Katsnelson, and S. Blügel. “Strength of Effective Coulomb Interactions in Graphene and Graphite”. *Phys. Rev. Lett.* 106 (2011), 236805. DOI: 10.1103/PhysRevLett.106.236805.
- [Wei10] R. T. Weitz, M. T. Allen, B. E. Feldman, J. Martin, and A. Jacoby. “Broken-Symmetry States in Doubly Gated Suspended Bilayer Graphene”. *Science* 330 (2010), 812–816. DOI: 10.1126/science.1194988.
- [Wen10] J. Wen, A. Rüegg, C.-C. J. Wang, and G. A. Fiete. “Interaction-driven topological insulators on the kagome and the decorated honeycomb lattices”. *Phys. Rev. B* 82 (2010), 075125. DOI: 10.1103/PhysRevB.82.075125.
- [Wet93] C. Wetterich. “Exact evolution equation for the effective potential”. *Physics Letters B* 301 (1993), 90–94. DOI: 10.1016/0370-2693(93)90726-X.
- [Wil71] K. G. Wilson. “Renormalization Group and Critical Phenomena. II. Phase-Space Cell Analysis of Critical Behavior”. *Phys. Rev. B* 4 (1971), 3184–3205. DOI: 10.1103/PhysRevB.4.3184.
- [WS99] S. R. White and D. J. Scalapino. “Competition between stripes and pairing in a t - t' - J model”. *Phys. Rev. B* 60 (1999), R753–R756. DOI: 10.1103/PhysRevB.60.R753.
- [WZL09] F. Wang, H. Zhai, and D.-H. Lee. “Antiferromagnetic correlation and the pairing mechanism of the cuprates and iron pnictides: A view from the functional renormalization group studies”. *Europhys. Lett.* 85 (2009), 37005. DOI: 10.1209/0295-5075/85/37005.

- [WZL10] F. Wang, H. Zhai, and D.-H. Lee. “Nodes in the gap function of LaFePO, the gap function of the Fe(Se,Te) systems, and the STM signature of the s_{\pm} pairing”. *Phys. Rev. B* 81 (2010), 184512. DOI: 10.1103/PhysRevB.81.184512.
- [Xu12] D.-H. Xu, J. Yuan, Z.-J. Yao, Y. Zhou, J.-H. Gao, and F.-C. Zhang. “Stacking order, interaction and weak surface magnetism in layered graphene sheets” (2012). <http://arxiv.org/abs/1207.5287>.
- [Yao07] Y. Yao, F. Ye, X.-L. Qi, S.-C. Zhang, and Z. Fang. “Spin-orbit gap of graphene: First-principles calculations”. *Phys. Rev. B* 75 (2007), 041401. DOI: 10.1103/PhysRevB.75.041401.
- [YRK11] S. Yuan, R. Roldán, and M. I. Katsnelson. “Landau level spectrum of *ABA*- and *ABC*-stacked trilayer graphene”. *Phys. Rev. B* 84 (2011), 125455. DOI: 10.1103/PhysRevB.84.125455.
- [Zan01] D. Zanchi. “Angle-resolved loss of Landau quasiparticles in 2D Hubbard model”. *Europhys. Lett.* 55 (2001), 376. DOI: 10.1209/epl/i2001-00413-7.
- [ZAV12] L. Zhu, V. Aji, and C. M. Varma. “Ordered Loop Current States in Bilayer Graphene” (2012). <http://arxiv.org/abs/1202.0821v2>.
- [Zee10] A. Zee. *Quantum Field Theory in a Nutshell*. In a Nutshell. Princeton University Press, 2010. ISBN: 9780691140346.
- [Zha08] L. M. Zhang, Z. Q. Li, D. N. Basov, M. M. Fogler, Z. Hao, and M. C. Martin. “Determination of the electronic structure of bilayer graphene from infrared spectroscopy”. *Phys. Rev. B* 78 (2008), 235408. DOI: 10.1103/PhysRevB.78.235408.
- [Zha10a] F. Zhang, H. Min, M. Polini, and A. H. MacDonald. “Spontaneous inversion symmetry breaking in graphene bilayers”. *Phys. Rev. B* 81 (2010), 041402. DOI: 10.1103/PhysRevB.81.041402.
- [Zha10b] F. Zhang, B. Sahu, H. Min, and A. H. MacDonald. “Band structure of *ABC*-stacked graphene trilayers”. *Phys. Rev. B* 82 (2010), 035409. DOI: 10.1103/PhysRevB.82.035409.
- [Zha10c] Z. Zhang, I. Opahle, H. O. Jeschke, and R. Valentí. “Itinerant nature of magnetism in iron pnictides: A first-principles study”. *Phys. Rev. B* 81 (2010), 094505. DOI: 10.1103/PhysRevB.81.094505.
- [Zha11a] F. Zhang, J. Jung, G. A. Fiete, Q. Niu, and A. H. MacDonald. “Spontaneous Quantum Hall States in Chirally Stacked Few-Layer Graphene Systems”. *Phys. Rev. Lett.* 106 (2011), 156801. DOI: 10.1103/PhysRevLett.106.156801.

- [Zha11b] L. Zhang, Y. Zhang, J. Camacho, M. Khodas, and I. Zaliznyak. “The experimental observation of quantum Hall effect of $l=3$ chiral quasiparticles in trilayer graphene”. *Nat. Phys.* 7 (2011), 953–957. DOI: 10.1038/nphys2104.
- [ZMM12] F. Zhang, H. Min, and A. H. MacDonald. “Competing Ordered States in Bilayer Graphene” (2012). <http://arxiv.org/abs/1205.5532>.
- [ZRV09] Y. Zhang, Y. Ran, and A. Vishwanath. “Topological insulators in three dimensions from spontaneous symmetry breaking”. *Phys. Rev. B* 79 (2009), 245331. DOI: 10.1103/PhysRevB.79.245331.
- [ZS00] D. Zanchi and H. J. Schulz. “Weakly correlated electrons on a square lattice: Renormalization-group theory”. *Phys. Rev. B* 61 (2000), 13609–13632. DOI: 10.1103/PhysRevB.61.13609.
- [ZS98] D. Zanchi and H. J. Schulz. “Weakly correlated electrons on a square lattice: A renormalization group theory”. *Europhys. Lett.* 44 (1998), 235. DOI: 10.1209/epl/i1998-00462-x.
- [ZTM12] F. Zhang, D. Tilahun, and A. H. MacDonald. “Hund’s rules for the $N = 0$ Landau levels of trilayer graphene”. *Phys. Rev. B* 85 (2012), 165139. DOI: 10.1103/PhysRevB.85.165139.
- [ZYD97] A. T. Zheleznyak, V. M. Yakovenko, and I. E. Dzyaloshinskii. “Parquet solution for a flat Fermi surface”. *Phys. Rev. B* 55 (1997), 3200–3215. DOI: 10.1103/PhysRevB.55.3200.

Publications

The compilation of this thesis is solely to the author, however, a large part of the work presented here has been published in previous articles and has been done in collaboration with the authors mentioned below, which I cordially appreciate. Parts of previous publications are contained in particular, but not exclusively, in the chapters 3 – 7, in which the results are detailed. In these chapters, the respective publications are indicated in the individual abstracts.

List of publications:

- S. Uebelacker and C. Honerkamp. "Instabilities of quadratic band crossing points". *Phys. Rev. B* 84 (2011), 205122, [UH11].
- S. Uebelacker and C. Honerkamp. "Multiband effects on superconducting instabilities driven by electron-electron interactions". *Phys. Rev. B* 85 (2012), 155122, [UH12a].
- M. M. Scherer, S. Uebelacker, and C. Honerkamp. "Instabilities of interacting electrons on the honeycomb bilayer". *Phys. Rev. B* 85 (2012), 235408, [SUH12].
- T. C. Lang, Z. Y. Meng, M. M. Scherer, S. Uebelacker, F. F. Assaad, A. Muramatsu, C. Honerkamp, and S. Wessel. "Antiferromagnetism in the Hubbard Model on the Bernal-stacked Honeycomb Bilayer". *Phys. Rev. Lett.* 109 (2012), 126402, [Lan12].
- M. M. Scherer, S. Uebelacker, D. D. Scherer, and C. Honerkamp. "Interacting electrons on trilayer honeycomb lattices". *Phys. Rev. B* 86 (2012), 155415, [Sch12].
- S. Uebelacker and C. Honerkamp. "Self-energy feedback and frequency-dependent interactions in the functional renormalization group flow for the two-dimensional Hubbard model". *Phys. Rev. B* 86 (2012), 235140, [UH12b].

Acknowledgements

Zunächst möchte ich Carsten Honerkamp herzlich dafür danken, dass er mir die Gelegenheit gegeben hat in seiner Arbeitsgruppe zu arbeiten und mich über insgesamt fast 5 Jahre ausgezeichnet betreut hat. Seine kreativen Ideen und sein stets kompetenter Rat waren eine große Hilfe und essentiell für diese Arbeit.

Ich danke weiterhin Prof. Dr. Werner Hanke für die Übernahme des Koreferats.

Für die erfolgreiche Zusammenarbeit möchte ich mich bei Thomas Lang, Stefan Wessel und Daniel Scherer bedanken. Besonderen Dank schulde ich Michael Scherer, der mich für die Forschung an Graphen begeistert hat und von dem ich durch die gemeinsame Arbeit vieles gelernt habe.

Über die Jahre meiner Forschungstätigkeit habe ich die stets angenehme Arbeitsatmosphäre genossen und von vielen Diskussionen, sowohl fachlich als auch persönlich, profitiert. Neben den bereits genannten seien Michael Kinza, Jutta Ortloff, Guido Klingschat, Stefan Maier und Julian Lichtenstein stellvertretend erwähnt.

Ebenfalls möchte ich unserer Sekretärin Gabriele Kramp-Salecker danken, die weit über ihre Dienstpflichten hinaus immer hilfsbereit und zuvorkommend war.

Vieles verdanke ich meiner Familie, besonders meinen Eltern, die mich immer unterstützt haben.

Schließlich möchte ich mich bei meiner Frau Susanne bedanken, für ihre Liebe und dafür, dass sie immer ein offenes Ohr für mich hat.

Curriculum Vitae

Stefan Andreas Uebelacker

born on 22 February 1984 in Fulda, Germany

June 2003

Abitur

Rabanus-Maurus-Schule, Fulda

Apr. 2004 - Jan. 2009

Studies of Physics (Diploma)

Bayerische Julius-Maximilians-Universität Würzburg

Feb. 2008 - Jan. 2009

Diploma Thesis

*“Renormierungsgruppenfluss der Selbstenergie im
zweidimensionalen Hubbard-Modell”*

Advisor: Prof. Dr. Carsten Honerkamp

Mar. 2009 - Dec. 2009
since Jan. 2010

Ph.D. Studies

Bayerische Julius-Maximilians-Universität Würzburg

RWTH Aachen University

Advisor: Prof. Dr. Carsten Honerkamp